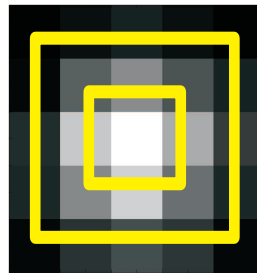


Electron multiplying CCD – based detection in Fluorescence Correlation Spectroscopy and measurements in living zebrafish embryos



Dissertation zur Erlangung des akademischen Grades
Doctor rerum naturalium (Dr. rer. nat.)

vorgelegt von

Markus Burkhardt

geboren in Dresden am 19.09.1978

Mai 2010

First Referee: Prof. Dr. Petra Schwille

Second Referee: Prof. Dr. Thorsten Wohland

Submitted on: 31 May 2010

Oral examination: 7 September 2010

Abstract

Fluorescence correlation spectroscopy (FCS) is an ultra-sensitive optical technique to investigate the dynamic properties of ensembles of single fluorescent molecules in solution. It is in particular suited for measurements in biological samples. High sensitivity is obtained by employing confocal microscopy setups with diffraction limited small detection volumes, and by using single-photon sensitive detectors, for example avalanche photo diodes (APD). However, fluorescence signal is hence typically collected from a single focus position in the sample only, and several measurements at different positions have to be performed successively.

To overcome the time-consuming successive FCS measurements, we introduce electron multiplying CCD (EMCCD) camera-based spatially resolved detection for FCS. With this new detection method, multiplexed FCS measurements become feasible. Towards this goal, we perform FCS measurements with two focal volumes. As an application, we demonstrate spatial cross-correlation measurements between the two detection volumes, which allow to measure calibration-free diffusion coefficients and direction-sensitive processes like molecular flow in microfluidic channels.

FCS is furthermore applied to living zebrafish embryos, to investigate the concentration gradient of the morphogen fibroblast growth factor 8 (Fgf8). It is shown by one-focus APD-based and two-focus EMCCD-based FCS, that Fgf8 propagates largely by random diffusion through the extracellular space in developing tissue. The stable concentration gradient is shown to arise from the equilibrium between a local morphogen production and the sink function of the receiving cells by receptor-mediated removal from the extracellular space. The study shows the applicability of FCS to whole model organisms. Especially in such dynamically changing systems *in vivo*, the perspective of fast parallel FCS measurements is of great importance.

In this work, we exemplify parallel, spatially resolved FCS by utilizing an EMCCD camera. The approach, however, can be easily adapted to any other class of two-dimensional array detector. Novel generations of array detectors might become available in the near future, so that multiplexed spatial FCS could then emerge as a standard extension to classical one-focus FCS.

Kurzfassung

Elektronenvervielfachungs-CCD-basierte Detektion in der Fluoreszenz-Korrelations-Spektroskopie und Messungen in lebenden Zebrafisch-Embryonen

Fluoreszenz-Korrelations-Spektroskopie (FCS) ist eine hochempfindliche optische Methode, um die dynamischen Eigenschaften eines Ensembles von einzelnen, fluoreszierenden Molekülen in Lösung zu erforschen. Sie ist insbesondere geeignet für Messungen in biologischen Proben. Die hohe Empfindlichkeit wird erreicht durch Verwendung konfokaler Mikroskop-Aufbauten mit beugungsbegrenztem Detektionsvolumen, und durch Messung der Fluoreszenz mit Einzelphotonen-empfindlichen Detektoren, zum Beispiel Avalanche-Photodioden (APD). Dadurch wird das Fluoreszenzsignal allerdings nur von einer einzelnen Fokusposition in der Probe eingesammelt, und mehrfache Messungen an verschiedenen Positionen in der Probe müssen nacheinander durchgeführt werden.

Um die zeitaufwendigen, aufeinanderfolgenden FCS-Einzelmessungen zu überwinden, entwickeln wir in dieser Arbeit Elektronenvervielfachungs-CCD (EMCCD) Kamera-basierte räumlich aufgelöste Detektion für FCS. Mit dieser neuartigen Detektionsmethode werden Multiplex-FCS Messungen möglich. Darauf abzielend führen wir FCS Messungen mit zwei Detektionsvolumina durch. Als Anwendung nutzen wir die räumliche Kreuzkorrelation zwischen dem Signal beider Fokalvolumina. Sie ermöglicht die kalibrationsfreie Bestimmung von Diffusionskoeffizienten und die Messung von gerichteter Bewegung, wie zum Beispiel laminarem Fluss in mikrostrukturierten Kanälen.

FCS wird darüber hinaus angewendet auf Messungen in lebenden Zebrafischembryonen, um den Konzentrationsgradienten des Morphogens Fibroblasten-Wachstumsfaktor 8 (Fgf8) zu untersuchen. Mit Hilfe von APD-basierter ein-Fokus FCS und EMCCD-basierter zwei-Fokus FCS zeigen wir, dass Fgf8 hauptsächlich frei diffundiert im extrazellulären Raum des sich entwickelnden Embryos. Der stabile Konzentrationsgradient entsteht durch ein Gleichgewicht von lokaler Morphogenproduktion und globalem Morphogenabbau durch Rezeptor vermittelte Entfernung aus dem extrazellulären Raum. Die Studie zeigt die Anwendbarkeit von FCS in ganzen Modell-Organismen. Gerade in diesen sich dynamisch ändernden Systemen *in vivo* ist die Perspektive schneller, paralleler FCS-Messungen von großer Bedeutung.

In dieser Arbeit wird räumlich aufgelöste FCS am Beispiel einer EMCCD Kamera durchgeführt. Die Herangehensweise ist jedoch einfach übertragbar auf jede andere Art von zwei-dimensionalem Flächendetektor. Neuartige Flächendetektoren könnten in naher Zukunft verfügbar sein. Dann könnte räumlich aufgelöste Multiplex-FCS eine standardisierte Erweiterung zur klassischen ein-Fokus FCS werden.

List of publications

1. M. Burkhardt, K. G. Heinze, and P. Schwille (2005) Four-color fluorescence correlation spectroscopy realized in a grating-based detection platform. *Opt. Lett.* 30, 2266–2268.
2. M. Burkhardt, and P. Schwille (2006) Electron multiplying CCD based detection for spatially resolved fluorescence correlation spectroscopy. *Opt. Express* 14, 5013–5020.
3. J. Ries*, S. R. Yu*, M. Burkhardt, M. Brand, and P. Schwille (2009) Modular scanning FCS quantifies receptor-ligand interactions in living multicellular organisms. *Nat. Methods* 6, 643–645.
4. S. R. Yu*, M. Burkhardt*, M. Nowak, J. Ries, Z. Petrášek, S. Scholpp, P. Schwille, and M. Brand (2009) Fgf8 morphogen gradient forms by a source-sink mechanism with freely diffusing molecules. *Nature* 461, 533–536.

*These authors contributed equally to the work.

Contents

Abstract/ Kurzfassung	i
List of publications	iii
1. Introduction	1
1.1. Research context	1
1.2. Goal and outline of this thesis	2
I. Theoretical and technological background	3
2. Fluorescence Correlation Spectroscopy (FCS)	5
2.1. Basics of fluorescence	5
2.2. Confocal setup	7
2.3. FCS autocorrelation analysis	9
2.4. FCS cross-correlation analysis	20
3. Detection methods in FCS	28
3.1. Multi-color detection and spectral cross-correlation	28
3.2. Parallel detection and spatial cross-correlation	32
3.3. Prospects of detection with an EMCCD	36
II. Establishment of an EMCCD detection platform for FCS	41
4. Optical setup for FCS with EMCCD detection	43
4.1. Integrated setup with both detectors APD and EMCCD	43
4.2. Technical requirements: adjustment and stability	45
5. EMCCD data acquisition for FCS	48
5.1. Frame transfer mode for ms time resolution	48
5.2. Fast kinetic mode for μ s time resolution	51
5.3. LabVIEW based acquisition software	55
5.4. Matlab based graphical user interface data evaluation software	58
6. Comparison of EMCCD- and APD-based detection in FCS in solution	60
7. Limits of the DV860 EMCCD model and prospects of the DU897 model	62
7.1. Baseline homogeneity across the chip and readout timings	62
7.2. Clock induced charges (CICs)	64

III. Two-focus FCS with EMCCD detection	67
8. Two-focus excitation and detection	69
8.1. Fast alternating two-focus excitation	69
8.2. Two-focus detection and automated distance adjustment	70
9. Refined EMCCD data processing	73
9.1. Enhanced baseline correction	73
9.2. CCD nonlinearity correction	74
9.3. Correction for triangular averaging in correlation analysis	76
10. Precise determination of diffusion coefficients and flow speeds	78
10.1. Diffusion measurements in solution and on membranes	78
10.2. Effect of the confocal pinhole size	81
10.3. Determination of minute flows in micro channels	85
IV. FCS in developmental biology	89
11. Introduction to Zebrafish embryo model system and the morphogen Fgf8	91
12. One-focus FCS in embryos	95
12.1. Major free diffusion of single morphogen molecules	95
12.2. Minor slow diffusion due to interaction with extracellular matrix components	97
13. Two-focus EMCCD-FCS in embryos	99
14. Exploring the morphogen concentration gradient	101
14.1. A stable morphogen gradient <i>in vivo</i>	101
14.2. Mathematical model and deduced key parameters	102
14.3. Direct measurement of the half-life time	105
14.4. Endocytosis controls the morphogen gradient	106
Conclusion and outlook	110
Bibliography	111
Symbols and Abbreviations	122
Acknowledgements	124
Erklärung (Declaration)	127

1. Introduction

1.1. Research context

In the last two decades, Fluorescence Correlation Spectroscopy (FCS) has become an invaluable tool for understanding the biophysics of cellular mechanisms on the molecular scale. When compared to fluorescence microscopy, a much older technique, FCS requires largely the same well-engineered optical instrumentation and efficient biochemical labeling. A special prerequisite for FCS, however, is the need for advanced fluorescence detectors with highest possible quantum efficiency and time resolution, to measure the temporal correlation in the fluorescence signal. From this correlation, thermodynamic and kinetic parameters of the biomolecular processes in solution are extracted.

The detectors of choice are avalanche photo diodes (APD) and photomultiplier tubes (PMT); both of them are currently available as so-called single points detectors. Therefore, in a typical FCS measurement, the fluorescence signal is collected from only one specific focus position in the sample. In practise, an overview confocal image is acquired (~ 1 s measurement time) by scanning the excitation laser across the sample, and FCS is then performed in one position of the image ($\sim 10 - 100$ s measurement time). FCS measurements in different positions have to be performed successively.

One of the major advances in confocal fluorescence imaging in the last years has been the increase of data acquisition beyond video frame rate, which is particularly important for imaging living cells or organisms. This advance has been possible by avoiding the raster-scan of a single laser beam across the sample but by utilizing parallel, multi-foci imaging strategies. Several technical implementations have emerged like spinning disc, multi-spot grid scan or line scan imaging. Besides the necessary multiplexed excitation, the key element enabling this technology is the parallel fluorescence detection with high sensitivity. For this purpose, some PMT-array detectors have been custom-developed. Single-photon counting APD-arrays, being the ultimate goal, are still not available, although they were announced by various companies recently. However, the detector of choice in these fast confocal imaging techniques is the electron multiplying charge-coupled device (EMCCD) camera, the inherent two-dimensional multi-pixel detector, with significantly reduced readout noise compared to standard CCDs.

For FCS, the same great interest in parallel multi-spot detection exists to overcome the sequential, time-consuming data acquisition, especially in living samples, where the measurement time window is often limited by the underlying biological process. In addition, multichannel FCS does not only allow for trivial multiplexing, but also for accessing the spatial cross-correlation. This yields additional information on the directionality of molecular processes. So far, only few multi-spot measurements have been reported which were limited to special purpose-made and inflexible customized excitation and detection setups. To achieve a flexible, parallel FCS functionality, the main task is to find a single-photon-sensitive multi-channel detector suitable for FCS. This thesis contributes to this task by introducing EMCCD-based detection for FCS.

1.2. Goal and outline of this thesis

The goal of the thesis consists of two aspects. First, as detailed above, the prerequisite for multi-spot FCS is to be developed by means of an EMCCD-based camera detector. This is a technological advancement and general task, but its motivation comes from the application of FCS to answer very specific biological questions. The multi-spot detection can elucidate potential directional propagation of molecules in contrast to undirected Brownian diffusion. This distinction is for example important when investigating the dynamics of so-called morphogen molecules in the developing embryo, the molecules that govern patterning of embryonic tissue.

The second aspect of the thesis is dedicated to this application of FCS in whole organisms, in particular in living zebrafish embryos. This task is performed in collaboration with Shuizi Rachel Yu, who was working in the developmental genetics group of Prof. Dr. Michael Brand in Dresden. In this study, important parameters of interest are mobility coefficients, local concentrations and the investigation of the concentration gradient of the morphogen Fibroblast Growth Factor 8 (Fgf8). The suitable instrumentation setup is chosen for each part of the experiment; standard concentration and mobility measurements are carried out with classical APD-based FCS, whereas specific investigation of the nature of morphogen propagation is performed with EMCCD-based FCS.

The thesis is separated into four parts. Part I introduces the theoretical background of FCS and the detection methods in FCS. Current detector standards and novel ideas are discussed.

Part II describes the EMCCD-based detection. Introducing a novel detection method for FCS requires a direct comparison to detection with the avalanche photodiode (APD), which has been the standard detector for the last decades. To investigate solely the influence of the detector, an experimental platform is established (chapter 4), where all the components of a typical (one-focus) FCS setup (excitation laser, objective lens, filter sets) are shared, but the fluorescence emission light can be directed either onto the EMCCD or the APD. This integrated approach assures that measured correlation curves can be compared quantitatively. In standard APD-FCS, the measurement result is typically already the correlation function calculated by a hardware correlator. EMCCD-based FCS, however, involves tailored data acquisition and step-by-step offline data processing of the raw image data. Therefore, we describe in detail the necessary steps to perform EMCCD-FCS (chapter 5), especially with respect to the special camera readout modes employed here. First comparative measurements in solution are presented (chapter 6), followed by a comparison of the performance characteristics of two different EMCCD camera models (chapter 7).

In part III, the first technical application of EMCCD-based spatial resolved FCS is demonstrated by performing dual-focus fluorescence cross-correlation spectroscopy (FCCS), a recently developed method to deduce accurate diffusion coefficients and minute flow speeds. For these precision measurements, the EMCCD data acquisition is further refined and measurements in solution and on membranes are performed (chapters 8 – 10).

Part IV describes the application of FCS in living zebrafish embryos. In particular, it is shown by one- and two-focus FCS that morphogen molecules largely diffuse freely as single molecules in the extracellular space, and a minor slowly diffusing component can be attributed to interactions with extracellular matrix components (chapter 12 – 13). In chapter 14, the observed stable *in vivo* morphogen concentration gradient is discussed. By employing a simple model for the description of morphogen production, propagation and receptor-mediated removal, important parameters such as the half life time of the morphogen are deduced. The study shows that the most simple mechanisms, free diffusion and overall degradation, are used by nature to efficiently traverse the crowded environment of extracellular space and to create a stable morphogen concentration gradient.

Part I.

Theoretical and technological background

Theoretical and technological background

In this part of the thesis, the essential background of fluorescence correlation spectroscopy (FCS) is given. Chapter 2 introduces the theoretical concept of auto- and cross-correlation analysis, and in chapter 3, standard and new detection methods are compared.

We conclude that spatially-resolved, array-based detection is advantageous in adding functionality and providing more flexibility in several FCS variations. In particular, the electron multiplying charge-coupled device (EMCCD) is shown to be a suitable and promising spatially resolved detector for FCS.

2. Fluorescence Correlation Spectroscopy (FCS)

FCS is a single-molecule technique uniquely suited for studying biological processes (1, 2). It is based on detecting fluorescence intensity fluctuations within one or several small confocal volumes (< 0.5 fl) (3). Statistical analysis by autocorrelation or cross-correlation of these fluctuations provides quantitative information on propagation, heterogeneity and concentration of fluorescent molecules present in the system.

The mathematical formulation of auto- and cross-correlation analysis is given in sections 2.3 and 2.4. Before, in sections 2.1 and 2.2, we introduce the necessary basics of fluorescence and the description of the confocal detection volume.

2.1. Basics of fluorescence

Fluorescence is the property of a substance to emit light after it was brought to an electronic excited state. The transitions in the fluorescent material, typically molecules with aromatic groups, are often schematically described by electronic-state diagrams, the Jablonski diagrams (fig. 2.1 a). In these diagrams, electronic levels (energy differences of electron volts, eV) and vibronic sublevels (0.1 eV) are shown. For molecules, a huge number of rotational sublevels (0.001 eV) exists, resulting in continuous excitation and emission band spectra.

At room temperature, only the vibrational ground state of S_0 is predominately occupied, according to the Maxwell-Boltzmann distribution. Due to the Franck-Condon principle, the electron is excited to one of the vibronic first or second electronic excited stages (S_1 or S_2). Excitation by absorption of a single photon is described by the Lambert-Beer law (4):

$$\frac{dI}{dz} = -kI, \quad (2.1)$$

where I is the transmitted intensity of light when traveling a path length z through a material with a one-photon absorption coefficient k . In case of molecules of concentration C , k equals to the product $k = \alpha C$, where α is the molar absorption coefficient. The more commonly used decadic absorption coefficient, called extinction coefficient ϵ , follows by $\epsilon = \alpha / \ln 10$. One-photon absorption depends linearly on the excitation power.

At sufficiently higher excitation power, also two- or more-photon absorption of light with correspondingly longer wavelength can occur. The multi-photon absorption is described by an extended Lambert-Beer law, including non-linear terms in I :

$$\frac{dI}{dz} = -kI - \beta I^2 - \gamma I^3, \quad (2.2)$$

where β and γ are the two- and three-photon absorption coefficients, respectively (5). Two-photon absorption can be utilized for FCS, with advantages when measuring in turbid samples like plant

2. Fluorescence Correlation Spectroscopy (FCS)

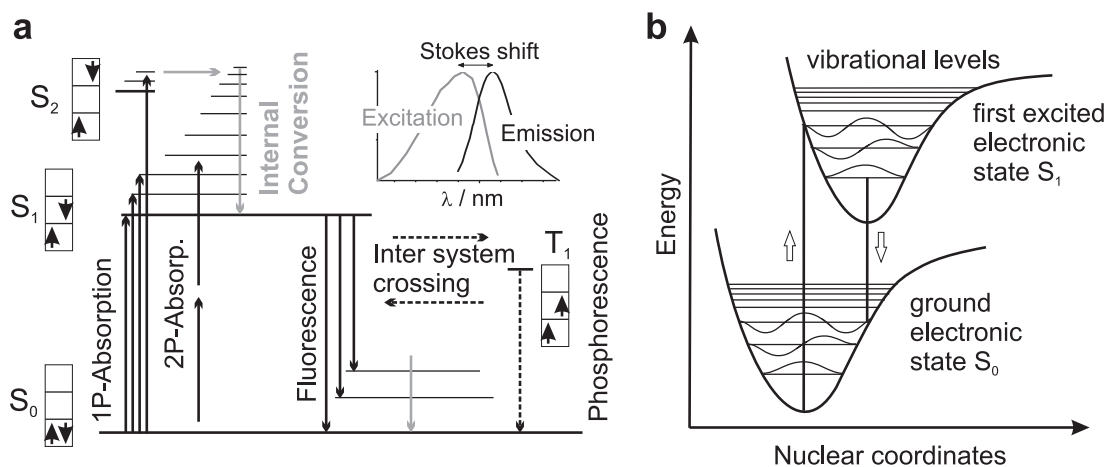


Figure 2.1.: Principle of fluorescence. **a:** Jablonski diagrams of a fluorescent molecule with electronic singlet (S) states with antiparallel spins and the first triplet (T) state with parallel spins. The vibronic levels are given as lines above the electronic levels. A fluorophore is excited (femtoseconds, fs) by absorption of one or two photons, relaxes back non-radiatively to the vibronic ground state (ps) and subsequently emits a fluorescence photon (ns). It also can undergo inter system crossing to the triplet state and emit phosphorescence (ms). **b:** Franck-Condon principle: Electronic transitions are much faster than the nuclear motion, therefore they can be depicted as vertical lines in the energy diagram. Since equilibrium distance of the nuclei is typically higher after excitation, the excitation and emission transitions always end in vibrational excited levels. Therefore, a typical emission spectra exhibits a red shift (Stokes shift) and a mirror symmetry compared to a one-photon excitation spectra (inset in (a)).

cells or at deep cell layers in tissue (6). However, one-photon absorption results in overall higher fluorescence signal per molecule and a better signal-to-noise ratio of the FCS curves. Hence, only one-photon excitation was utilized for all measurements in this thesis.

After excitation, the molecule relaxes back to the vibronic ground state of S_1 or S_2 by internal conversion, which is the energy dissipation by collisions with the solvent molecules. Independent of the absorption process, the molecule subsequently decays to the electronic ground state by emitting a fluorescence photon (rate k_r , radiative decay), or by non-radiative internal conversion (rate k_{ic}). With a much lower probability, intersystem crossing to the meta-stable, comparatively long-lived triplet state can occur (rate k_{is}), from where again radiative (phosphorescence) and non-radiative decay to the ground state is possible. Besides internal conversion, also collisions with other molecules can de-excite the fluorophore, leading to another form of non-radiative decay called fluorescence quenching. The degree of quenching (quenching rate k_q) strongly depends on the concentration of quenching molecules Q .

The quantum yield of the fluorescence is given by the quotient of the rate constants:

$$q = \frac{k_r}{k_r + k_{ic} + k_{is} + k_q(Q)}. \quad (2.3)$$

It represents the number of emitted fluorescence photons, divided by the number of absorbed photons.

Fluorescence transition occurs into a vibrational excited electronic ground state, again due to the Franck-Condon principle (fig. 2.1 b). Therefore, transition energy is lower than the one for excitation. The emission spectra is hence shifted to longer wavelengths compared to the excitation spectra. The distance between the maxima of excitation and emission spectra is called Stokes shift (fig. 2.1 a,

inset). It allows for efficient separation of excitation and fluorescence light with appropriate dichroic filters.

Fluorophores

A perfect fluorophore exhibits a high extinction coefficient, a high quantum yield and high photostability, and it is small in order not to interfere with the system. The fluorescent species used in biologically-related research can be divided into three groups:

A first group are the standard organic dyes, such as fluorescein, rhodamine or cyanine. Although they already have a good molecular brightness, their commercial variants have been further improved. They are now available over the whole spectral range, together with various functional groups attached for labeling of the biomolecules. Advantage is the high brightness, photostability, well-characterized photophysics, and the small size (< 1 kDa, $1 \text{ kDa} = 1000 \text{ g mol}^{-1}$). Efficient labeling and subsequent insertion into the cells for in-vivo measurements, however, can be an elaborate task.

A second group are autofluorescent proteins (7). They can be genetically attached to the proteins of interest, so that the fusion construct is directly expressed by the cells. Fluorescent proteins have already a similar size (20-30 kDa) to typical proteins of interest, hence potential interference with the biological function needs to be carefully investigated. Their brightness and photostability is lower when compared to the best organic fluorophores, and they often exhibit complex photophysical or chemical dynamics that may interfere with the FCS analysis. This is especially the case for the fluorescent proteins in the orange to red spectral range (8). However, for cellular applications, fluorescent proteins like the green fluorescent protein are often the first choice.

A third group are nanoparticles such as semiconductor nanocrystals (9) or nanodiamonds (10). They exhibit a high brightness per particle and extraordinary photostability. Additionally, their narrow emission spectra can be tuned, allowing for multi-color labeling strategies. A disadvantage is their comparably large size (5 to 10 nm) which often exceeds the one of the biomolecules of interest. Also compatibility with biological material, labeling strategies and the blinking dynamics characterization have been a challenge in the past. However, many of these questions have been recently addressed (11, 12), so that nanoparticles are still promising alternatives complementing organic dyes and fluorescent proteins.

2.2. Confocal setup

In order to detect fluorescence fluctuations from small ensembles of single molecules, low concentrations in the nanomolar range and small detection volumes (< 0.5 femtoliters) are needed. The small detection volume is achieved in an epi-illuminated, confocal microscope configuration (1). A collimated laser beam enters the back-focal plane of a high NA objective lens, creating a diffraction limited excitation volume (fig. 2.2). Fluorescence is collected by the same objective lens, passes a dichroic mirror (and additional filters for background light suppression), is focused onto a small confocal aperture of diameter 50-100 μm , and subsequently detected by typically a single-point avalanche photo diode (APD). The confocal principle assures a good axial resolution. The pinhole in the image plane of the microscope tube lens is often replaced by the entrance pupil of a multimode optical fiber, allowing for an easy alignment and simple connection to a fiber-coupled APD.

2. Fluorescence Correlation Spectroscopy (FCS)

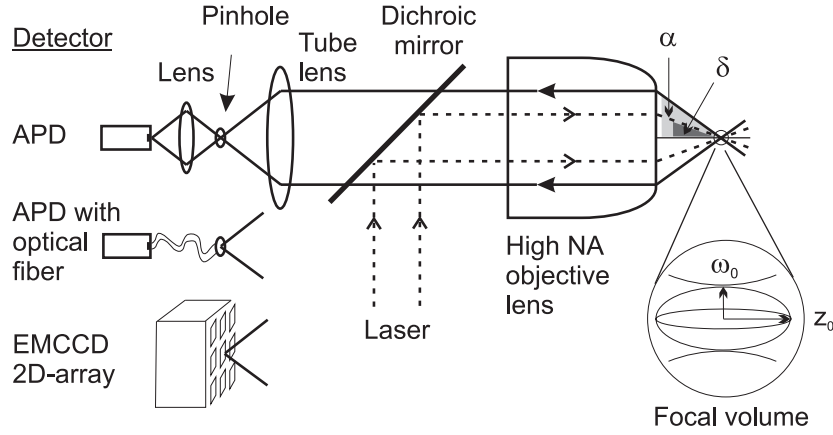


Figure 2.2.: Confocal setup for FCS. A laser is focused to the diffraction limit for excitation. Fluorescence is mapped onto a confocal pinhole for axial resolution, and detected by an APD point detector. The pinhole–lens combination is often substituted by an optical fiber of same core diameter as the pinhole. EMCCD-based detection, presented in this thesis, utilizes the pixels of the camera as a pinhole of tunable size. The focal detection volume can be approximated by a simple three-dimensional Gaussian function, radially symmetric and elongated in the axial direction.

Excitation profile

The excitation intensity profile of the focused laser beam is described by a Gaussian function in lateral direction (x, y) and by a Lorentzian function in axial (z) direction:

$$I_{ex}(\vec{r}) = I_{ex}(r, z) = I_0(z) \cdot e^{-\frac{2r^2}{\omega^2(z)}} \quad (r^2 = x^2 + y^2) \quad (2.4)$$

and:

$$\omega^2(z) = \omega_0^2 + z^2 \tan^2 \delta, \quad I_0(z) = \frac{\omega_0^2 I_0}{\omega^2(z)} \quad (2.5)$$

and:

$$\omega_0 = \frac{\lambda f}{n\pi \omega_L} = \frac{\lambda}{n\pi \tan \delta}. \quad (2.6)$$

The beam waist ω_L is the $1/e^2$ -radius of the collimated laser beam before entering the objective and f is the focal length of the objective lens. The parameter δ is the focus angle, λ is the wavelength of light and n is the index of refraction of the immersion media.

A collimated laser beam with a large width ω_L results in a small focus waist. For confocal imaging, the back aperture of the objective is typically filled by the laser to achieve the smallest possible focus and hence the best spatial resolution. However, for FCS, the back aperture is typically slightly under-filled to better approximate the resulting confocal detection volume by a three-dimensional Gaussian model. The focus angle δ is therefore typically smaller than the detection angle α , which is defined by the numerical aperture $NA = n \sin \alpha$ of the objective.

Detection profile

The detection profile is the intensity distribution of the detected fluorescence light. It is therefore the product of the excitation profile $I_{ex}(\vec{r})$ and the optical transfer function $S(\vec{r})$, including the point spread

function of the objective lens and the pinhole function (1). The detection profile, normalized with the center maximum value I_0 , is called molecule detection function (1) or volume profile (13):

$$W(\vec{r}) = \frac{I_{ex}(\vec{r}) \cdot S(\vec{r})}{I_0}. \quad (2.7)$$

In order to obtain an analytical closed form of the autocorrelation function, the molecule detection function is often approximated by a three-dimensional Gaussian function:

$$W(\vec{r}) = e^{-2\frac{x^2+y^2}{\omega_0^2}} e^{-2\frac{z^2}{z_0^2}}, \quad (2.8)$$

where ω_0 and z_0 are the $1/e^2$ -radii in radial and axial direction, respectively.

This approximation is sufficient for small pinhole sizes where the lateral Gaussian profile is not influenced, but where the z-dependence of the axial Lorentzian profile is suppressed (14). In addition, a perfect description of the molecule detection function is not necessary when FCS is used to determine parameters relative to a reference dye in standard one-focus FCS.

For two-focus FCS, where absolute parameter estimates are obtained, and where precision of FCS measurements is much higher, a generalized Gauss-Lorentz model has been introduced (15). This model better describes the experimental situation of APD-based two-focus FCS, where a single comparably big confocal pinhole is employed for both focal volumes. The correlation function for this model is given in section 2.4.2.

2.3. FCS autocorrelation analysis

In fluorescence correlation spectroscopy, the kinetic properties of the molecules can be studied within the thermodynamic equilibrium of the system. Information are extracted from the naturally occurring temporal fluorescence fluctuations. The fluorescence intensity fluctuations $\delta I(t)$ are defined as:

$$\delta I(t) = I(t) - \langle I(t) \rangle, \quad (2.9)$$

where $\langle \cdot \rangle$ denotes a temporal average over the measurement time T :

$$\langle I(t) \rangle = \frac{1}{T} \int_0^T I(t) dt. \quad (2.10)$$

The normalized autocorrelation function $G(\tau)$ of fluorescence intensity fluctuation $\delta I(t)$ with lag time τ is defined as:

$$G(\tau) = \frac{\langle \delta I(t) \cdot \delta I(t + \tau) \rangle}{\langle I(t) \rangle^2}. \quad (2.11)$$

It describes the self-similarity of the function $I(t)$ to a later time $t + \tau$. The fluctuations can be induced by any process occurring on the molecular level. To be measurable with FCS, the process has to be reversible to give fluctuations within the observation time. The time window is given by the dead time of the detector (<100 ns for an APD) and the residence time of the molecules in the focal volume ($10 \mu\text{s} - \text{s}$). For the simplest case of intensity fluctuations arising from one species of molecules in solution that freely diffuse through a three-dimensional Gaussian detection volume, we derive the autocorrelation function in detail. For the other cases relevant to this thesis, we briefly give the approach and result. A thorough general mathematical treatment can be found in reference (13).

2. Fluorescence Correlation Spectroscopy (FCS)

2.3.1. Diffusion

The most prominent source of fluctuations evaluated by FCS are the intensity fluctuations due to Brownian translational diffusion. At constant macroscopic concentration $\langle C \rangle$, the local concentration within a small confocal volume V_0 fluctuates (fig. 2.3 a). The number of particles within the volume is Poisson-distributed, expressed by the equality of variance $\langle \delta N^2 \rangle$ and mean value $\langle N \rangle$, hence:

$$\langle \delta C^2 \rangle = \frac{\langle \delta N^2 \rangle}{V_0^2} = \frac{\langle N \rangle}{V_0^2} = \frac{\langle C \rangle}{V_0}. \quad (2.12)$$

In the limit of an infinitesimal small volume, we get:

$$\phi(\vec{r}, \vec{r}', 0) = \langle \delta C(\vec{r}, 0) \delta C(\vec{r}', 0) \rangle = \langle C \rangle \delta(\vec{r} - \vec{r}'). \quad (2.13)$$

The last equation is the concentration correlation function at time $\tau = 0$, which means that concentration fluctuations at the same time are only correlated at the same spatial coordinate. The general term for the concentration correlation function $\phi(\vec{r}, \vec{r}', \tau)$ reads:

$$\phi(\vec{r}, \vec{r}', \tau) = \langle \delta C(\vec{r}, t) \delta C(\vec{r}', t + \tau) \rangle = \langle \delta C(\vec{r}, 0) \delta C(\vec{r}', \tau) \rangle, \quad (2.14)$$

where $t = 0$ can be chosen due to the assumption that the system is stationary. The function can be derived from the diffusion equation (13, 16):

$$\frac{\partial C(\vec{r}, t)}{\partial t} = D \nabla^2 C(\vec{r}, t). \quad (2.15)$$

The diffusion coefficient D for spherical particles in solution can be calculated by the Stokes-Einstein-relation:

$$D = \frac{k_b T}{6\pi \eta r}, \quad (2.16)$$

where k_b is Boltzmann's constant, T is the absolute temperature, η is the viscosity of the medium, and r is the hydrodynamic radius. The diffusion coefficient depends on the temperature directly (equation 2.16) and indirectly via the temperature dependence of the viscosity, which can be given for water (17):

$$\log \left(\frac{\eta_w(\vartheta)}{\eta_w(20^\circ \text{C})} \right) = \frac{20 - \vartheta}{\vartheta + 96} \left[1.2364 - 1.37 \cdot 10^{-3}(20 - \vartheta) + 5.7 \cdot 10^{-6}(20 - \vartheta)^2 \right], \quad (2.17)$$

where ϑ is the temperature in degree Celsius and $\eta_w(20^\circ \text{C}) = 1.003 \text{ mPas}$. At temperatures around room temperature, as used in our measurements, D changes by approximately 2% for every degree.

From equation 2.15 and the definition of the concentration fluctuation:

$$\delta C(\vec{r}, t) = C(\vec{r}, t) - \langle C \rangle, \quad (2.18)$$

it follows as well:

$$\frac{\partial(\delta C(\vec{r}, t))}{\partial t} = D \nabla^2(\delta C(\vec{r}, t)). \quad (2.19)$$

As boundary condition, the concentration fluctuations are assumed to be zero at infinity:

$$\lim_{|\vec{r}| \rightarrow \infty} (\delta C(\vec{r}, t)) = 0. \quad (2.20)$$

Equation 2.19 can be solved by Fourier transformation:

$$\frac{\partial(\delta\tilde{C}(\vec{k}, t))}{\partial t} = -D k^2(\delta\tilde{C}(\vec{k}, t)) \quad (2.21)$$

and the solution in \vec{k} -space is:

$$\delta\tilde{C}(\vec{k}, t) = \delta\tilde{C}(\vec{k}, 0) e^{-D k^2 t}. \quad (2.22)$$

Now we can directly calculate the concentration correlation function (equation 2.14):

$$\begin{aligned} \phi(\vec{r}, \vec{r}', \tau) &= F_r^{-1}\{\langle\delta C(\vec{r}, 0) \delta\tilde{C}(\vec{k}, \tau)\rangle\} \\ &= F_r^{-1}\{\langle\delta C(\vec{r}, 0) \delta\tilde{C}(\vec{k}, 0)e^{-D k^2 \tau}\rangle\} \\ &= F_r^{-1}\{e^{-D k^2 \tau} F_k\{\langle\delta C(\vec{r}, 0) \delta C(\vec{r}', 0)\rangle\}\} \\ &= F_r^{-1}\{e^{-D k^2 \tau} F_k\{\phi(\vec{r}, \vec{r}', 0)\}\} \\ &= F_r^{-1}\{e^{-D k^2 \tau} F_k\{\langle C\rangle\delta(\vec{r} - \vec{r}')\}\} \\ &= \frac{\langle C\rangle}{(2\pi)^3} \int_{-\infty}^{\infty} d^3k e^{-D\tau k^2 - i(\vec{r} - \vec{r}')\vec{k}} \\ \phi(\vec{r}, \vec{r}', \tau) &= \langle C\rangle \frac{1}{\sqrt{4\pi D\tau}^3} e^{-\frac{(\vec{r} - \vec{r}')^2}{4D\tau}}. \end{aligned} \quad (2.23)$$

This function is the product of the mean concentration and the conditional probability that a molecule is found at position \vec{r}' and time τ , after it was present at \vec{r} and time 0.

Using the theoretical concentration correlation (equation 2.23), we now want to calculate the experimentally measurable correlation of the fluorescence fluctuations (equation 2.11). The fluorescence intensity and its fluctuations do not only depend on the concentration, but also on the spatial distribution of the excitation intensity $I_{ex}(\vec{r})$, the molecular absorption cross-section σ and quantum yield q , and the overall detection efficiency κ and spatial fluorescence collection efficiency $S(\vec{r})$ of the optical setup:

$$\delta I(t) = \kappa \cdot \sigma \cdot q \int_V I_{ex}(\vec{r}) \cdot S(\vec{r}) \cdot \delta C(\vec{r}, t) dV. \quad (2.24)$$

For simplicity, all parameters apart from the concentration are assumed to be time-independent. The product of the two spatial distributions, normalized with the center maximum value I_0 , was called molecule detection function $W(\vec{r})$ (equation 2.7). The product of the other factors, together with I_0 , is the molecular brightness:

$$\eta_0 = \kappa \cdot \sigma \cdot q \cdot I_0, \quad (2.25)$$

which determines the detected count rate per particle and second (cpps) in an FCS measurement. It is important for the signal-to-noise ratio and can serve as a reference value to compare setups or different fluorescent molecules. The fluorescence intensity fluctuation (equation 2.24) now reads:

$$\delta I(t) = \eta_0 \cdot \int_V W(\vec{r}) \delta C(\vec{r}, t) dV. \quad (2.26)$$

The normalized autocorrelation function $G(\tau)$ (equation 2.11) can be calculated in an analytical closed form if we use the derived concentration correlation function (equation 2.23) and the simple

2. Fluorescence Correlation Spectroscopy (FCS)

three-dimensional Gaussian approximation of the detection volume (equation 2.8):

$$\begin{aligned}
G(\tau) &= \frac{\langle \delta I(t) \cdot \delta I(t + \tau) \rangle}{\langle I(t) \rangle^2} \\
&= \frac{\int \int W(\vec{r}) W(\vec{r}') \langle \delta C(\vec{r}, t) \delta C(\vec{r}', t + \tau) \rangle dV dV'}{(\int W(\vec{r}) \langle C(\vec{r}, t) \rangle dV)^2} \\
&= \frac{\int \int W(\vec{r}) W(\vec{r}') \phi(\vec{r}, \vec{r}', \tau) dV dV'}{(\langle C \rangle \int W(\vec{r}) dV)^2} \\
&= \frac{\int_{-\infty}^{\infty} \int_{-\infty}^{\infty} W(\vec{r}) W(\vec{r}') \langle C \rangle e^{-\frac{(\vec{r}-\vec{r}')^2}{4D\tau}} dV dV'}{\sqrt{4\pi D\tau}^3 (\langle C \rangle \int_{-\infty}^{\infty} W(\vec{r}) dV)^2} \\
&= \frac{\int_{-\infty}^{\infty} \int_{-\infty}^{\infty} e^{-2\frac{x^2+y^2}{\omega_0^2} - 2\frac{z^2}{z_0^2}} \cdot e^{-2\frac{x'^2+y'^2}{\omega_0^2} - 2\frac{z'^2}{z_0^2}} \langle C \rangle e^{-\frac{(\vec{r}-\vec{r}')^2}{4D\tau}} dV dV'}{\sqrt{4\pi D\tau}^3 (\langle C \rangle \int_{-\infty}^{\infty} e^{-2\frac{x^2+y^2}{\omega_0^2} - 2\frac{z^2}{z_0^2}} dV)^2} \\
G(\tau) &= \frac{1}{\pi^{3/2} \omega_0^2 z_0 \langle C \rangle} \left(\frac{1}{1 + \frac{4D\tau}{\omega_0^2}} \cdot \frac{1}{\sqrt{1 + \frac{\omega_0^2}{z_0^2} \frac{4D\tau}{\omega_0^2}}} \right). \tag{2.27}
\end{aligned}$$

The autocorrelation function $G(\tau)$ (equation 2.27) has four parameters: the lateral and axial dimensions ω_0 and z_0 of the detection volume, the mean concentration $\langle C \rangle$ and the diffusion coefficient D . Not all four physical parameters can be obtained from fitting an experimental autocorrelation curve to this model function, since the shape of the function only depends on three parameters. Introducing these three parameters, the function reads:

$$G(\tau) = \frac{1}{N} \left(\frac{1}{1 + \frac{\tau}{\tau_D}} \cdot \frac{1}{\sqrt{1 + \frac{1}{S^2} \frac{\tau}{\tau_D}}} \right), \tag{2.28}$$

and the interpretation is the following (fig. 2.3):

- The dimensionless parameter N is the mean number of particles in the effective detection volume, which is defined as V_{eff} :

$$V_{eff} = \frac{(\int W(\vec{r}) dV)^2}{\int W^2(\vec{r}) dV} = \pi^{3/2} \omega_0^2 z_0. \tag{2.29}$$

N is the inverse of the so-called amplitude $G(0)$ of the autocorrelation function. If the dimensions of the detection volume are known, the concentration can be calculated.

- The time constant τ_D is called (transversal) diffusion time:

$$\tau_D = \frac{\omega_0^2}{4D}. \tag{2.30}$$

If ω_0 is known, the diffusion coefficient can be calculated. The diffusion time τ_D is the lag time τ at which the correlation function has decayed by approximately half of its amplitude.

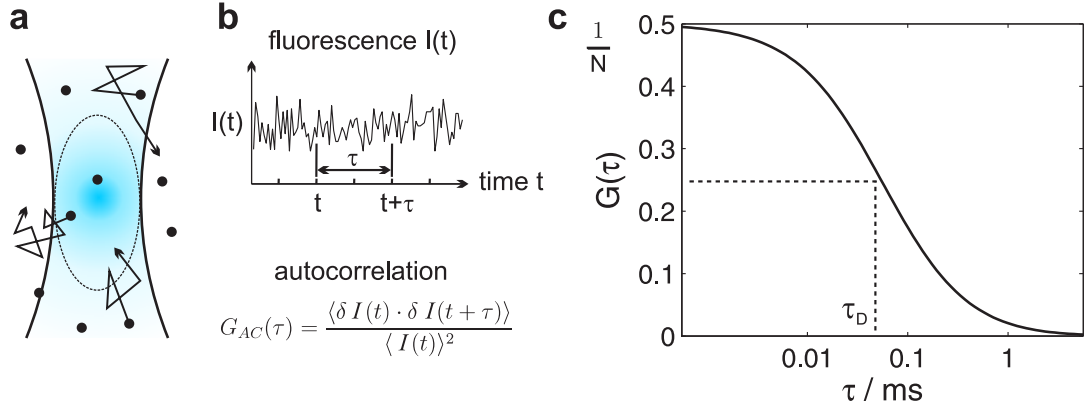


Figure 2.3.: FCS autocorrelation curve. **a:** Schematic drawing of the confocal detection volume (see fig. 2.2) with molecules diffusing in and out. **b:** Fluorescence intensity fluctuations are auto-correlated over time. **c:** Experimentally obtained autocorrelation curves are fit with appropriate model functions, here equation 2.28 is plotted with parameters $N = 2$, $S = 5$, and $\tau_D = 56 \mu s$ ($D = 400 \mu m^2/s$, and $\omega_0 = 0.3 \mu m$).

Mathematically, it exactly decays by half for an axially infinitely extended volume ($z_0 \rightarrow \infty$ in the last factor in equation 2.27), where the axial component of the diffusion doesn't contribute to the shape of the curve any more. The real case for this is the two-dimensional diffusion, for example in a planar membrane (see below).

- The dimensionless parameter S is called structure parameter:

$$S = \frac{z_0}{\omega_0}, \quad (2.31)$$

which is the axial-to-lateral aspect ratio of the ellipsoidal three-dimensional Gaussian detection volume. Depending on the optical setup, its theoretical value is between 2–3. The experimental fit value is typically a bit higher and between 3 – 6 due to the slightly non-Gaussian detection volume under one-photon excitation (18). Nevertheless, S serves as a good control parameter of the setup since it can be easily out of this range or can diverge in case of a severe non-Gaussian detection volume.

A fourth important parameter of an FCS measurement is the effective molecular brightness η_{eff} :

$$\eta_{eff} = \frac{\langle I(t) \rangle}{N}. \quad (2.32)$$

It can be directly calculated from the average photon count rate and the fit parameter particle number and its unit is counts per particle and second (cpps). The signal-to-noise ratio of the FCS curve depends quadratically on this parameter (19).

To obtain the important fit parameters concentration C and diffusion coefficient D from an autocorrelation measurement, the detection volume has to be calibrated before. This calibration is typically done by measuring the autocorrelation curve of a fluorescent dye of well known diffusion coefficient D_1 . Then the diffusion coefficient D_2 of the biomolecule of interest can be easily calculated (equation 2.30) by:

$$D_2 = D_1 \cdot \frac{\tau_{D,1}}{\tau_{D,2}}. \quad (2.33)$$

2. Fluorescence Correlation Spectroscopy (FCS)

The exact values of ω_0 and S are not important, as long as they are constant in both measurements. This can be assumed, for example, if the biomolecule of interest is labeled with the same dye that is used for calibration. Otherwise, the different photophysical properties of the two dyes, for example photobleaching (20, 21) or fluorescence saturation (22–24), can lead to different effective detection volumes and hence influence the result. This uncertainty can be overcome by spatial cross-correlation in a two-focus FCS setup (section 2.4.2), where no calibration measurement is needed anymore.

Two-dimensional diffusion

For a two-dimensional system like diffusion in a horizontal planar membrane, the autocorrelation function can be obtained by assuming a two-dimensional Gaussian molecule detection function. The concentration correlation function reads:

$$\phi(\vec{r}, \vec{r}', \tau) = \langle C \rangle \frac{1}{4\pi D\tau} e^{-\frac{(\vec{r}-\vec{r}')^2}{4D\tau}}, \quad (2.34)$$

and the autocorrelation function simplifies to:

$$G_{2D}(\tau) = \frac{1}{N} \frac{1}{1 + \frac{\tau}{\tau_D}}. \quad (2.35)$$

The definition of the diffusion time (equation 2.30) is the same. However, N is now the particle number within the effective detection area $A_{eff} = \pi\omega_0^2$ and $\langle C \rangle$ is an area concentration.

Diffusion of multiple species of molecules

In the case of more than one diffusing, non-interacting species, the autocorrelation function $G(\tau)$ is the weighted superposition of the individual autocorrelation functions. This will be shown in the following.

The fluorescence intensity fluctuations (equation 2.26) of n species are:

$$\delta I(t) = \sum_{i=1}^n \delta I_i(t) = \int W(\vec{r}) \sum_{i=1}^n \eta_i \delta C_i(\vec{r}, t) dV. \quad (2.36)$$

The molecular brightnesses η_i can be different but they are again assumed to be constant. The normalized autocorrelation function reads:

$$\begin{aligned} G(\tau) &= \frac{\langle \delta I(t) \cdot \delta I(t + \tau) \rangle}{\langle I(t) \rangle^2} \\ &= \frac{\int \int W(\vec{r}) W(\vec{r}') \sum_{i=1}^n \sum_{j=1}^n \eta_i \eta_j \langle \delta C_i(\vec{r}, t) \delta C_j(\vec{r}', t + \tau) \rangle dV dV'}{(\int W(\vec{r}) \sum_{i=1}^n \eta_i \langle C_i(\vec{r}, t) \rangle dV)^2} \\ G(\tau) &= \frac{\int \int W(\vec{r}) W(\vec{r}') \sum_{i=1}^n \sum_{j=1}^n \eta_i \eta_j \phi_{ij}(\vec{r}, \vec{r}', \tau) dV dV'}{(\sum_{i=1}^n \eta_i \langle C_i \rangle)^2 \cdot (\int W(\vec{r}) dV)^2}. \end{aligned} \quad (2.37)$$

The concentration correlation functions $\phi_{ij}(\vec{r}, \vec{r}', \tau)$ are zero for $i \neq j$, since the diffusion of one species is not correlated with the diffusion of another one if there is no interaction. The concentration fluctuations $\delta C_i(\vec{r}', t)$ of each species i obey the diffusion equation:

$$\frac{\partial(\delta C_i(\vec{r}, t))}{\partial t} = D_i \nabla^2(\delta C_i(\vec{r}, t)), \quad (2.38)$$

and for $i = j$, we obtain the known concentration correlation function in case of three-dimensional diffusion (equation 2.23):

$$\phi_{ii}(\vec{r}, \vec{r}', \tau) = \phi_i(\vec{r}, \vec{r}', \tau) = \langle C_i \rangle \frac{1}{\sqrt{4\pi D_i \tau}} e^{-\frac{(\vec{r}-\vec{r}')^2}{4D_i \tau}}. \quad (2.39)$$

If we plug equation 2.39 in equation 2.37, it follows:

$$G(\tau) = \frac{\sum_{i=1}^n [\eta_i \langle C_i \rangle]^2 \cdot G_i(\tau)}{\left[\sum_{j=1}^n \eta_j \langle C_j \rangle \right]^2} = \frac{\sum_{i=1}^n [\eta_i N_i]^2 \cdot G_i(\tau)}{\left[\sum_{j=1}^n \eta_j N_j \right]^2} = \frac{\sum_{i=1}^n \langle I_i(t) \rangle^2 \cdot G_i(\tau)}{\left[\sum_{j=1}^n \langle I_j(t) \rangle \right]^2}, \quad (2.40)$$

where $G_i(\tau)$ is the known autocorrelation function of each single species (equations 2.27 and 2.28):

$$G_i(\tau) = \frac{1}{V_{eff} \langle C_i \rangle} \left(\frac{1}{1 + \frac{4D_i \tau}{\omega_0^2}} \cdot \frac{1}{\sqrt{1 + \frac{4D_i \tau}{z_0^2}}} \right) = \frac{1}{N_i} \left(\frac{1}{1 + \frac{\tau}{\tau_{D,i}}} \cdot \frac{1}{\sqrt{1 + \frac{1}{S^2} \frac{\tau}{\tau_{D,i}}}} \right). \quad (2.41)$$

The resulting autocorrelation function is therefore the weighted sum of the individual autocorrelation functions. The weighting factor is the square of the fractional intensities.

Note that the weighting factors in equation 2.40 depend to the same extend on the molecular brightness η_i and the concentration C_i (or equivalent the particle number N_i). However, the representation of the individual temporal decay in the resulting summed autocorrelation curve depends on the square of the molecular brightness but only linear on the concentration of the individual species. This is due to the fact that individual autocorrelation curves (equation 2.41) are weighted by their inverse concentration or particle number already. Given an example that there are two species and the first one has a double molecular brightness than the second one, we have to use four times the concentration of the second species to get the same influence of both species on the resulting autocorrelation curve. The intensity (fluorescence count rate) of the second species is double of that of the first species in this case.

In general, distinguishing more than two species by FCS is rather difficult. For the different species, not only the product of the concentration and the square of the molecular brightness needs to be similar, but also their diffusion coefficients have to be sufficiently different (at least by factor 1.6 (25) for two species) to obtain a separation of the components. Additional, two additional fit parameters for each component (a fraction and a time constant) will rapidly result in too many free parameters so that even an excellent fit result loses its physical meaning. In practice, only two component models are mostly employed. Additionally, one can typically assume that the molecular brightness is the same for both species. Then, equation 2.40 simplifies to:

$$G(\tau) = \frac{1}{N_{total}} \left(\frac{F}{\left(1 + \frac{\tau}{\tau_{D,1}}\right) \cdot \sqrt{1 + \frac{1}{S^2} \frac{\tau}{\tau_{D,1}}}} + \frac{1-F}{\left(1 + \frac{\tau}{\tau_{D,2}}\right) \cdot \sqrt{1 + \frac{1}{S^2} \frac{\tau}{\tau_{D,2}}}} \right), \quad (2.42)$$

where N_{total} is the total number of particles in the effective detection volume:

$$N_{total} = N_1 + N_2, \quad (2.43)$$

and F is the fraction of molecules of the first species (fig. 2.4):

$$F = \frac{N_1}{N_{total}} \quad \text{and} \quad 1 - F = \frac{N_2}{N_{total}}. \quad (2.44)$$

2. Fluorescence Correlation Spectroscopy (FCS)

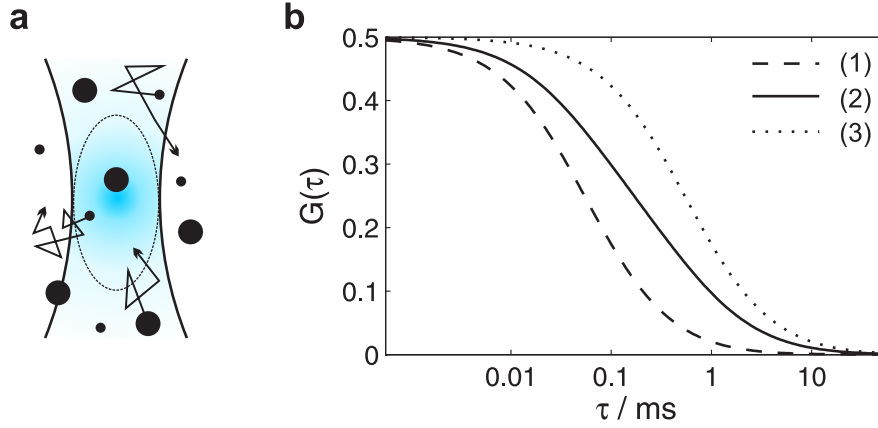


Figure 2.4.: FCS autocorrelation curve for a mixture of two molecular species of distinct molecular mass. **a:** Schematic drawing of the focal detection volume with two species of molecules diffusing in and out. The species two has a ten times smaller diffusion coefficient ($D=40 \mu\text{m}^2/\text{s}$), which means a ten times larger hydrodynamic radius and hence factor 1000 higher molecular mass. **b:** Autocorrelation curve (1) is the same as in fig. 2.3 c for one molecule species with $D=400 \mu\text{m}^2/\text{s}$. FCS curve (3) would be obtained for one molecule species with $D=40 \mu\text{m}^2/\text{s}$. FCS curve (2) is the representation for the 1:1 mixture ($F = 0.5$ in equation 2.42) of both species, as depicted in (a).

2.3.2. Fast blinking processes

The simple assumption of a constant molecular brightness (equation 2.26) is not fulfilled for most fluorophores. Additional fluctuation can arise from changes in the dynamic fluorescence properties of the particles while being inside the detection volume. The most prevalent phenomenon is induced by the reversible transition of the molecule into the quantum mechanically forbidden first excited triplet state (triplet blinking) (26) (fig. 2.1 a). Also, pH dependent reversible protonation of the fluorophore has been described for fluorescent proteins such as eGFP (protonation blinking) (27). The resulting repetitive fast fluorescence intermittence can be seen in the correlation curves as additional shoulders in the fast, typically μs time range (fig. 2.5).

To account for these fluctuations in the model autocorrelation function, these processes are usually approximated by an unimolecular one-step reaction between a bright state B and a dark state D , and rate coefficients k_1 and k_{-1} , respectively.



In case of an unchanged diffusion coefficient for both states, and the assumption that the blinking relaxation time constant τ_T is sufficiently faster (typically one order of magnitude) than the diffusion time, both processes can be separated. The resulting autocorrelation curve can then be expressed as a product of an exponential blinking term and the usual function accounting for the diffusion (equation 2.28):

$$G(\tau) = X_{trip}(\tau) \cdot G_{diff}(\tau) \quad (2.46)$$

and finally reads for one component:

$$G(\tau) = \frac{1}{N_{\text{total}}} \frac{(1 - T + T e^{-\frac{\tau}{\tau_T}})}{1 - T} \frac{1}{1 + \frac{\tau}{\tau_D}} \cdot \frac{1}{\sqrt{1 + \frac{\omega_0^2}{z_0^2} \frac{\tau}{\tau_D}}} \quad (2.47)$$

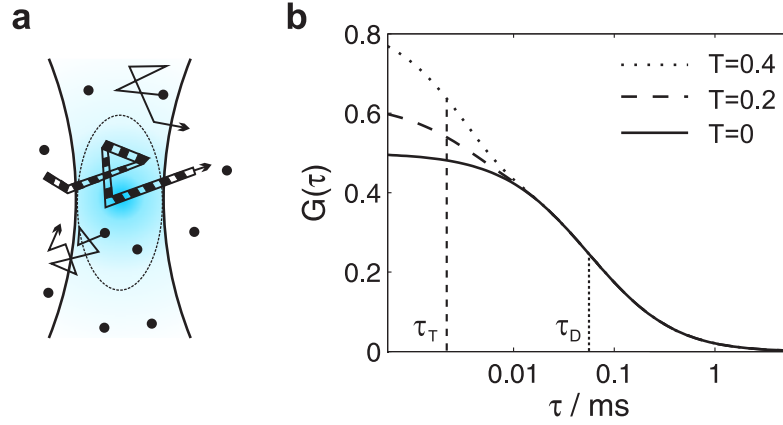


Figure 2.5.: FCS autocorrelation curve including triplet blinking. **a:** Schematic drawing of a molecule diffusing through the focal detection volume with fast fluorescence intermittence due to the transition to the triplet state. **b:** In case of triplet dynamics, the autocorrelation curve exhibits an additional shoulder in the μs time range ($\tau_D = 56 \mu\text{s}$, triplet relaxation time $\tau_T = 3 \mu\text{s}$, triplet fraction $T = 0$ to 0.4).

The blinking (or triplet) fraction T is the mean fraction of molecules in the dark state ($N_{\text{dark}} = T \cdot N_{\text{total}}$) or the mean fraction of the time one molecule remains dark.

2.3.3. Transport and flow

In addition to random free diffusion, molecules can move in a directional manner. For example, this can be a pure active transport of a tightly bound cargo molecule or vesicle in a cellular process. Or it can be a laminar flow superimposed on the free diffusion of molecules, for example the blood flow *in vivo* or the flow in a small channel used in microfluidics *in vitro*. Whether flow or diffusion dominate the propagation of the molecules in this case depends on the diffusion coefficient, the flow speed, and the length or time scale which is considered.

The concentration of the molecules and their fluctuations are described by the advection-diffusion equation that is given for one species of molecules by:

$$\frac{\partial(\delta C(\vec{r}, t))}{\partial t} = D \nabla^2(\delta C(\vec{r}, t)) - \vec{v}(\vec{r}, t) \cdot \nabla(\delta C(\vec{r}, t)), \quad (2.48)$$

where $\vec{v}(\vec{r}, t)$ is the vector of the transport or flow speed. The concentration correlation function is similar to the one for diffusion only (equation 2.23):

$$\phi(\vec{r}, \vec{r}', \tau) = \langle C \rangle \frac{1}{\sqrt{4\pi D \tau}} e^{-\frac{(\vec{r}-\vec{r}'-\vec{v}\tau)^2}{4D\tau}}. \quad (2.49)$$

For the usual considered case that the flow is present only in the xy -plane: $\vec{v} = (v_x, v_y)$, and having the norm of $v = |\vec{v}|$, the autocorrelation $G(\tau)$ is:

$$G(\tau) = \frac{1}{N} \left(\frac{1}{1 + \frac{4D\tau}{\omega_0^2}} \cdot \frac{1}{\sqrt{1 + \frac{4D\tau}{S^2\omega_0^2}}} \right) \cdot \exp\left(\frac{-v^2\tau^2}{\omega_0^2 + 4D\tau}\right). \quad (2.50)$$

This is just the autocorrelation function for diffusion (equation 2.28), multiplied with an exponential flow term. For $v = 0$, we recover the function for diffusion only, and for $D = 0$, we are left with the

2. Fluorescence Correlation Spectroscopy (FCS)

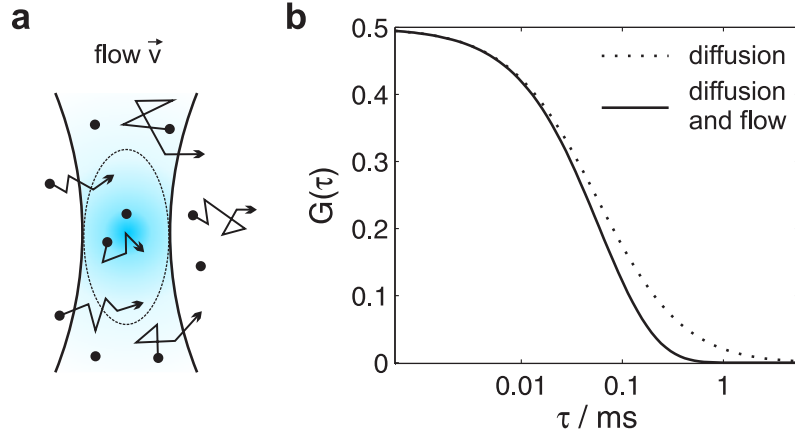


Figure 2.6.: FCS autocorrelation curve for diffusion and flow. **a:** Schematic drawing of the detection volume with molecules moving by diffusing and flow. **b:** In case of a flow superimposed on diffusion, the autocorrelation curve decay is steeper compared to the one in case of diffusion only ($D = 400 \mu\text{m}^2/\text{s}$, flow speed $v = 3 \text{ mm/s}$).

exponential function which describes the pure active transport. If both are present, then due to a flow in addition to diffusion, molecules spend less time in the detection volume, and hence the correlation function decays steeper than the one in pure diffusion (fig. 2.6). The autocorrelation function only depends on the magnitude of the velocity, therefore it is not sensitive to the flow direction.

2.3.4. Artefacts in FCS

In the derivations of the autocorrelation functions above, even for the simplest case of free diffusion, there have been used many simplifying assumptions. The Gaussian detection volume (equation 2.8), for example, is the commonly used assumption because it yields a simple, analytical fit function, and experimental data can be quickly fit to this general model. However, to obtain results with high precision, for example absolute diffusion coefficients or concentrations, special care has to be taken to account for potential systematic errors introduced by these simplifications and a number of other sources of artefacts of FCS. We briefly explain and classify the most common ones in this section.

Optical and sample artefacts arise from non-idealities of the optical setup in combination with the optical properties of the sample. These can be, for example, astigmatism of the laser or of any element in the optical path, a varying cover slide thickness or a mismatch of the refractive index of the sample compared to the design value of the immersion objective. Such non-idealities lead to distortions of the detection volume, and errors in diffusion coefficient and concentration can easily be as high as factor two. However, these sources of errors have been intensively studied and methods to avoid or correct them have been given (28, 29). In particular, two-focus FCS is robust against most of these artefacts (15, 30).

Detector artefacts result from the limited time resolution, stability or reliability of the detected signal. In the mostly employed avalanche photodiodes (APD), the incident photon creates an avalanche of electrons and holes which only then result in a measurable current. After the detection of the photon, this avalanche is actively quenched and all charges need to be completely deleted before the next photon can be detected.

The dead time of the APD is this cycle time of avalanche creation and subsequent quenching, typically about 70 ns. This finite dead time in turn limits the maximal detectable count rate, typically

about 15 MHz. Even well below this maximal saturation value, APDs can be nonlinear. However, FCS typically employs count rates below 500 kHz, due to the very low number of molecules in the detection volume and limited molecular brightness of the fluorophores. In this range of count rates, APDs can be assumed to be linear.

Another related effect is detector afterpulsing. It results from remaining charges of the avalanche in the device that are amplified and detected again although no second photon was present. In the FCS curve, this leads to a strong correlation for short lag times, which can preclude the analysis of real phenomena like triplet dynamics or fast diffusion. The problem of afterpulsing can be overcome by splitting the fluorescence light, detecting it with two detectors and cross-correlating both signals, by performing a calibration experiment and subsequent mathematical correction (31), or by using the fluorescence lifetime to discriminate the afterpulsing from the true fluorescence signal (32).

Furthermore, temporal stability of the detection and a low number of detector dark counts are important. For the standard detector APD, stability is very good, and dark counts are sufficiently low (≈ 250 Hz), when compared to the detected fluorescence photon count rates of typically tens to hundreds of kHz. However, for novel detectors like the electron multiplying CCD camera, employed in this thesis, the detection linearity, baseline stability and dark counts are of prime importance to obtain reliable FCS curves.

Photophysical artefacts are due to the generally limited number of photons a molecule can emit and due to sometimes complex photophysical and photochemical processes inherent in the fluorescence emission. These processes are typically not completely accounted for in the fitting model.

Fluorescence saturation is the effect, that with linearly increasing intensity of the laser excitation, the resulting fluorescence signal does not increase linearly any more. As a result, the effective detection volume is flattened and enlarged, leading to an apparent longer diffusion time and higher concentration. However, at the same time, an opposite effect can occur.

Bleaching of fluorescent molecules, that is, irreversible photodestruction leads to an apparent reduced diffusion time and concentration. Both effects can be linked to triplet processes. In case of a finite reservoir of fluorophores, for example in cells or other small compartments, even the overall fluorescence signal can decrease, leading to a non-steady state of the system, where this effect dominates the correlation curve. An excitation laser power well below the saturation and bleaching onset can help to minimize these effects. However, this is not always possible when a moderate laser power has to be employed to acquire enough photons in a given observation time window. A number of studies have therefore proposed different methods to account for saturation and bleaching in the fitting model (21–24, 31, 33, 34). Two-focus FCS can improve the accuracy of FCS measurements also in case of photophysical artefacts (30, 35).

Background artefacts are due to detected signal that doesn't origin from the fluorophores of interest in the detection volume. These can be instrumentation related non-idealities like laser excitation stray light or detector dark counts, as mentioned above, which can be avoided or minimized rather easily. However, also the sample itself can introduce a background, for example Raman scattering or autofluorescence of the buffer. Additionally, the focal volume can be distorted in biological dense samples which can lead to a significant out-of-focus fluorescence detection.

Usually, it can be assumed, that these sources yield an uncorrelated background B , which only contributes to the normalization of the autocorrelation curve (equation 2.11). It results in a reduced autocorrelation amplitude and hence apparent higher concentration, and it can therefore easily be corrected by:

$$G(\tau)^{\text{corr}} = \frac{(I + B)^2}{I^2} G(\tau)^{\text{meas}}. \quad (2.51)$$

2. Fluorescence Correlation Spectroscopy (FCS)

In equation 2.51, B is the average background intensity, I is the average (background corrected) intensity of the fluorophores, and $G(\tau)^{\text{meas}}$ and $G(\tau)^{\text{corr}}$ are the measured and corrected autocorrelation curves, respectively. The value of the deduced diffusion coefficient is not influenced by an uncorrelated background.

A correlated background $B(t)$ can be accounted for by using a multi-component fit or by independently measuring the autocorrelation curve of the background $G_B(\tau)$ and correcting the obtained autocorrelation curve:

$$G(\tau)^{\text{corr}} = \frac{(I + B)^2 G(\tau)^{\text{meas}} - B^2 G_B(\tau)}{I^2}. \quad (2.52)$$

2.4. FCS cross-correlation analysis

In fluorescence cross-correlation spectroscopy, the fluorescence fluctuations from two detection volumes are compared. These can be two spectrally different and spatially overlapping detection volumes, in which case one evaluates a spectral cross-correlation. Or one can employ two spatially offset and otherwise equal detection volumes, to calculate a spatial cross-correlation. In this section, we briefly give the mathematical framework. The technological implementations, mainly with respect to the detection methods, are discussed in chapter 3.

2.4.1. Spectral cross-correlation

Spectral cross-correlation, also called dual-color or two-color cross-correlation, is a very important and elegant method to measure the interaction between two species of molecules (36). The species are labeled with fluorophores of distinct emission spectra. Both fluorophores are excited by typically two overlapping laser foci of different wavelength, and their fluorescence signals are detected in two spectral separate channels. The fluorescence intensity fluctuation $\delta I(t)$ in the two channels, which we name here green (g) and red (r) channel, are according to equation 2.36 with $n = 2$:

$$\delta I_g(t) = \int W(\vec{r}) \eta_g (\delta C_g(\vec{r}, t) + \delta C_{gr}(\vec{r}, t)) dV \quad (2.53)$$

$$\delta I_r(t) = \int W(\vec{r}) \eta_r (\delta C_r(\vec{r}, t) + \delta C_{gr}(\vec{r}, t)) dV, \quad (2.54)$$

where $C_g(\vec{r}, t)$, $C_r(\vec{r}, t)$ and $C_{gr}(\vec{r}, t)$ are the concentrations of the single labeled green and red, and the double labeled species, respectively. For simplicity, we have assumed here, that both detection volumes overlap completely and are of same size, there is a perfect spectral separation of the two fluorophores, and molecular brightnesses η don't change upon binding. We can now evaluate the two autocorrelation functions (equation 2.40 with $n = 2$):

$$G_g(\tau) = \frac{\langle C_g \rangle \cdot M_g(\tau) + \langle C_{gr} \rangle \cdot M_{gr}(\tau)}{(\langle C_g \rangle + \langle C_{gr} \rangle)^2} \quad (2.55)$$

$$G_r(\tau) = \frac{\langle C_r \rangle \cdot M_r(\tau) + \langle C_{gr} \rangle \cdot M_{gr}(\tau)}{(\langle C_r \rangle + \langle C_{gr} \rangle)^2}, \quad (2.56)$$

where the functions $M_i(\tau)$ denote the motion terms (without the concentration in the denominator) of the autocorrelations functions for the individual species (equation 2.41) with $i = \{g, r, gr\}$:

$$M_i(\tau) = \frac{1}{V_{eff}} \left(\frac{1}{1 + \frac{4D_i \tau}{\omega_0^2}} \cdot \frac{1}{\sqrt{1 + \frac{4D_i \tau}{z_0^2}}} \right). \quad (2.57)$$

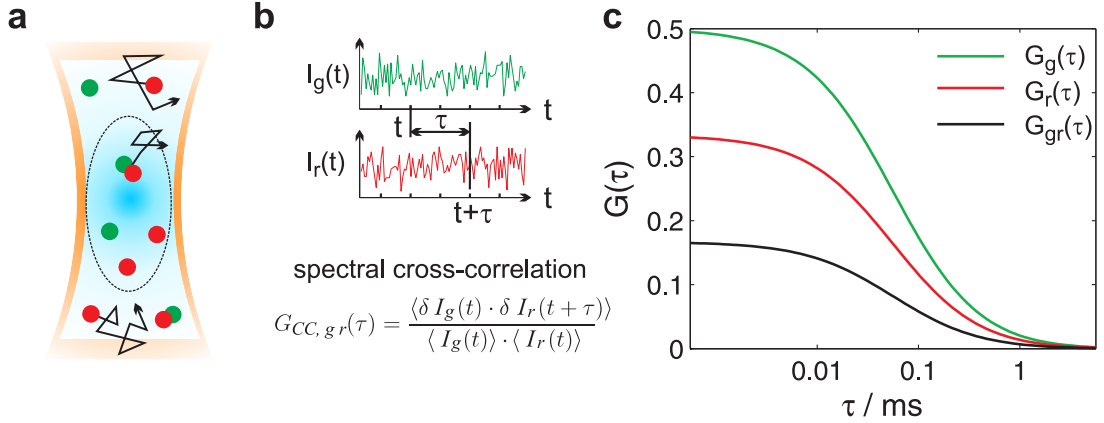


Figure 2.7.: Spectral cross-correlation. **a:** Schematic drawing of two overlapping focal detection volumes. They are created by two excitation lasers of different wavelength, which can excite a green and red fluorophore species, respectively. **b:** Fluorescence intensity fluctuations in both spectral detection channels are measured and cross-correlated over time, resulting in a positive cross-correlation if both species are bound together and diffuse as an entity. **c:** Two autocorrelation curves and two (equal) cross-correlation curves are obtained. The ratio of the cross-correlation amplitude to the lower (here the red) autocorrelation amplitude yields the concentration fraction of double-labeled particles to all green particles, and vice versa. In this example, in total two green molecules ($G_g(0) = 0.5$), three red molecules ($G_r(0) = 0.33$) and one double-labeled molecule is present in the detection volume. The amplitude of the cross-correlation is $G_{gr}(0) = 0.166$, according to equation 2.61. The degree of binding is 50%, relative to all green particles.

Besides the two autocorrelations, we can calculate two cross-correlation functions between both intensity signals from the two detection channels (fig. 2.7). The normalized cross-correlation function is defined as:

$$G_{ij}(\tau) = \frac{\langle \delta I_i(t) \cdot \delta I_j(t + \tau) \rangle}{\langle I_i(t) \rangle \cdot \langle I_j(t) \rangle}. \quad (2.58)$$

Substituting equations 2.53 and 2.54, we obtain two identical cross-correlations functions:

$$G_{gr}(\tau) = \frac{\langle C_{gr} \rangle \cdot M_{gr}(\tau)}{(\langle C_g \rangle + \langle C_{gr} \rangle) \cdot (\langle C_r \rangle + \langle C_{gr} \rangle)} = G_{rg}(\tau). \quad (2.59)$$

The expression is similar to the autocorrelation functions (equations 2.55 and 2.56). However, in the calculation of the sums (equation 2.37), only the correlation term $\langle \delta C_{gr}(\vec{r}, t) \delta C_{gr}(\vec{r}', t + \tau) \rangle$ is non-zero in the numerator, and all concentrations contribute linearly in the denominator.

To quantify the interaction of the two species, only the amplitudes of the auto- and cross-correlation curves are important. They follow by setting $\tau = 0$ in the motion terms (and omitting the angle brackets):

$$G_g(0) = \frac{1}{V_{eff} (C_g + C_{gr})}, \quad G_r(0) = \frac{1}{V_{eff} (C_r + C_{gr})}, \quad (2.60)$$

$$G_{gr}(0) = \frac{C_{gr}}{V_{eff} (C_g + C_{gr})(C_r + C_{gr})} = \frac{N_{gr}}{(N_g + N_{gr})(N_r + N_{gr})}. \quad (2.61)$$

Note that the inverse amplitudes of the autocorrelation functions (equations 2.60) are the total number of all green or all red particles, respectively. The inverse of the cross-correlation amplitude, however,

2. Fluorescence Correlation Spectroscopy (FCS)

is not the number of double-labeled particles (although it indeed has this dimension). Rather, the cross-correlation amplitude is directly proportional to the relative number of double-labeled particles, where relative means with respect to the product of the total number of green and total number of red particles. The measure of interest is hence not the cross-correlation amplitude itself, but the cross-correlation amplitude divided by one or the other autocorrelation amplitude:

$$\frac{G_{gr}(0)}{G_g(0)} = \frac{C_{gr}}{C_r + C_{gr}}, \quad \frac{G_{gr}(0)}{G_r(0)} = \frac{C_{gr}}{C_g + C_{gr}}. \quad (2.62)$$

These quotients give the concentration fractions in the range $[0, 1]$ of double-labeled particles, with respect to the total concentration of all red particles, or all green particles, respectively. In the general case, the concentrations of single labeled green particles and red particles will not be the same, therefore the fractions are different. The single labeled species in excess (for example the red one) will have a lower autocorrelation amplitude.

The degree of binding is now the quotient of the cross-correlation amplitude and this lower red autocorrelation amplitude (here the right term of equation 2.62), which is the concentration fraction of double-labeled particles to all green particles. This crosswise relation is understandable since the less abundant species (here the green one) determines the degree of binding (fig. 2.7). If there are, for example, no single labeled green particles at all ($C_g = 0$) then the binding is 100%, since all green particles are bound to red ones. But vice versa, not all red particles are bound to green ones due to their excess.

From the formulas above, spectral cross-correlation seems to be conceptional simple. Only amplitudes are compared rather than extracting information from precisely analyzing the temporal decay of autocorrelation curves. However, in practice, two-color cross-correlation measurements can contain a number of artefacts. Reasons are for example complex binding stoichiometries, non-ideal overlap of the detection volumes, or spectral cross-talk (31, 37–39).

2.4.2. Spatial cross-correlation

Spatial cross-correlation, also called two-beam, dual-focus or two-focus cross-correlation, is a direction-sensitive extension to the standard one-focus FCS autocorrelation. It was introduced to measure the flow velocity and flow angle in a microstructured channel (40). Recently, it has attained a general attention, not limited to flow systems, because of its inherent capability to yield more reliable and precise estimates of all parameters determined in FCS (15). The enhanced precision is due to the creation of a second detection volume, which is positioned in a well defined distance from the first one and thereby inserts an external ruler in the system. Two autocorrelations can be evaluated from both intensity fluctuations $\delta I_1(t)$ and $\delta I_2(t)$, and two spatial cross-correlations (fig. 2.8), defined in the same way as the spectral cross-correlations above (equation 2.58):

$$G_{12}(\tau) = \frac{\langle \delta I_1(t) \cdot \delta I_2(t + \tau) \rangle}{\langle I_1(t) \rangle \cdot \langle I_2(t) \rangle}, \quad G_{21}(\tau) = \frac{\langle \delta I_2(t) \cdot \delta I_1(t + \tau) \rangle}{\langle I_1(t) \rangle \cdot \langle I_2(t) \rangle}. \quad (2.63)$$

The cross-correlations give a measure for the probability that a molecule, which has been detected in one focal volume at time t , is subsequently detected in the other at time $t + \tau$. These two cross-correlations will be the same, if there is no directionality in the system as it is for random diffusion. In case of a flow or active transport in the system, the so-called forward cross-correlation in flow direction will have a higher amplitude than the backward cross-correlation (fig. 2.8 c). The difference of the two cross-correlation curves depends on the angle between the flow velocity vector and the distance

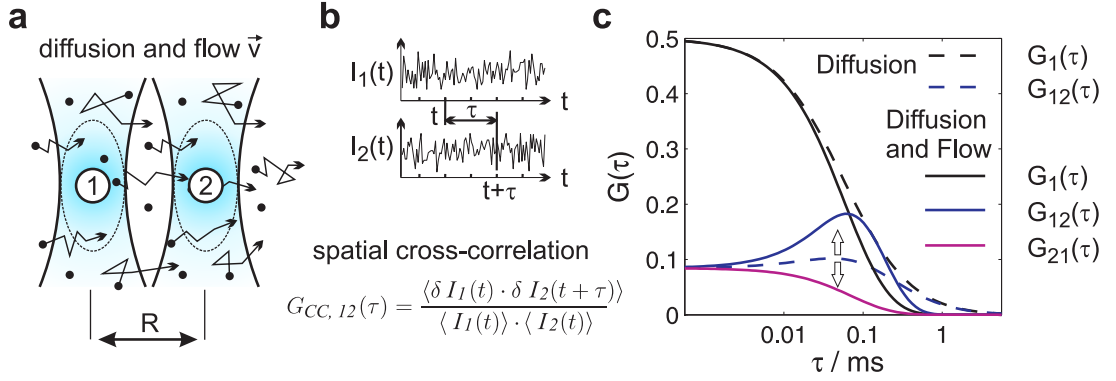


Figure 2.8.: Spatial cross-correlation. **a:** Schematic drawing of two spatially offset focal detection volumes and fluorophores moving by diffusion and by flow in the direction from volume 1 to 2. **b:** Fluorescence intensity fluctuations from both spatial detection channels are cross-correlated over time, resulting in a positive cross-correlation if a molecule is first detected in one focal volume and subsequently in the other. **c:** Two equal autocorrelation curves $G_1(\tau) = G_2(\tau)$ and two cross-correlation curves $G_{12}(\tau)$ and $G_{21}(\tau)$ are obtained. In case of diffusion, both cross-correlations are the same. In case of a directional movement, the forward cross-correlation $G_{12}(\tau)$ in flow direction has a higher amplitude than the backward cross-correlation ($D = 400 \mu\text{m}^2/\text{s}$, $v = 3 \text{ mm/s}$, $\omega_0 = 0.3 \mu\text{m}$ and $R = 0.4 \mu\text{m}$).

vector of the two focal volumes. Maximum difference is obtained at zero degree, when positioning the two foci in flow direction. The difference decreases for increasing angles until it disappears at 90° . Spatial cross-correlation is hence direction-sensitive, as opposed to autocorrelation, which only depends on the magnitude of the flow.

The model cross-correlation function for the general case of combined diffusion and flow can be calculated using the concentration correlation function $\phi(\vec{r}, \vec{r}', \tau)$ (equation 2.49) and the two molecule detection functions $W_1(\vec{r})$ and $W_2(\vec{r})$ of the foci, where the second focal volume is spatially offset by \vec{R} with respect to the first one:

$$G_{12}(\tau) = \frac{\int \int W_1(\vec{r}) W_2(\vec{r}' - \vec{R}) \phi(\vec{r}, \vec{r}', \tau) dV dV'}{\langle C \rangle^2 \int W_1(\vec{r}) dV \cdot \int W_2(\vec{r}' - \vec{R}) dV'}. \quad (2.64)$$

If both detection volumes are approximated by the simple three-dimensional Gaussian (equation 2.8 in section 2.2), and if the distance vector \vec{R} and flow vector \vec{v} are assumed to be in the confocal x-y-plane with an angle α in between, then the cross-correlation reads:

$$G_{12}(\tau) = \frac{1}{N} \left(\frac{1}{1 + \frac{4D\tau}{\omega_0^2}} \cdot \frac{1}{\sqrt{1 + \frac{4D\tau}{S^2\omega_0^2}}} \right) \cdot \exp\left(-\frac{v^2\tau^2 + R^2 - 2Rv\cos\alpha}{\omega_0^2 + 4D\tau}\right). \quad (2.65)$$

The other cross-correlation $G_{21}(\tau)$ is obtained for $\tilde{\alpha} = \alpha + \pi$. In case of a known flow direction, for example in a microfluidic channel, the detection volumes are positioned parallel to the flow direction to obtain the largest separation of both cross-correlation curves ($\alpha = 0$ and $\tilde{\alpha} = \pi$) and hence the highest sensitivity with respect to the detection of small flow speeds. For $R = 0$, we obtain the autocorrelation function (equation 2.50).

2. Fluorescence Correlation Spectroscopy (FCS)

Diffusion and 3D-Gaussian detection volume

If we set $v = 0$ in equation 2.65, we get the two identical spatial cross-correlation functions in case of pure diffusion and the usual three-dimensional Gaussian description of the two detection volumes:

$$G_{12}(\tau) = G_{21}(\tau) = \frac{1}{N} \left(\frac{1}{1 + \frac{4D\tau}{\omega_0^2}} \cdot \frac{1}{\sqrt{1 + \frac{4D\tau}{S^2\omega_0^2}}} \right) \cdot \exp\left(\frac{-R^2}{\omega_0^2 + 4D\tau}\right). \quad (2.66)$$

The function is the autocorrelation function for diffusion (equation 2.28), multiplied with an exponential factor. Due to this factor, the cross-correlation is always lower than the autocorrelation. For a not too small separation of the two focal volumes (ratio $R/\omega_0 \gtrsim 1$), the cross-correlation exhibits a characteristic maximum (fig. 2.8 c) at a lag time τ that corresponds to the time it takes a molecule to diffuse from one to the other detection volume. It is also this exponential factor, which leads to the separation of the two parameters focus waist ω_0 and diffusion coefficient D , so that these and the other physical parameters concentration C and structure parameter S can be directly determined from a fit, provided that the distance R is known. Therefore, the need for a calibration of the detection volume in FCS with a reference dye is omitted. Moreover, possible variations of the fit parameter ω_0 itself can be investigated and attributed to potential artefacts.

However, the distance R needs to be determined once with high precision since the result of D depends quadratically on R . The distance determination is not a straight forward task for two diffraction-limited and overlapping focal volumes, and hence several methods have been proposed and successfully been demonstrated, for example point spread function scans with beads, two-focus FCS reference measurements on membranes (15), and a combined approach of dynamic light scattering measurements and two-focus FCS on small latex beads (41). In our two-focus EMCCD-camera based setup, we directly determine the distance from the acquired spatially resolved images with high precision (chapter 8).

Diffusion and generalized Gaussian-Lorentzian detection volume

When Dertinger *et al.* (15) introduced two-focus FCS as a method to obtain absolute and accurate diffusion coefficients, they also used a new two-parameter model describing the molecule detection function to evaluate two-focus cross-correlation data. This model assumes a generalized Gauss-Lorentz excitation profile to account for the laser divergence and a simple pinhole function:

$$W(x, y, z) = \frac{\kappa(z)}{w^2(z)} \exp\left(-\frac{2}{w^2(z)}(x^2 + y^2)\right). \quad (2.67)$$

In each z -plane, this is a Gaussian distribution of width $w(z)$:

$$w(z) = w_0 \left(1 + \left(\frac{\lambda_{\text{ex}} z}{\pi w_0^2 n} \right)^2 \right)^{1/2}, \quad (2.68)$$

where λ_{ex} is the excitation wavelength and n is the refractive index of the immersion medium. Equation 2.67 is not the usual Gauss-Lorentz profile due to the non-trivial amplitude function $\kappa(z)$:

$$\kappa(z) = 1 - \exp\left(-\frac{2a^2}{R^2(z)}\right), \quad (2.69)$$

2.4. FCS cross-correlation analysis

which accounts for the axial detection profile, defined by the confocal aperture of radius a in the object space and the point spread function dependence $R(z)$:

$$R(z) = R_0 \left(1 + \left(\frac{\lambda_{\text{em}} z}{\pi R_0^2 n} \right)^2 \right)^{1/2}, \quad (2.70)$$

where λ_{em} is the center emission wavelength. The parameters w_0 and R_0 are two unknown model parameters, where R_0 replaces the structure parameter S of the 3D-Gaussian model.

The spatial cross-correlation $G_{12}(\tau)$ for two focal volumes with distance d , assumed along the x -direction, can be calculated using the concentration correlation function $\phi(\vec{r}, \vec{r}', \tau)$ (equation 2.23) and the molecule detection function $W(x, y, z)$ (equation 2.67):

$$G_{12}(\tau) = \frac{\int \int W(x, y, z) W(x' - d, y', z') \phi(\vec{r}, \vec{r}', \tau) dV dV'}{(\langle C \rangle \int W(x, y, z) dV)^2} = \frac{g_{12}(\tau)}{\langle F(t) \rangle^2}. \quad (2.71)$$

For clarity, we separately give the non-normalized cross-correlation $g_{12}(\tau)$ and the normalization. The non-normalized cross-correlation reads:

$$g_{12}(\tau) = \frac{C}{4} \sqrt{\frac{\pi}{D\tau}} \int_{-\infty}^{\infty} dz \int_{-\infty}^{\infty} dz' \frac{\kappa(z) \kappa(z')}{w^2(z) + w^2(z') + 8D\tau} \times \exp\left(-\frac{(z - z')^2}{4D\tau} - \frac{2d^2}{w^2(z) + w^2(z') + 8D\tau}\right). \quad (2.72)$$

This function can only be evaluated numerically, and for convenience, the variables are transformed to:

$$\xi = \frac{z' - z}{2\sqrt{D\tau}} \quad \text{and} \quad \eta = \frac{z' + z}{2}, \quad (2.73)$$

which results in:

$$g_{12}(\tau) = 2C \sqrt{\pi} \int_0^{\infty} d\xi \int_0^{\infty} d\eta \frac{\kappa(\eta - \xi\sqrt{D\tau}) \kappa(\eta + \xi\sqrt{D\tau})}{w^2(\eta - \xi\sqrt{D\tau}) + w^2(\eta + \xi\sqrt{D\tau}) + 8D\tau} \times \exp\left(-\xi^2 - \frac{2d^2}{w^2(\eta - \xi\sqrt{D\tau}) + w^2(\eta + \xi\sqrt{D\tau}) + 8D\tau}\right). \quad (2.74)$$

The infinite integrals can be evaluated on a finite two-dimensional strip due to the rapidly decaying functions w and κ , so that the result does not change any more when increasing the truncation value (15). The normalization in equation 2.71 is given by:

$$\langle F(t) \rangle^2 = \left(C \frac{\pi}{2} \int_{-\infty}^{\infty} \kappa(z) dz \right)^2 \quad (2.75)$$

In (15), non-normalized experimental cross-correlation and auto-correlation curves ($d = 0$) were directly fit to the non-normalized model function (equation 2.74) and two factors ε_1 and ε_2 were introduced to account for small differences in the overall excitation power and detection efficiency of the two detection volumes.

2. Fluorescence Correlation Spectroscopy (FCS)

In this thesis, normalized two-focus cross-correlation and autocorrelation curves were globally fit with a Matlab based fit routine (31). For diffusion measurements in solution (chapter 10), data was fit numerically to the generalized Gauss-Lorentz model. However, using the 3D-Gauss model (equation 2.66) resulted only in small differences of the fit parameters. This is most likely due to the small divergence of our only moderately focused laser beams and the comparable tight axial confinement of the foci by small, individual pixel-based pinholes.

Alternating excitation avoids spatial cross-talk

All expressions for spatial cross-correlations above imply that both detection volumes are described by two independent, laterally symmetric molecule detection functions. For continuous excitation of both foci, this assumption is still justified in case of laterally well separated excitation volumes (ratio of distance to focus waist $R/\omega_0 \gg 1$ in equation 2.65), as have been employed in flow measurements (40, 42). There, the cross-correlation curve reflects the probability, that a molecule was first excited and detected in volume one at time t and at a later time $t + \tau$ it was excited and detected in volume two. A substantial flow, which dominates over diffusion, leads to a peak in the cross-correlation for the characteristic time it takes a molecule to flow from the center of volume one to the center of volume two.

If two-focus FCS is used to investigate pure diffusion or small flows with superimposed dominating diffusion, the two foci need to be in close proximity ($R/\omega_0 \approx 1$) to obtain a measurable cross-correlation. This is understandable since diffusion is isotropic and hence only a small fraction of molecules, that was detected in volume one, appears in the second detection volume. For large distances, the probability and therefore the cross-correlation goes quickly to zero. The cross-correlation is again the probability, that a molecule was first excited and detected in volume one and then excited

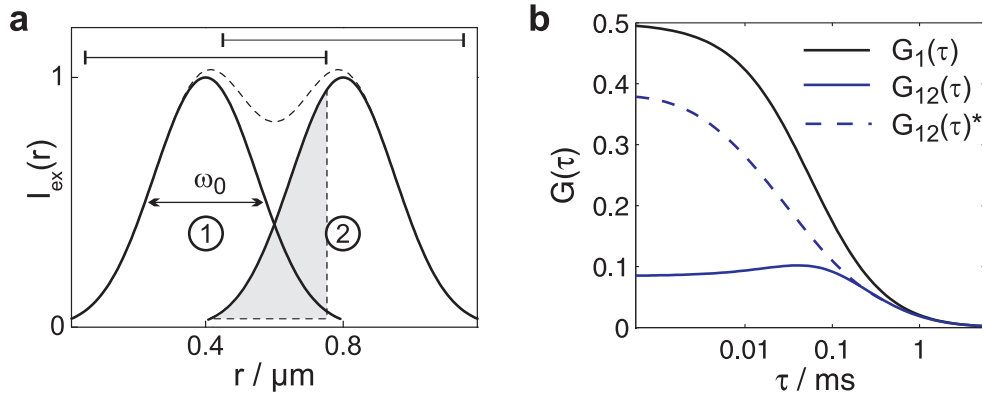


Figure 2.9.: Spatial crosstalk. a: Lateral excitation profiles (equation 2.4 at $z = 0$) of two overlapping focal volumes as the ones in fig. 2.8 a ($\omega_0 = 0.3 \mu\text{m}$ and distance $R = 0.4 \mu\text{m}$). The ranges above the profiles indicate the collection ranges of the confocal pinholes of typical size (diameter $0.75 \mu\text{m}$ in sample space). In case of simultaneous excitation of both foci, the shaded area is the spatial cross-talk of the excited focal volume number two into the detection channel number one. The cross-talk deforms the radially symmetric detection volume (dashed line). **b:** Auto- and cross-correlation curves in case of diffusion (fig. 2.8 c). In case of spatial cross-talk, the amplitude of the cross-correlation $G_{12}(\tau)^*$ is artificially higher, distorting the usable information from two-focus FCS. However, spatial cross-talk can be completely circumvented by employing alternating excitation and detection, so that the true spatial cross-correlation curve $G_{12}(\tau)$ is obtained.

and detected in volume two. The overlap of the two detection volumes is taken into account by the models as can be seen by the non-zero cross-correlation for the shortest lag times (fig. 2.8 c). This is due to molecules that were present in the overlap region of both volumes and hence their correlation time was shorter than the average time it took a molecule to diffuse from the center of volume one to the center of volume two. Still, it is the characteristic peak in the cross-correlation, or more general the ratio of the amplitude of the cross-correlation to the amplitude of the autocorrelation, which yields the information in two-focus FCS in case of pure diffusion.

In case of overlapping detection volumes, it directly follows from the discussion above, that the two detection volumes have to be employed in an alternating fashion. This means, lasers foci are excited alternatingly and fluorescence signal is only evaluated from the respective detection channel. If both foci are excited continuously, the photons originating from the excited focal volume one but are detected in the detector belonging to volume two (and vice versa), are called spatial cross-talk. They largely deform the assumed radially symmetric detection volumes in the models above (fig. 2.9). The resulting focal volumes are larger, and their effective distance is smaller. Therefore, the cross-correlation amplitude will be artificially higher, which is called a pseudo-autocorrelation (40). This effect cannot be easily included in the theory. For measurements in flow systems, typically the pseudo-autocorrelation was removed from the data by subtracting the backward from the forward cross-correlation (40). In diffusion systems, however, this would result in a zero line. Alternating excitation and detection is hence an easy way to completely avoid spatial cross-talk. Overlapping focal volumes are thereby accurately described by the standard models.

The alternating excitation, also called pulsed interleaved excitation (43, 44), can be performed with pulsed lasers (15), or by using continuous wave lasers and acousto-optical modulators (in this theses, chapter 8), electro-optical modulators (45, 46) or by repeated confocal scans (47).

3. Detection methods in FCS

The breakthrough of fluorescence correlation spectroscopy was achieved when its sensitivity reached the single-molecule level by using confocal setups and single-photon counting detectors (1). This method of measuring the dynamic properties of single molecules by auto-correlation analysis was then widely used for studying different modes of diffusion (48, 49), flow (50), chemical reactions (51), photophysical properties (26, 27) and receptor ligand interactions (52).

As an important next step of technical advance, two focal volumes were utilized and the cross-correlation of both fluorescence signals was evaluated. The two prominent variants are spectral cross-correlation (36) and spatial cross-correlation (40). The theory of cross-correlation was introduced in section 2.4. In this chapter, we describe the current standard and novel detection methods used in these two FCS extensions.

To allow for multiplexed autocorrelation analysis in a sample, and to gain more flexibility in both spectral and spatial cross-correlation, we introduce the idea of utilizing an electron multiplying CCD-camera (EMCCD) for detection in FCS. We describe the EMCCD technology and compare the sensitivity and speed of this new detector to the currently used standard point detector, the avalanche photodiode (APD).

3.1. Multi-color detection and spectral cross-correlation

Dual-color FCS cross-correlation allows for measuring the interaction between two differently labeled molecular species. It permits to measure the changes in concentration and diffusion characteristics of product and educts, all at the same time. In the first dual-color cross-correlation FCS (FCCS) experiment, the binding of two complementary DNA single strands labeled with Rhodamin green and Cy-5, respectively, was followed (36).

The two-color detection setup principle, used at that time, is still the typically employed one (fig. 3.1). Two excitation lasers are employed to excite the two molecular species efficiently. Fluorescence light is split by a dichroic mirror in the detection path and projected onto two standard APDs. Most critical for spectral cross-correlation is the good objective lens. It needs to be free of chromatic aberrations in order to obtain a good spatial overlap of both lasers, noticeable by a high cross-correlation amplitude when measuring a positive control sample with only double-labeled species.

Dual-color FCS has been used for *in vitro* and *in vivo* studies. *In vitro*, enzyme kinetics were followed (53), protein-DNA interaction and site-specific DNA recombination could be investigated (54), and partitioning of water-insoluble proteins into artificial model membranes was demonstrated (55).

In live cells, cross-correlation was utilized to follow the endocytic pathway of cholera toxin, showing the separation of two of its subunits at the Golgi body (56). FCCS was further employed to investigate the dynamics and binding affinities among components of the MAP kinase in living yeast cells (57), and FCCS allowed for real-time *in vivo* monitoring of the incorporation of small double-stranded RNA molecules into the RNA-induced silencing complex (58). In living zebrafish embryos, FCCS could quantify *in-vivo* binding affinities (59).

3.1. Multi-color detection and spectral cross-correlation

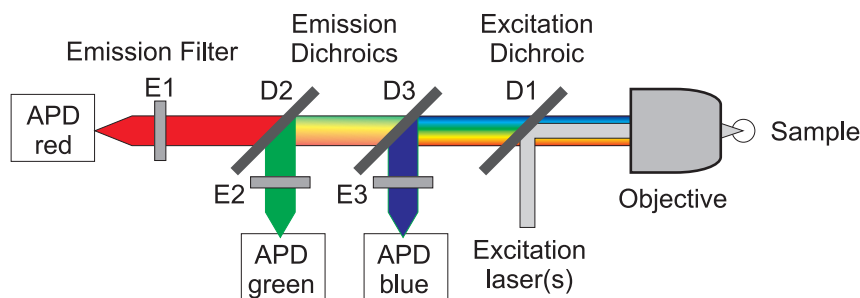


Figure 3.1.: Spectral cross-correlation setup with up to three detection channels. Extension of the confocal setup for autocorrelation FCS (fig. 2.2) to detect up to three fluorescent species for cross-correlation analysis (confocal pinholes are not shown). In case of two colors, an emission dichroic mirror D2 and filter E2 is inserted, reflecting the green fluorescence light to a second APD. In case of three colors, D3, E3 and a third APD are utilized. The multi-color excitation is done with perfectly overlapped excitation lasers of different wavelengths, or with single-wavelength excitation for special dyes.

A challenge of the initially used home-built two-color setups was stability. A perfect alignment of the two laser foci could be a demanding and time-consuming task, which had to be performed before each measurement series. The last generations of commercial FCS setups have solved this problem, so that maximum spectral cross-correlation is very stable and sufficiently high (60-80%). The difference to 100% is due to still non-perfect cross-correlation test samples, and due to the remaining small overlap mismatch of the two diffraction-limited focal volumes.

Alignment issues could be completely circumvented by utilizing a single laser line for excitation of spectrally differently emitting fluorophores. This was performed by either two-photon excitation (39), or by another approach called single-wavelength FCCS (60, 61), where a single visible laser line for efficient excitation of spectrally differently emitting fluorophores was employed. Depending on the sample and especially the fluorophores involved, either excitation technique of these three (one-photon excitation with one, or with two lasers, or two-photon excitation) can be advantageous (62).

Irrespective of the excitation method, the detection part of the FCS-setups were developed further for multi-color detection. Dual-color FCS was extended to three detection channels (fig. 3.1) to investigate ternary systems, by triple pairwise cross correlation (63) and by triple-color coincidence analysis (64). The detection setup used, was the simple extension of the dual-color setup, only supplemented by another dichroic mirror and a third APD.

For more than three color detection, these systems utilizing dichroic mirror and filters could not be extended further, because of the inherent multiplicative signal losses induced by the filter cascade. Therefore, two groups introduced a direct spectral separation of the fluorescence emission light for FCS (fig. 3.2). One setup was established with a diffraction grating and a fix optical linear fiber array (65) and the other setup utilized a dispersion prism and a fiber array as well. Advantages of the latter implementation was that individual fibers could be aligned independently and detection efficiency was by factor two higher (66) compared to the grating-based setup.

Full spectral detection for FCS

If we first look at confocal imaging, spectral detection of fluorescence light has been performed in various different arrangements (67, 68). Spectral imaging can be utilized to distinguish fluorophores

3. Detection methods in FCS

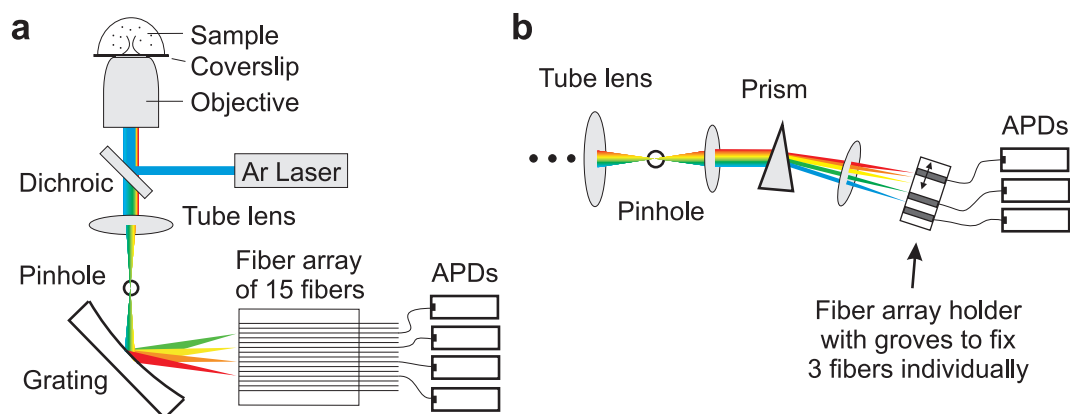


Figure 3.2.: Spectral detection for FCS with optical fiber arrays and APDs. Optical setups for multi-color FCS, used in two references: **a:** A concave diffraction grating and an array of 15 optical fibers was utilized (65). **b:** A dispersing prism and three optical fibers were used (66). Fibers could be positioned freely in the spectrum. (figure adapted from (66)).

with highly overlapping emission spectra (69, 70) or the fluorophores from autofluorescence background (71) by linear spectral unmixing. Spectrographs have been built as separate devices which were coupled to the output port of a microscope with an optical fiber (72), and even spectra of single molecules were acquired (73). A multi-spot spectral imaging system was realized with a spinning disk setup (74).

The technical realization with high efficiency and tunable detection ranges has also been implemented in commercially available confocal laser scanning microscopes from various companies in the last years. Some systems use diffraction gratings, others prism-based dispersion. Some employ linear detector arrays (75), and others define up to five detection channels by decomposing the spectrum with moveable optomechanics (76).

For FCS, however, only few attempts have been done to realize full spectral detection. Next to the spectral FCS platforms (65, 66), mentioned above, which were designed to be also extendable to more than three or four detection channels, only one full spectrally-resolved FCS setup has been reported (77). It utilized a multianode PMT, dedicated multichannel single-photon counting electronics and global FCS analysis. However, photon detection efficiency was only 3-5% due to the descanning optics, the grating efficiency and the low sensitivity of the multianode PMT. Therefore, measurements of dye molecules were difficult, and mainly the dynamics and concentrations of polystyrene fluorescent spheres (≈ 150 times brighter than single fluorophores) were analyzed.

A technological solution for spectral FCS seems to be more demanding than for spectral imaging. The reasons are the very specific detector requirements. Indeed, at present, FCS is mostly performed with a single type of detector, which is the avalanche photodiode (APD). For the establishment of spectral FCS, the following points have to be considered:

1. First, only a couple of detection channels, for example according to the number of fluorescent species to be investigated, could be freely defined by cutting out the respective ranges in the dispersed spectrum with appropriate opto-mechanical components, as has been done in spectral imaging (76). The light from these individual detection channels could then be detected with a standard single point APD. However, the active area of an APD is comparably small (diameter $< 200 \mu\text{m}$). The collimated fluorescence light beam, first projected onto the confocal pinhole

3.1. Multi-color detection and spectral cross-correlation

(diameters 30 – 200 μm), and usually not dispersed, can be easily mapped onto this small APD area. However, if the spectrum is dispersed with a sufficient spectral resolution, the spatial length of the spectrum in each detection channel will be a multiple of the pinhole size; and such a spatially extended spectrum can not easily be mapped onto a small single APD, unless more advanced setups with additional prisms are designed.

2. Second, emission light could be directly dispersed onto a detector array (a detector array is also required for multiplexed FCS, further discussed in section 3.2). FCS requires a detector with high quantum efficiency, high time resolution, low dark signal and low afterpulsing probability. Only recently, multi-pixel avalanche diode arrays, suitable for FCS, have been developed (78, 79). The monolithic array in (79), consisting of eight detector elements for parallel photon counting, was reported to be produced at low costs. However, currently, the price for a single APD is $>\$5000$, and it has not changed over the last years. Therefore, it can be anticipated that multiplexed APDs arrays, including the necessary signal processing electronics, will still be cost-intensive in the near future.
3. APDs are operated in photon counting mode. The electron avalanche, triggered by the first detected photon, results in many photons being emitted again by the detector. In an APD-array, this light can result in optical cross-talk between individual detecting cells (80).
4. The photon counting technology requires a structure of the individual active cell, so that neighboring cells need to be separated by more than the diameter of the active area (80). The reported eight-element array in (79), for example, had an active area diameter of 50 μm and a pitch of 250 μm . In a continuous spectrum, which is dispersed onto the array detector, the low fill factor will result in spectral detection gaps. This can lead to a significantly lower detection efficiency, unless solutions such as microlens arrays are employed (81).

Detection with an EMCCD camera is an alternative approach. High quantum efficiency, 100% fill factor, no optical cross-talk, and moderate price are advantages, and only the limited time resolution is a disadvantage (section 3.3). The conceptual sketch of a dispersion by a prism and subsequent mapping onto a line of the EMCCD is shown in fig. 3.3.

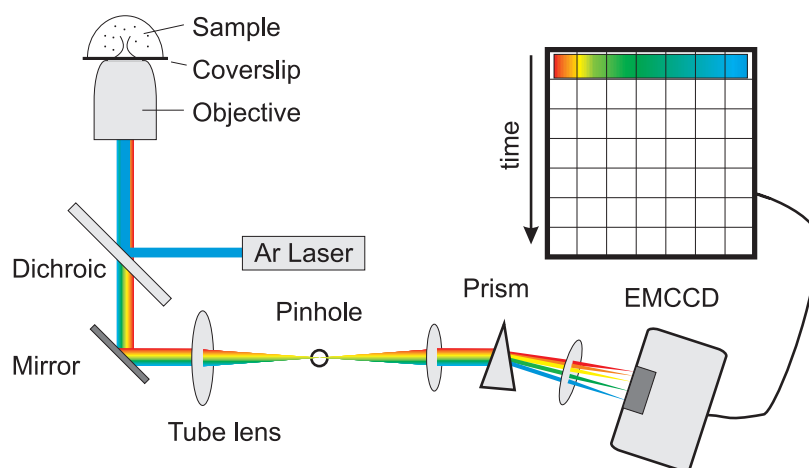


Figure 3.3.: Idea of full spectral detection with an EMCCD. Sketch of using the EMCCD as a spectral detector for FCS. The dispersion by a prism is similar to the one used in (66) (fig. 3.2 b). However, detection with an EMCCD is more flexible, allowing for freely tunable detection ranges.

3. Detection methods in FCS

The EMCCD would be operated in the same acquisition mode that will be introduced in chapter 5 for single spot EMCCD-FCS. The dispersed spectrum is mapped onto one or several CCD rows. The light level per pixel, however, will be much lower, depending on the intended spectral resolution. At low light levels, dark count sources like clock-induced-charges (section 7.2) might become an important limitation.

In the scope of this thesis, we focused on the development of EMCCD-based detection for FCS, being, first of all, a spatially resolved detection. To use the spatial detector for spectrally resolved FCS, will then be a next step, which we did not approach yet. Such an implementation will yield a highly efficient, tunable, spectrally resolved detector for spectral cross-correlation.

3.2. Parallel detection and spatial cross-correlation

When fluorescence correlation spectroscopy (FCS) was combined with confocal setups (1), the diffraction limited observation volume permitted to selectively probe a small ensemble of molecules. Measurements could be performed at specific positions in the sample, for example in the cytoplasm or in the nucleus of a living cell (58).

However, confocal FCS has therefore traditionally been a single-point technique, meaning that fluorescence signal was collected from one focus position in the sample only. Repeated measurements at different positions in the sample were performed successively, which could result in long total measurements times, required for obtaining a good statistics.

Naturally, there was a need to extend single-spot FCS to multiplexed FCS. To this end, parallel multi-spot excitation and detection strategies had to be developed. Interestingly, the first two-beam

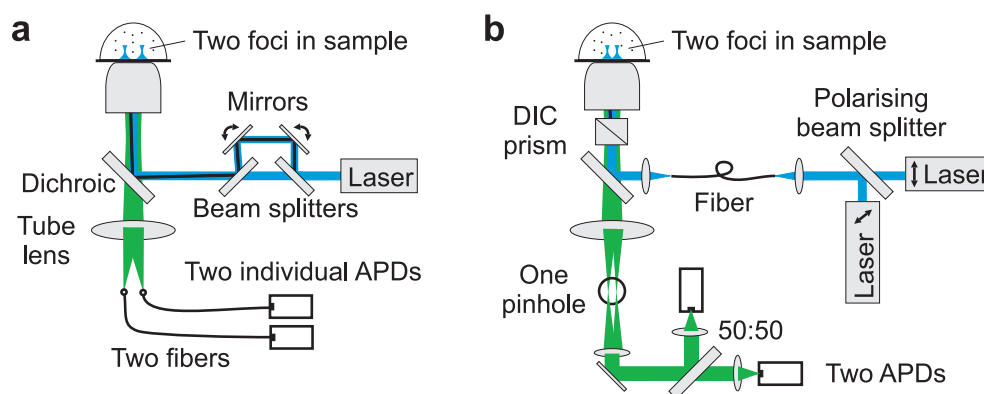


Figure 3.4.: Two-beam spatial cross-correlation setups. Optical setups for two-focus FCS. **a:** When the method was introduced, the laser beam was split and reunited by beam splitters and coupled into the objective at a slightly different angle. Fluorescence signal from the two laser foci was detected with two optical fibers, coupled to individual avalanche photodiodes (APDs), for determination of molecular flow (40). **b:** At present, two-focus FCS is often used to measure calibration free, precise diffusion coefficients (15, 47). When this application was introduced (15), two pulsed-interleaved lasers of different polarisation were coupled into a polarisation maintaining fiber, and were collimated after the fiber and separated by a Nomarski prism, typically used for differential interference contrast (DIC) microscopy. In this configuration, distance of both focal volumes is small, so that fluorescence from the overlapping detection volumes passes through a single large pinhole. The photons are sorted between both foci by their arrival times, with respect to the laser pulses. The detection with two APDs is not related to the two foci, but solely to prevent the APD afterpulsing artefact (section 2.3.4).

3.2. Parallel detection and spatial cross-correlation

setup (fig. 3.4 a) was not developed for the sake of a parallel measurement. Rather, spatial cross-correlation of the signal from the two detection volumes was performed as a direction-sensitive extension to the standard one-focus FCS autocorrelation (section 2.4.2). The mathematical description of the spatial cross-correlation was formulated, and it was utilized to measure the flow velocity and angle of fluorophores in a microstructured channel (40). This method of measuring direction-sensitive was also potentially interesting for the investigation of cellular transport mechanisms (82).

Recently, two-focus FCS was recovered as a method to not only investigate flow properties, but also to obtain calibration-free parameter estimates in FCS (section 2.4.2, fig. 3.4 b). To this end, measurements in pure diffusion systems were performed and precise reference values for the diffusion coefficients of several fluorophores were obtained (15, 47, 83).

The first parallel FCS was done by splitting the excitation laser with a diffractive optical element into 2×2 laser foci, and by using four optical fibers and individual avalanche photodiodes (APD) for detection (84) (fig. 3.5 a). A similar diffractive optical element was utilized to create four spots in a line for measurements in a flow system, again with individual fibers and APDs for detection (85). Very recently, multipoint FCS has been performed with total internal reflection excitation and detection with seven optical fibers and individual photomultiplier tubes (86) (fig. 3.5 b).

The first integrated single-photon sensitive multi-element device for FCS was a 2×2 CMOS (complementary metal oxide semiconductor) detector array (87) (fig. 3.5 c). Despite its much lower detection efficiency of 7%, compared to 60% of an APD, reliable FCS curves could be achieved. Recently, a monolithic matrix detector array of 6×8 individual APD detectors was developed (78) (fig. 3.5 c). It exhibits a high detection efficiency of 48% peak at 530 nm, but array elements have a rather large pitch of $240 \mu\text{m}$ and small active area of each element of $50 \mu\text{m}$ diameter, as mentioned before in section 3.1 for the 8×1 array (79).

Classical two-focus FCS measurements were performed, for example, to study the flow in microchannels with two-photon excitation (88), and to resolve the bound and unbound fractions of

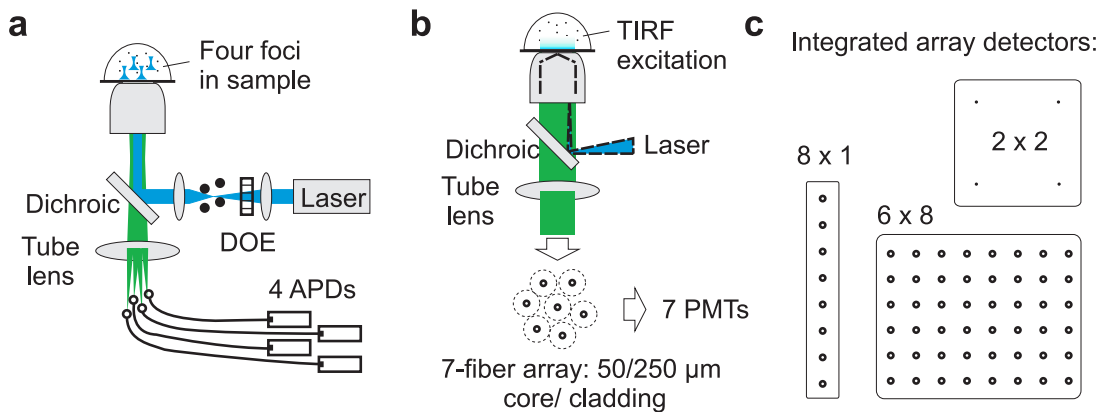


Figure 3.5.: Parallel detection methods for FCS. **a:** Schematic drawing of the first parallel FCS setup, performed by utilizing a diffractive optical element (DOE) to produce four identical laser foci. Fluorescence was detected with four optical fibers and individual APDs (84, 85). **b:** Recently, seven spot multi-point FCS has been realized by TIRF illumination and seven optical fibers with individual PMTs (86) for detection. **c:** Schematic sketch of integrated multi-element detector arrays: initially, a 2×2 array (87) was used, but recently, an 8×1 (79) and a 6×8 array (78) have been developed. Although very promising, the fill factor is still low (typically $50 \mu\text{m}$ diameter of the active area versus $250 \mu\text{m}$ pitch between elements).

3. Detection methods in FCS

single-stranded DNA in a DNA-protein complex when flowing through an electrophoresis capillary (89). Two-focus FCS was further utilized to quantitatively map the 3-D flow pattern in a microchannel, generated by an electrohydrodynamic micropump (42).

Some novel ideas have been described to simplify the excitation and detection geometries for two-focus FCS, by for example using a single expanded laser focus and two small detection pinholes (90) or by using two encapsulated core and ring pinholes (91). Two-focus FCS with tunable distances between the foci was achieved by means of a Michelson interferometer (92), or by the use of a computer-controlled spatial light modulator (93). With the latter implementation, the two spots were positioned on both sides of a phospholipidic membrane, and spatial cross-correlation was utilized to probe the membrane permeability for hydrophilic or hydrophobic molecules. Furthermore, a versatile dual spot FCS setup has been reported (94), which was utilized for simultaneous imaging and FCS, and for circular two-spot scanning FCS.

Towards a full spatially resolved detection for FCS

Even though the degree of multiplexing has been constantly increasing, spatially fixed excitation and detection schemes lack flexibility and simplicity. If we again compare it to confocal imaging, we notice the same trend as discussed for spectrally resolved detection.

For confocal imaging, multiplexing strategies have been developed much faster and further than for FCS. Parallel excitation is commercially realized, for example, by Nipkow spinning disk (Andor Technology, Belfast, UK), linear multi-beam scanning (Lavision Biotec GmbH, Bielefeld, Germany) or line-scanning strategies (Zeiss GmbH, Jena, Germany). Parallel detection is mostly performed by CCD-cameras, especially since 2001 by highly sensitive electron multiplying CCD (EMCCD) cameras (section 3.3).

For spatially resolved FCS, the limiting factor is hence not the multiplexed confocal excitation but again the lack of a suitable array detector as mentioned above for spectrally resolved FCS. Two-dimensional APD or PMT arrays, that qualify for FCS, are not commercially available. However, since EMCCDs were shown to be single-photon sensitive (95), two groups introduced basically at the same time in 2006 the idea of utilizing an EMCCD for spatially resolved FCS (96, 97) (fig. 3.6 a). Kannan et al. (96) demonstrated EMCCD-FCS measurements on diffusing fluorescent dyes and polystyrene beads in high-viscosity media, and on membrane proteins in living cells. They also presented measurements of flows in microchannels. Flow speeds were deduced from autocorrelation and flow directions were obtained from spatial cross-correlation between different CCD pixels within one focal spot. Time resolution of the FCS curves was 4 ms, using a 20×20 pixels subregion on the EMCCD for data acquisition. In our work (97), as detailed in part II of this thesis, we focused on performing EMCCD-FCS with a high time-resolution, suitable for measuring commonly used fluorescent probes such as fluorescent proteins and organic dyes in aqueous solution. A time resolution of 20 μ s was achieved in a special camera readout mode, when only using several top lines of the CCD chip (section 5.2). We presented a simple two-spot measurement to demonstrate the multiplexing capability of EMCCD-FCS (97).

After these initial EMCCD-FCS demonstrations, several further implementations have been reported. An increased multiplexing was achieved by utilizing a spinning disk confocal microscope (fig. 3.6 b), which allowed the illumination of 10,000 points simultaneously (98). Time resolution for FCS analysis was limited to 100 ms, a speed still sufficient to measure small microspheres (200 nm diameter, brightness equivalence to 100 fluorescein molecules). Recently, multipoint FCS has also been performed with a stopped Nipkow disk, greatly increasing the signal to noise ratio of the FCS

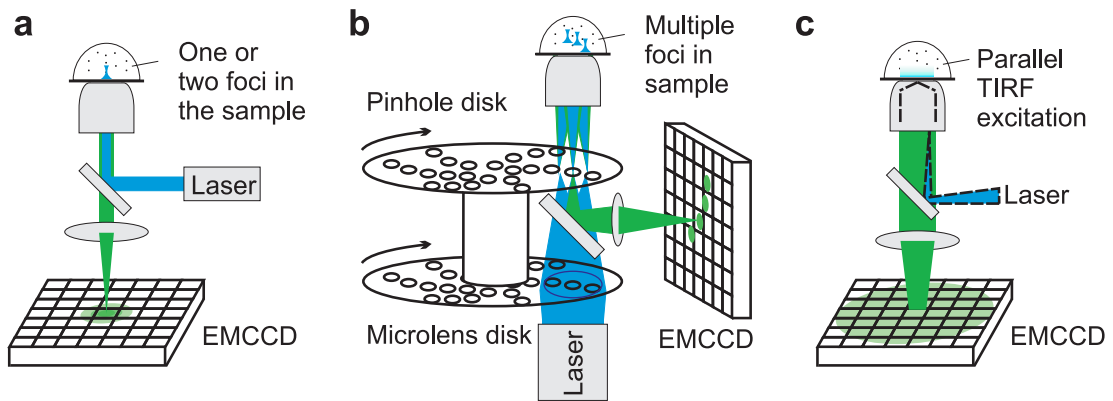


Figure 3.6.: Spatially resolved FCS with EMCCD-based detection. **a:** EMCCD-based FCS was introduced by two groups using setups with one or two confocal detection volumes (96, 97). **b:** Multiplexing was achieved by using a spinning disk setup, either with the disk rotating (98) or also with a stopped disk (99). **c:** EMCCD-FCS with TIRF illumination has been performed for autocorrelation (101) and spatial cross-correlation (102) analysis.

curves by a factor of more than ten (99). Time resolution was 0.3 ms (as we will report in the kinetic camera readout mode, section 5.1) for a small subregion on the CCD, corresponding to 10 pinholes; and 2 ms for full frame acquisition, corresponding to more than 600 pinholes. This allowed to measure 40 nm colloids, a membrane dye and a fluorescent protein complex. Recently, spatially extended FCS was also performed with a much less sensitive CMOS-camera for the quantification of flows of 1 μm silica particles in microchannels (100).

As an alternative to using multiple confocal excitation volumes, multiplexed EMCCD-FCS was also performed with total internal reflection excitation (fig. 3.6 c) for measurements of membrane diffusion in lipid bilayers and membrane proteins in living cells (101). At an EMCCD time resolution of 5 ms, 1600 autocorrelations were acquired simultaneously, and the measurement area was sufficiently large to investigate the lower membrane of a whole cell. Recently, this imaging TIRF-FCS was extended to spatial cross-correlation to access diffusion and active transport processes, and membrane organization and heterogeneity in live neuroblastoma cells (102). EMCCD-FCS was also performed with critical angle illumination (103) to obtain an observation volume of tunable depth. Very recently, EMCCD-FCS has been combined with single plane illumination microscopy (SPIM-FCS), allowing for multiplexed FCS in whole planes within a 3D sample (104).

Multiplexed EMCCD-FCS basically aims at combining the high temporal resolution of FCS with the spatial resolution of image correlation spectroscopy (ICS), a method to study the spatial distribution of molecules like concentrations and the aggregation state (105–107). ICS has also merged with temporal correlation for studying slow dynamics of large molecules (k-space ICS (108), raster image correlation spectroscopy (RICS) (109, 110), and spatiotemporal image correlation spectroscopy (111)). Scanning FCS denotes the subset of techniques using spatiotemporal correlation, where only one spatial dimension is scanned periodically, for example along a line (112–114) or on a circle (115, 116). Scanning FCS increases the statistical accuracy, as signal is measured from many statistically independent regions in the sample. However, it still has comparably high time resolution since scanning is limited to one line instead of scanning a whole frame. As a compromise, RICS allows to access the fast microsecond timescales from adjacent pixels along the scanning path, but as well the longer timescales of ms to s from successive lines and frames (110).

3. Detection methods in FCS

To gain most flexibility in changing from one to another of these techniques, two prerequisites are needed. First, excitation modes should be changeable quickly and computer-controlled. And second, detector should be a single-photon counting array without any gaps in between the separate elements, with high quantum efficiency and high time resolution. Such a system would allow for ultra-low light wide-field or TIRF imaging, multiplexed confocal imaging, FCS, ICS and all spatiotemporal acquisition types. However, this type of ultimate detector does not exist yet. Therefore, at first, we start with utilizing an EMCCD.

3.3. Prospects of detection with an EMCCD

As follows from above, both FCS cross-correlations variants would greatly benefit from a flexible spatially resolved detection. Indeed, since multiplexed extensions of the standard APD point detector for FCS were not commercially available, several groups performed parallel FCS with electron multiplying CCD cameras.

Charge-coupled devices (CCDs) are well-established spatially resolved detectors. Scientific grade CCDs are available, which have high quantum efficiencies close to 100% (back-illuminated CCDs), no gaps between the detector elements (100% fill factor), and a continuous shutterless operation (frame-transfer chip). However, the time needed to read one whole CCD image (ms to s) is by orders of magnitude longer compared to the time resolution of a single point APD. Indeed, the time to shift the charges pixel by pixel in the readout process (100 ns) is similar to the time resolution of an APD.

CCDs are charge-integrating devices as opposed to photon counting APDs, meaning that accumulated charges have to be converted to voltages. This is done by on-chip charge amplification and subsequent charge to voltage conversion. High speed operation requires a large bandwidth of the charge amplifier, and hence leads to a high noise level of the read out process. Traditionally, a low readout noise could only be achieved in slow-scan CCDs (< 1 MHz readout rate per pixel, < 10 electrons readout noise).

Electron multiplying (EM-) CCD cameras, which were introduced in 2001 (117), overcome this fundamental limitation by additionally multiplying the charges on chip (on-chip gain) before the conventional charge amplifier (fig. 3.7). The effective readout noise is then the conventional readout noise divided by the gain factor, resulting in sub-electron effective readout noise. Since readout noise is reduced, single electrons can be detected with an EMCCD, even at high pixel readout frequencies.

Multiplication gain is obtained by clocking the charges in the gain register with a higher clock voltage of 20-40 V, compared to normal voltages of 10 V to shift the charges from pixel to pixel. The higher voltage enhances the probability of impact ionization, the process in which a charge with sufficient energy creates an electron-hole pair and hence an additional charge in the conduction band. Although the gain per one cell is only about $g = 1.01 - 1.015$, the total gain over several hundred (N) gain register pixels $G = g^N$ can be easily more than 1000 (118).

Stochastic EM gain process and photon counting

The stochastic nature of the gain process, however, leads to an uncertainty of the input electron level for a measured number of output electrons. For n input electrons and a mean total gain G , the probability distribution of x output electrons (fig. 3.8 a) is approximated by (119):

$$p(x) = \frac{x^{n-1} \exp(-x/G)}{G^n (n-1)!}. \quad (3.1)$$

The mean of this probability distribution for n input photons is nG . The noise introduced by the multiplication process does not depend on the input photon level. For gain factors bigger than 30, the signal to noise ratio is reduced by a constant factor $\sqrt{2}$, which is called the excess noise factor (95). The EMCCD has therefore a reduced effective quantum efficiency (QE) compared to a normal CCD by factor two. The effective QE of a back-illuminated EMCCD is comparable to the QE of an APD (fig. 3.8 c).

A method to overcome the loss in effective quantum efficiency is the operation of the EMCCD in photon counting mode. This is only possible when light levels are well below one photo-electron per exposure (up to 0.5 photons per pixel per readout (119)). Then, a single threshold can be used to distinguish the two cases of zero and one photo-electron. The threshold value has to be carefully chosen (fig. 3.8 b), dependent on the readout noise level and the EM gain. A too high threshold value will result in many photoelectrons not being counted, a too low threshold value will give false positive counts. The readout noise effect can be neglected if the threshold is set above six times the readout noise level ($6\sigma_{\text{read}}$), and the probability to detect the photo-electron is according to equation 3.1 with $n = 1$ (118):

$$P = \sum_{x=6\sigma_{\text{read}}}^{\infty} p(x, n=1) \approx \exp\left(-\frac{6\sigma_{\text{read}}}{G}\right). \quad (3.2)$$

The discussion shows that, although readout noise is overcome for EMCCD cameras by the large EM gain, full quantum efficiency of the detector can only be exploited when maximizing EM gain and minimizing the conventional readout noise. In our FCS measurements, light levels depended on the various exposure times employed in the different data acquisition modi (chapter 5), that were typically higher than one photoelectron per pixel. We therefore did not use any thresholding scheme.

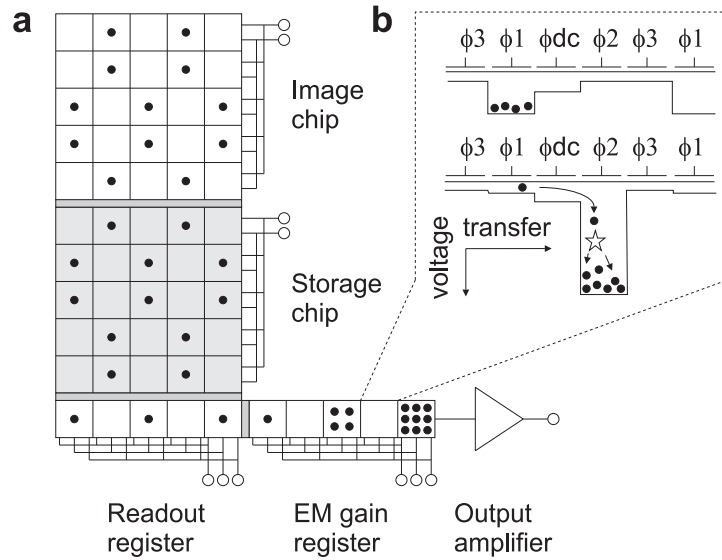


Figure 3.7.: Schematic of the EMCCD chip readout. **a:** Charges (black circles) acquired in the image chip are rapidly shifted to the optically shielded storage chip. While next exposure of the image chip occurs, the storage chip is read out, by shifting lines in the readout register and subsequent horizontal readout pixel by pixel. **b:** An EMCCD has an additional horizontal shift register, the EM gain register, where charges are clocked with the two usual voltage sequences for charge transfer to the next pixel (top), but where one of the three clocked phases (here ϕ_2) is at higher voltage to cause impact ionization (bottom). Figure modified from (95).

3. Detection methods in FCS

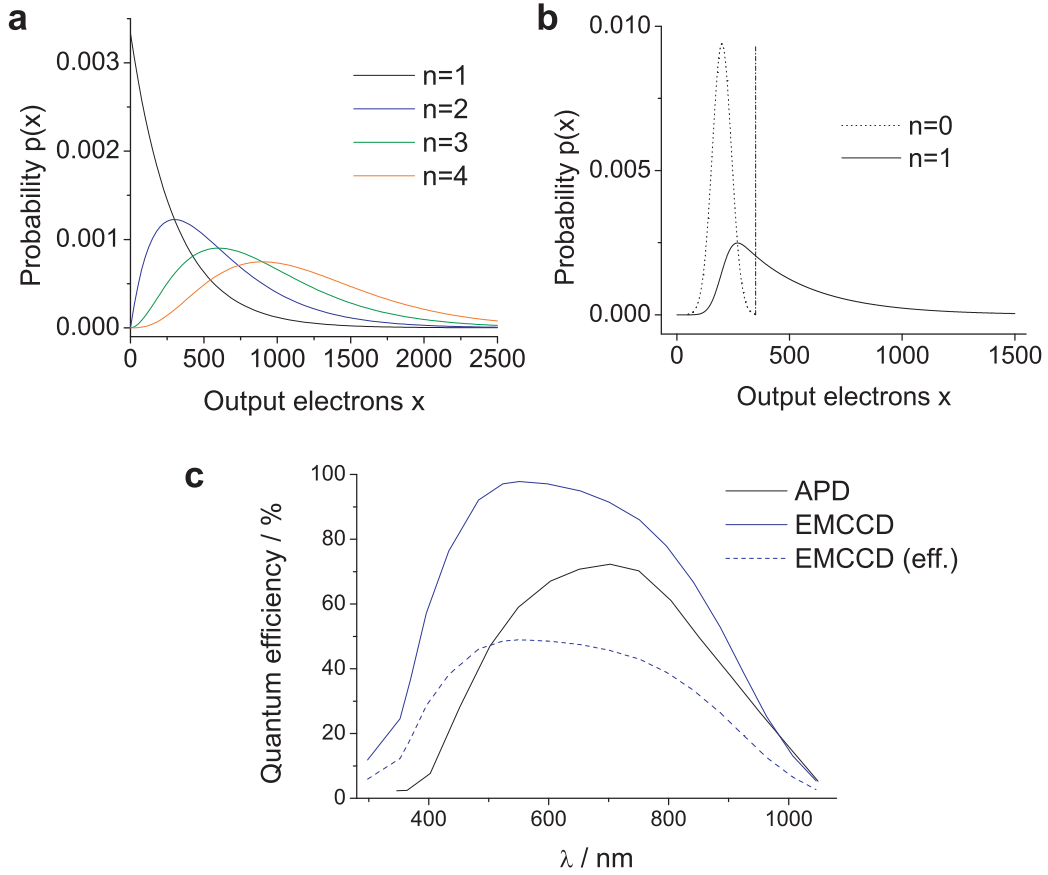


Figure 3.8.: Probability distribution for the number of output electrons after EM gain, and quantum efficiencies of EMCCD and APD. **a:** Theoretical output probability for $n=1$ to 4 input photo electrons, calculated from equation 3.1 with a mean gain $G = 300$. **b:** Output electron signal at very low light levels. Either there is no photo-electron, and only Gaussian readout noise around an electronic baseline offset is detected, or the low light level assures that only one input electron can be present, resulting in the exponential decaying function ($n = 1$), convolved with the readout noise. The vertical line is a threshold value used to distinguish both cases for photon counting. **c:** Quantum efficiency (QE) of an EMCCD compared to an APD. Full QE of the EMCCD can only be exploited in photon counting mode at low light levels. Otherwise, the noise of the EM gain process reduces the QE by factor two, called the effective QE of an EMCCD. This effective QE is on average lower compared to the one of a single photon counting APD.

3.3. Prospects of detection with an EMCCD

For the investigation of clock-induced-charges, a dark noise source in EMCCD cameras (section 7.2), that can be assumed to be a single electron charge per pixel, we used equation 3.1 with $n = 1$. This equation was complemented to include the electronic offset (baseline bl), the conversion factor cf from output EMCCD electrons to digital counts y , and the probability of a clock-induced charge present in a pixel (cic):

$$p(y) = cic \frac{cf}{G} \exp\left(\frac{-(y - bl) cf}{G}\right). \quad (3.3)$$

From the comparison of the properties of an EMCCD to the standard point detector APD, we summarize that EMCCDs have similar sensitivity as APDs concerning quantum efficiency and noise characteristic. The great advantage of the EMCCD is the spatially resolved, array-based two-dimensional detection with great flexibility, but time resolution is much lower than for the single-point detector APD. It is likely that readout speed of future camera generations will increase further. Additionally, novel detectors for single-molecule fluorescence and spectroscopy are expected to be developed (67). At present, for the investigation of EMCCD-FCS, we will employ different methods to enhance the time resolution by only using part of the chip (chapter 5).

Part II.

Establishment of an EMCCD detection platform for FCS

Establishment of an EMCCD detection platform for FCS

In this part of the thesis, we describe in detail all steps to perform FCS with an EMCCD. The experimental setup and basic prerequisites are discussed in chapter 4. In chapter 5, we explain the different camera readout modi and discuss all EMCCD hardware settings. The developed data acquisition and data evaluation software is presented and after that, first measurements of different molecules in solution are shown in chapter 6.

In chapter 7, we discuss the main limitations of the camera model used in this part and compare it to another camera model. We conclude from this technical part, that EMCCD-based FCS is a versatile alternative to classical APD-FCS, and resulting autocorrelation curves in both detection methods are in good agreement.

4. Optical setup for FCS with EMCCD detection

A home-built confocal FCS setup (section 2.2) consists of a microscope (objective lens, filter sets and tube lens), an excitation laser, and the detection optics including the detector. The alignment for FCS is typically done in repeated steps of optimizing the excitation and detection path. The performance is checked with a diffusion measurement of a standard dye in solution. Suboptimal alignment in either of both paths can lead to similar effects in the autocorrelation curve, mostly recognized by a larger diffusion time, a higher structure parameter or a lower effective molecular brightness of the molecules than expected. To exclusively investigate the novel detector EMCCD for FCS, we extended a complete standard APD-FCS setup by a detection path for the EMCCD camera. This assured that:

- Calibration of the FCS excitation pathway (laser beam alignment, cover slide correction collar of the objective lens) and mounting of the sample could be quickly performed with standard APD-FCS.
- Reference APD-FCS curves could be taken before, in between and after extended EMCCD-FCS measurements series to confirm stable conditions (for example regarding the sample concentration).
- Laser excitation (beam diameter and power), mostly determining the size of the confocal volume, was the same for both measurement types. Therefore, resulting FCS curves from both detection methods could be directly compared.

4.1. Integrated setup with both detectors APD and EMCCD

The integrated FCS setup with both detectors was based upon an inverted microscope (IX71, Olympus, Germany) with a 60x water immersion objective (Fig. 4.1). For first test measurements, reported in this part of the thesis, we employed a 488 nm laser line (Stabilite, Spectra-Physics, Darmstadt, Germany), a dichroic mirror (LP 505) and a bandpass filter (HQ 535/70M, AHF, Tübingen, Germany), suitable for various fluorescent probes in the green spectral region. The laser beam was expanded by a lens telescope to slightly underfill the back aperture of the objective lens and attenuated by neutral density filters (New Focus, San Jose, California) to approximately 5 μ W before entering the objective. Nanomolar concentrated sample solution was either pipetted as a droplet on a cover slide or enclosed in different types of chambers to prevent evaporation (section 4.2).

The detection method was chosen by utilizing either the left or right side port of the microscope. We verified that the output efficiency of both side ports differed by less than 5%, in accordance to the specifications of the manufacturer. The mechanics of the two side port switches was slightly different influencing the stability and reproducibility per switch (section 4.2).

For APD detection, we chose the left side port (fig. 4.1 b) as this is the well-established standard for most of our FCS setups with the IX71-microscope. In the primary image plane, a multimode optical fiber of core diameter 50 μ m is positioned (Thorlabs Europe, Karlsfeld, Germany), serving as the confocal pinhole. This end of the optical fiber is mounted on μ m-translational stages in all three

4. Optical setup for FCS with EMCCD detection

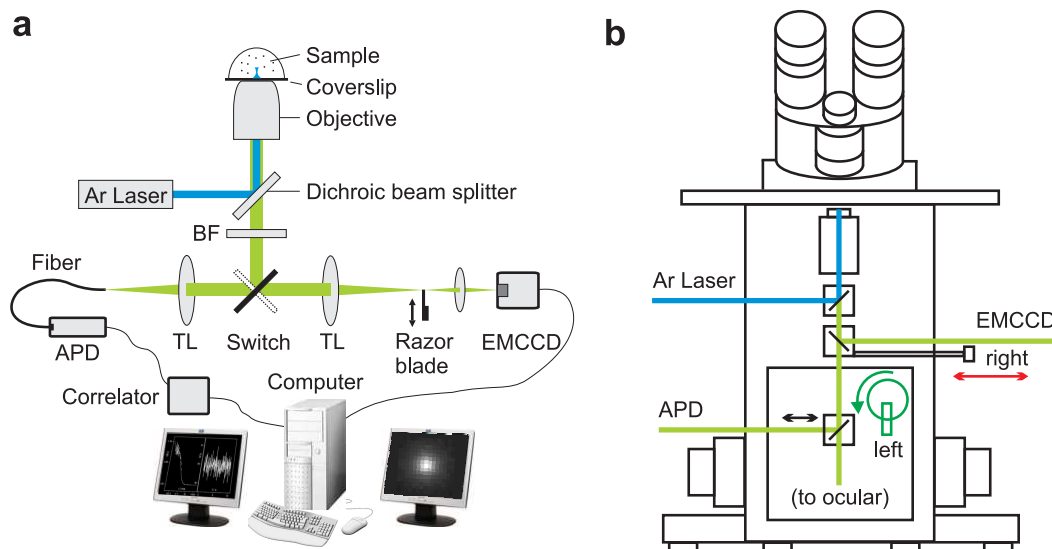


Figure 4.1.: Optical setup for FCS with APD or EMCCD detection. **a:** Optical components and detection pathways (BF: bandpass filter, TL: tube lens). **b:** Detailed optical path and switches of the inverse microscope IX71 (Olympus).

spatial directions (Owis, Staufen, Germany) with a spindle pitch of 0.25 mm per turn, corresponding to a position accuracy of 1 μm . The other end of the fiber is connected to a fiber coupled avalanche photo diode (APD, SPCM-AQR-13, PerkinElmer Optoelectronics, Fremont, California), that operates in single-photon counting mode. The APD signal is fed into a digital multiple-tau correlator (ALV, Langen, Germany), which displays the instant averaged count rate and correlation function in real-time. Therefore, the setup can be aligned while measuring to optimize both, the fluorescence intensity and the correlation amplitude.

For EMCCD detection, we utilized the right side port, which is usually a camera port intended for wide-field imaging. The electron multiplying CCD camera (EMCCD iXon DV860, Andor Technology, Belfast, Northern Ireland) was first positioned in the primary image plane as well. For the advanced fast kinetic acquisition mode (section 5.2), however, we mapped the primary image of the focal spot 1:1 onto the EMCCD by an additional achromatic lens and inserted a razor blade (see fig. 4.1 a) in the primary image plane for optically shielding the lower part of the camera chip. For the measurements in this part of the thesis, the EMCCD was mounted on μm -translational stages (Standa, Vilnius, Lithuania) with a larger spindle pitch of 0.5 mm per turn, and hence slightly lower positional accuracy (section 4.2).

The EMCCD was operated by a home-written program (section 5.3) based on the LabView (National Instruments, Austin, Texas) driver supplied by Andor, and image sequences were evaluated offline using a home-written program (section 5.4) written in Matlab (MathWorks, Natick, Massachusetts). Correlation curves were fit with Origin (OriginLab, Northhampton, Massachusetts) or Matlab (31), based on a nonlinear least square Levenberg-Marquardt fit routine.

4.2. Technical requirements: adjustment and stability

Typical EMCCD-FCS measurements times were much longer ($> 10\times$) than APD-FCS measurements, mostly due to the camera readout gaps in the fast kinetic acquisition mode (section 5.2) and due to the necessary multiple series of acquisitions with different exposure times. Therefore, a key prerequisite to obtain reproducible results from EMCCD-FCS is the stability of the optical setup and the sample. We briefly name the important sources of instabilities and how they can be avoided.

4.2.1. Stability of the optical setup

Microscope stability

Due to the different ports of the microscope used for excitation and emission beam paths (fig. 4.1 b), a slightly tilted microscopy body leads to a lateral shift of the position of the primary image. This effect is even stronger if the primary image is mapped again and the camera is positioned in a secondary image plane. Additionally, the CCD camera is a more sensitive device to check for spatial drifts than the APD, where the effect can only be recognized indirectly by a change in the autocorrelation curve.

We noticed that even a little touch on the microscope body slightly influenced the position of focal spot image on the camera. This source of instability could be eliminated easily by tightly fastening the microscope body onto the optical table. Additionally, we used rigid one inch post and mirror holders and ultra-stable mirror mounts (Thorlabs Europe, Karlsfeld, Germany).

Laser stability

For the solid state laser (Sapphire 488-20, Coherent, Dieburg, Germany), we employed in part of the measurements (chapter 8), we observed remaining drifts of the focal spot image that could be attributed to small variations of the laser beam angle. This was observed for several hours of laser warming up (compared to usually less than an hour for power stability) and it was due to the slowly warming up of the aluminium block that served as a mounting support for the laser. We avoided this effect by switching on the laser at least four hours before the measurement. A complete elimination of this effect could in principle be obtained by using a fiber coupled laser.

Side port switch reproducibility

Side port switches need to be operated many times in an experiment, as the sample positioning is observed by transmitted light through the ocular, and APD and EMCCD-FCS measurements are performed repeatedly. We noticed that the right side port switch was less accurate than the left one. This is due to the different switch mechanisms (fig. 4.1 b). For the left side port selection, a turning knob is actuated which moves an internal slide carrying a prism via a cable pull. The sliding carriage has a very precise click-stop that assures good reproducibility per switch.

The right side port also employs an internal slide, carrying a mirror in this case. The mechanical force to move the slide, however, is directly transmitted by pulling a metal connecting rod, and there is a simple mechanical stop without a click-stop. The switching is hence less accurate and less reproducible, but apparently good enough for typical wide-field imaging.

We checked the switching accuracy with sub-resolution fluorescent beads and a standard CCD camera ($6.5\ \mu\text{m}$ pixel size) positioned at both primary image planes. The reproducibility of the left

4. Optical setup for FCS with EMCCD detection

side-port switch was better than $2\text{ }\mu\text{m}$. This accuracy was sufficient compared to the typically employed confocal pinhole of $50\text{ }\mu\text{m}$ diameter. The right side port switch had an insufficient reproducibility of more than $50\text{ }\mu\text{m}$ lateral shift. The position of the observed image of the fluorescent bead varied easily by ten pixels on the CCD camera.

We reduced this effect by upgrading the right side port switch with a custom-made click-stop (Olympus). The switching accuracy was considerably improved to approximately $6\text{ }\mu\text{m}$ lateral shift. Still, a precision similar to the left side port switch could not be attained due to the direct mechanical force applied by the connecting rod. Therefore the EMCCD camera had to be sometimes slightly readjusted after side port switching.

EMCCD precise positioning and stability

The EMCCD camera itself had to be stably mounted to the same extend of a few micrometers. However, at the same time, the camera needed to be adjustable with micrometer precision for aligning the image of the detection volume to the center of a pixel. The employed stages (Standa, Vilnius, Lithuania) were intended for a micrometer precise translation of the EMCCD, that had a mass of approximately 5 kg, together with a custom made rigid aluminium frame for mounting. We observed, that the micrometer screws could not be turned smoothly due to the heavy load, resulting in a difficult alignment. Therefore, we only used this configuration of the EMCCD being adjustable in all three spatial dimension for initial calibration measurements to find the optimum axial and lateral position.

In later precision two-focus FCS measurements, we fixed the camera tightly to the optical table in the correct axial position of the secondary image plane. The lateral position of the fluorescence spot could be coarsely shifted on the camera by a movable mirror in the detection path, inserted between the achromatic lens and the camera. To precisely center the focal spot onto the camera pixels, we developed an automated realignment procedure of the focal volume by slightly changing the angle of the excitation laser before being coupled into the objective lens (section 8.2).

4.2.2. Stability of the sample

For extended EMCCD-FCS measurements series, the sample stability is of particular importance. For quick FCS alignment measurements, performed in several minutes, typically only a droplet of sample solution (approximately $30\text{ }\mu\text{l}$) is pipetted on a cover slide and mounted on the microscope stage (fig. 4.2 a). Over time, the concentration of the fluorescent molecules changes due to evaporation of water.

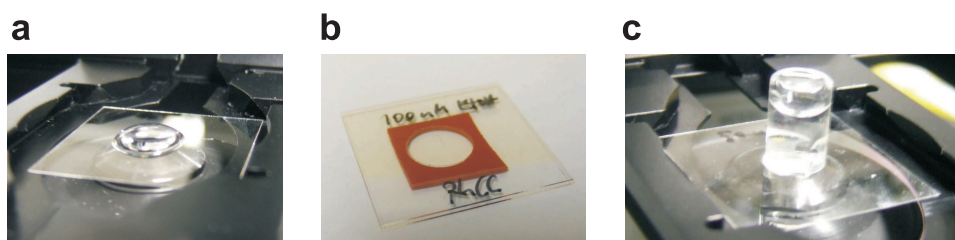


Figure 4.2.: Sample chambers for concentration stability. The sample solution in form of a droplet (a) does not exhibit a stable concentration of fluorophores over time due to evaporation of the solvent (water). Therefore, closed chambers are utilized (b and c). In the hermetically sealed chamber made from solely glass (c), the concentration is stable over months.

4.2. Technical requirements: adjustment and stability

To prevent evaporation, usually a larger volume is pipetted in different types of closed chambers. A commercially available system is for example the Lab-Tek chamber (Nunc, Wiesbaden, Germany), which is a plastic chamber with a cover glass bottom and a loosely fit plastic lid. In typical eight-well chambers, each well has a volume of 200-400 μl . Concentration is much more stable in these chambers, but remaining evaporation still changes the concentration over days and hydrophobic molecules tend to stick to the plastic.

A simple home-built chamber can be created by two cover slides and an adhesive silicone ring (Strattech, UK) of 1 mm height (fig. 4.2 b), employing approximately 40 μl sample solution. The concentration in this closed chamber is more stable but still changes after several days due to water evaporating through the silicon, noticeable by air bubbles in the solution.

We therefore created hermetically sealed sample containers made solely from glass. We pipetted approximately 50 μl sample solution in little glass vials (CZT, Kriftel, Germany), applied two-component adhesive (R&G, Waldenbuch, Germany) on the rim and closed them with a cover slide (fig. 4.2 c). The concentration in these samples was stable over months.

When measuring the dye Rhodamin 6G (Invitrogen, Karlsruhe, Germany) and the enhanced green fluorescent protein (eGFP; Clontech, Mountain View, California), we observed a strong adhesion of the molecules to the cover slide, noticeable by a continuous decrease of the fluorescence count rate in the solution over time and bright fluorescence when focusing the laser onto the cover slide. The unspecific binding was efficiently reduced for eGFP by coating the cover slide surface with bovine serum albumin (BSA), and for Rhodamin 6G by coating it with polyethylene glycol (PEG).

5. EMCCD data acquisition for FCS

In standard FCS using avalanche photodiodes (APD), the photon counts are continuously detected. A hardware correlator instantaneously calculates the autocorrelation curve with a high temporal resolution of about 200 ns. Therefore, no parameters in the detection process have to be set, apart from the overall measurement time.

EMCCD detection, in contrast, is an imaging method, where exposure times and frame rates have to be chosen. The fluorescence signal time trace has to be extracted from the acquired image sequences and correlation curves are calculated offline after the measurement. This chapter describes all important settings in the detection and data evaluation process for the EMCCD model iXon DV860 (Andor Technology).

5.1. Frame transfer mode for ms time resolution

In frame transfer mode, also named kinetic mode, the camera acquires data quasi-continuously. After an exposure of the 128×128 pixel image chip, the whole frame is rapidly shifted vertically to the same sized optically shielded storage chip, enabling a shutterless operation. While the storage chip is readout, the next exposure is taken. The highest frame rate or correspondingly shortest possible exposure time for a full frame acquisition at the fastest readout frequency (10 MHz) is 2 ms. It is largely determined by the time of 1.6 ms needed to sequentially readout the 128×128 pixels. The parallel vertical frame shift is comparably fast (38 μ s) and hence does not affect the full frame rate much.

Higher time resolution is possible by only using a subregion of the image chip in terms of a limited number of CCD rows, since the readout of the storage chip can be performed faster in this case. Unused rows below and above the region of interest are binned together and readout as one line. Reducing the number of columns to be readout, in contrast, does not increase the speed but still reduces the data file size.

For FCS measurements, we used the following acquisition settings:

A **subregion** of 5×5 pixels was employed (pixel size is $24 \mu\text{m} \times 24 \mu\text{m}$ for this camera model), corresponding to a square of $120 \mu\text{m} \times 120 \mu\text{m}$ in the image plane. For comparison, the optical fiber core diameter used for detection with the APD has a diameter of $50 \mu\text{m}$. Together with the settings described below, the minimal exposure time was 0.26 ms, resulting in a kinetic cycle time of 0.3 ms (exposure time plus frame shift time). This cycle time is the time resolution of the autocorrelation curve. Note that the vertical frame shift of (38 μ s) does affect the frame rate when using such short exposure times. A sketch of the kinetic acquisition mode is shown in fig. 5.1.

Readout frequency, also called horizontal readout rate, was set to the highest possible value of 10 MHz. The only advantage of choosing a lower readout frequency would be a reduced readout noise (130 electrons at 10 MHz) by approximately factor two, but readout noise is largely overcome by on-chip gain in EMCCD cameras (section 3.3).

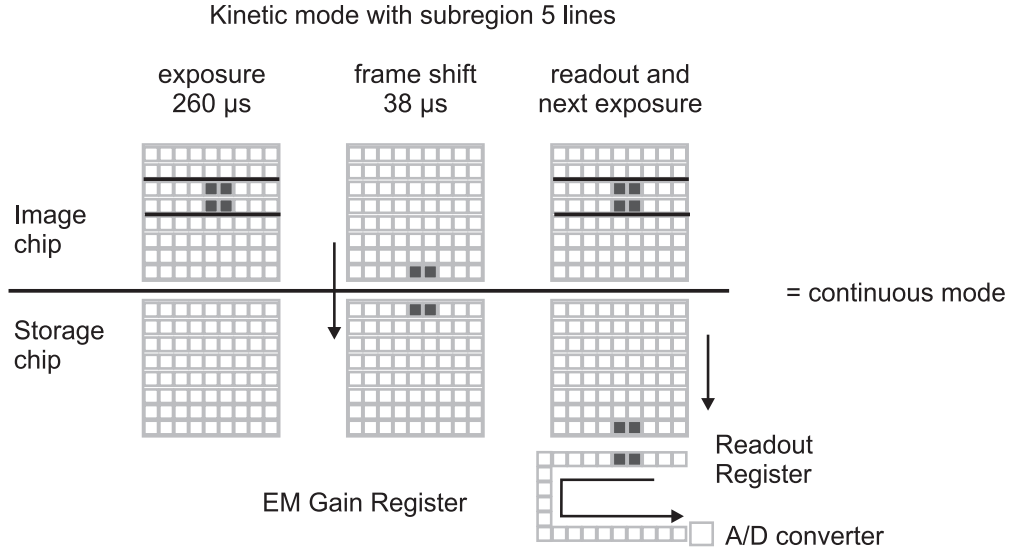


Figure 5.1.: Sketch of the timing in the kinetic mode. For a vertical subregion of, for example, five CCD lines, a minimal exposure time of 260 μ s can be set. This results in a continuous data acquisition with a time resolution of 0.3 ms.

Vertical shift time and voltage was set to the fastest recommended value of 0.3 μ s per line, resulting in 38 μ s frame shift time for 128 CCD rows. The vertical shift time is the time the voltage is applied to vertically shift the charges. Using a faster shift time can reduce the charge transfer efficiency, noticeable by vertical stripes below and above a bright signal. This, in turn, can be compensated for by increasing the vertical clock voltage amplitude. However, reducing the shift time and increasing the voltage leads to overall higher clock-induced charges, which is the dominating source of dark signal in EMCCD cameras (section 7.2). We verified that charge transfer efficiency was good for the standard normal voltage setting and a shift time down to 0.3 μ s.

Electron multiplying gain (EM-gain) is the on-chip multiplication of the electrons before readout (section 3.3). The gain should be set to a value higher than the readout noise, resulting in “sub-electron effective readout noise”, as denoted in the specifications of EMCCD cameras.

For this camera model DV860, the gain is set in a range (0,255). The actual gain increases exponentially with this software setting and it additionally depends on the cooling temperature (in the EMCCD model DU897, used in part III of this thesis, the real gain can be directly set). Therefore, the gain characteristic has to be determined in a calibration measurement for a given temperature. This can be easily done using any stable light source and comparing the obtained signal from a measurement with and without gain. We set the thermoelectric cooling to the minimal possible value of -60°C to obtain maximum EM-gain. By using the average fluorescence signal of a dye solution (100 nmol), we determined an actual gain of factor 450 at full gain setting (software setting 255). This gain was used for all FCS measurements with this camera model.

Preamplifier gain is the classical amplifier before the analog-to-digital conversion (ADC). It determines the conversion factor from electrons into digital values. It can be varied to adjust the conversion factor to the light level present in the experiment, since dynamic range of the sensor (given in electrons full well capacity of a pixel) is typically larger than the dynamic range of the ADC (given in bit). To detect low light levels, as present in FCS, with highest sensitivity, the smallest conversion

5. EMCCD data acquisition for FCS

factor is used. This is, in turn, the highest preamplifier gain setting. For this camera model, this is the setting $\times 5$ preamplifier gain, corresponding to a conversion factor of 18 electrons per digital count.

Baseline clamp option was used throughout the measurements with the EMCCD DV860. If this option is set, the varying electronic offset of the analog-to-digital conversion is corrected. This is performed on hardware level for each frame by subtracting the average dark signal from optical shielded dummy rows on the chip. Without using the baseline clamp option, fluctuations in an FCS measurement are dominated by fluctuations of the baseline, and autocorrelation curves are largely distorted.

However, we noticed that the baseline clamp option is problematic for the fast kinetic mode, since it can introduce additionally noise and it does not correct for baseline variations across the chip. We therefore created our own baseline correction in part III of this thesis (section 9.1).

First FCS measurements in the kinetic mode were performed with nanomolar concentrated solution of CdSe/ZnS quantum dots (Evident Technologies, Troy, New York). Quantum dots are semiconductor nano-particles, that are used in certain applications of fluorescence microscopy and FCS as a substitute of organic dyes (12, 120). Here, we employ them due to their comparably long diffusion time in the range of ms, perfectly suitable for measurements in the kinetic mode.

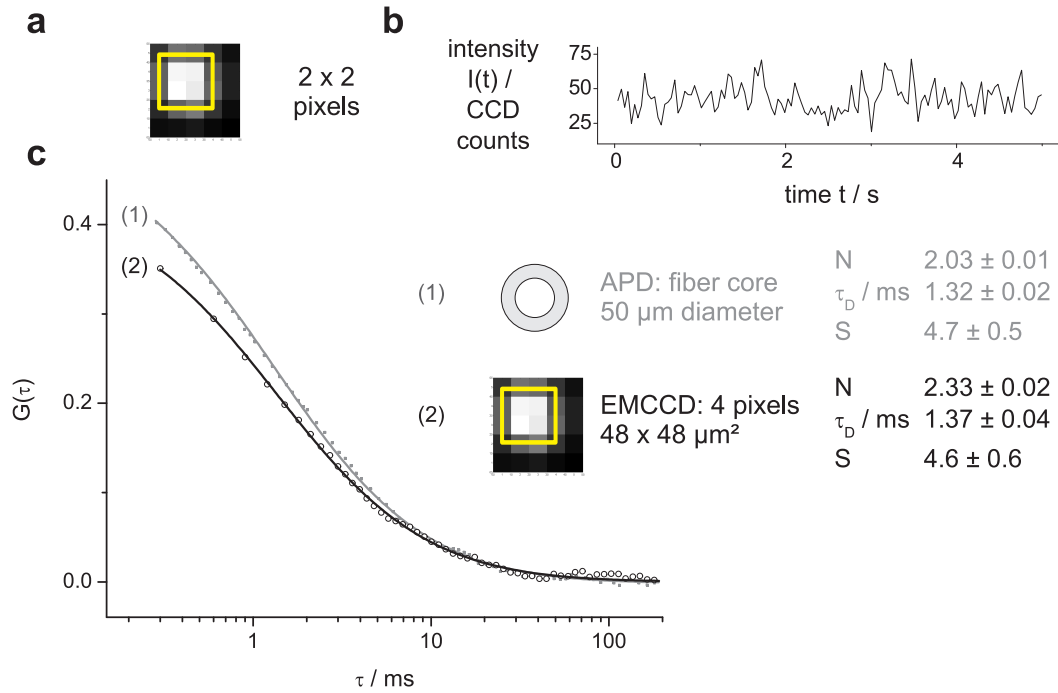


Figure 5.2.: EMCCD-FCS in kinetic mode. **a:** Integrated image over time from a stack of 60,000 exposures (18 s) of a measurement for quantum dots. **b:** Signal trace over time from 2×2 pixels marked by the yellow box in (a). **c:** Autocorrelation curve from the EMCCD signal, compared to an APD-FCS measurement and deduced fit parameters. Symbols: data, lines: fit.

A kinetic stack of 60,000 images (18 s) was recorded, together with a second dark measurement. The mean dark signal was subtracted pixel-wise from each image in the stack. Fig. 5.2 a shows the integrated image over time. The signal from the marked region of 2×2 pixels on the CCD is summed for each image in the stack, yielding a signal-trace over time (fig. 5.2 b). The autocorrelation function of this trace is shown in fig. 5.2 c, together with a curve from APD detection (measurement time

was 100 s). Both autocorrelation curves are very similar as they have a comparable amplitude and temporal decay.

Data were fit with the standard model function for free diffusion through a three-dimensional Gaussian detection volume (equation 2.28). The extracted fit parameters are given in fig. 5.2 c, showing good agreement. The square pinhole of the EMCCD leads to a slightly bigger focal volume. The structure parameter is in the expected range for both curves, indicating that the approximation of a three-dimensional Gaussian detection volume holds for square confocal apertures, too.

Having a time resolution of 0.3 ms, the kinetic mode can easily be used to perform FCS measurements of free diffusion in solution of comparably large fluorescent particles as the used quantum dots. Their diffusion coefficient is $D \sim 15 \mu\text{m}^2/\text{s}$. The kinetic mode can also be used in systems where diffusion is generally slower than in solution, for example in cells due to the higher viscosity or in membranes.

5.2. Fast kinetic mode for μ s time resolution

Obviously, a faster temporal resolution of EMCCD-FCS is needed to monitor the more commonly used, smaller fluorescent probes. These are fluorescent proteins or organic dyes like Alexa Fluor 488 with a diffusion time in solution of approximately 60 μ s through the focal volume. The usual frame transfer mode of the EMCCD cannot achieve this time resolution, since the readout time of the storage chip determines the minimal exposure time and even the frame transfer time itself (38 μ s) is in this time range.

To overcome this limitation, we therefore adopted another mode called fast kinetic mode. The basic idea of this mode is to illuminate only several rows of the image chip and rapidly shift the acquired charges down by only several lines out of the illuminated region. Since the complete frame shift is avoided, a repeated acquisition is possible with exposure times down to 1 μ s and cycle times given by the sum of exposure and the shift time for only several lines.

In order to perform as many exposures as possible, it is preferable to use the top lines of the image chip for illumination, so that most of the image chip and the storage chip both are used to store images. Because, for measurements in solution, the out-of-focus light is not imaged into the pixels corresponding to the focus but spread to neighboring area, the bottom part of the image area, used now to store the previously illuminated (already shifted) lines, has to be shielded from the light in subsequent exposures. Note that a shielding would be required as well when using the bottom lines of the image chip, to prevent out-of-focus light from previous exposures to be shifted into the lines used for illumination.

A direct shielding of the EMCCD chip was not possible since it is inside the camera housing. Therefore, an indirect shielding was applied as follows. The image of the focal spot was mapped 1:1 onto the EMCCD by an achromatic lens (see fig. 4.1 a). A vertically adjustable razor blade was inserted in the primary image plane of the microscope to block part of the out-of-focus light, thus effectively shielding the bottom part of the image chip used now as a storage area. The edge steepness of this shielding was determined to be about two pixels, meaning that one row (and the part of the chip below) could be completely shielded and the signal two rows further up (and the part of the chip above) were not influenced. By using the top 6 CCD rows for illumination (as described later in this section) and the signal from 2x2 pixels (the middle 2 rows contained the 2×2 pixels used for data analysis), an efficient blocking could be achieved without reducing the signal in the favored pixels.

5. EMCCD data acquisition for FCS

The number of possible exposures depends on the chip size. If both chips are filled, they have to be read out and therefore, the measurement is finished, meaning that the fast kinetic mode is not a continuous mode. Rather, one can achieve a faster time resolution by renouncing a continuous acquisition, as employed in the kinetic mode, but the readout is still the speed-limiting process.

Considering for example 6 lines at the top of the image chip for illumination and a vertical shift time of $0.3 \mu\text{s}$ per line, the image transfer of the 6 lines takes $1.8 \mu\text{s}$. An exposure time of $20 \mu\text{s}$ is chosen which is sufficiently longer than the shift time, similar to the ratio in the kinetic mode. With these settings, 40 images are recorded in about 0.87 ms to fill both chips, named one fast kinetic series. Before the next fast kinetic series can be started, both chips have to be read out. A reduced readout frequency of 3 MHz had to be used (explained in section 7.1) and we experimentally obtained a readout gap of 25 ms . The other camera settings were the same as in the kinetic mode. A sketch of the fast kinetic acquisition mode and the timing are shown in fig. 5.3.

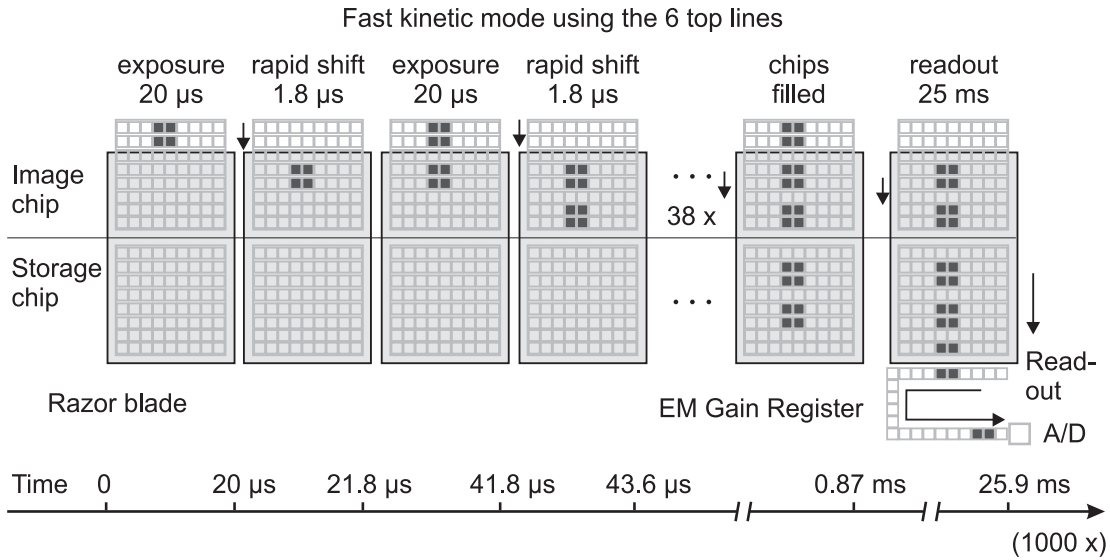


Figure 5.3.: Sketch of the timing in the fast kinetic mode. Rapidly shifting only the top six illuminated lines under an optically mask allows for high time resolution of, for example, $21.8 \mu\text{s}$, defined by the exposure time and the shift time. After a limited number of exposures, both chips are filled and need to be read out, before the next fast kinetic series can be started. The fast kinetic mode is hence a non-continuous data acquisition mode.

Note that the readout speed does not determine the time resolution in the fast kinetic mode. Rather, it determines the ratio of effective measurement time to total measurement time, which we call the usage of the measurement time (figure 5.4 d).

EMCCD-FCS measurements in the fast kinetic mode were performed, for example, using nanomolar concentrated solution of enhanced Green Fluorescent Protein (eGFP; Clontech, Mountain View, California). They were carried out by starting 1,000 fast kinetic series in a loop with a total measurement time of 26 s , compared to an effective measurement time of 0.8 s , hence a time usage of only 0.03 . The data analysis was performed by correlating the fluctuations $\delta I(t)$ of each single short fast kinetic trace (equation 2.11), using the temporal average intensity $\langle I(t) \rangle$ over the whole measurement time. The resulting normalized correlation curves of the 1,000 repetitions were averaged, and in the mean autocorrelation curve, data points for lag times larger than ten times the exposure time ($\tau > 0.2 \text{ ms}$) were averaged on a logarithmic time scale (fig. 5.4).

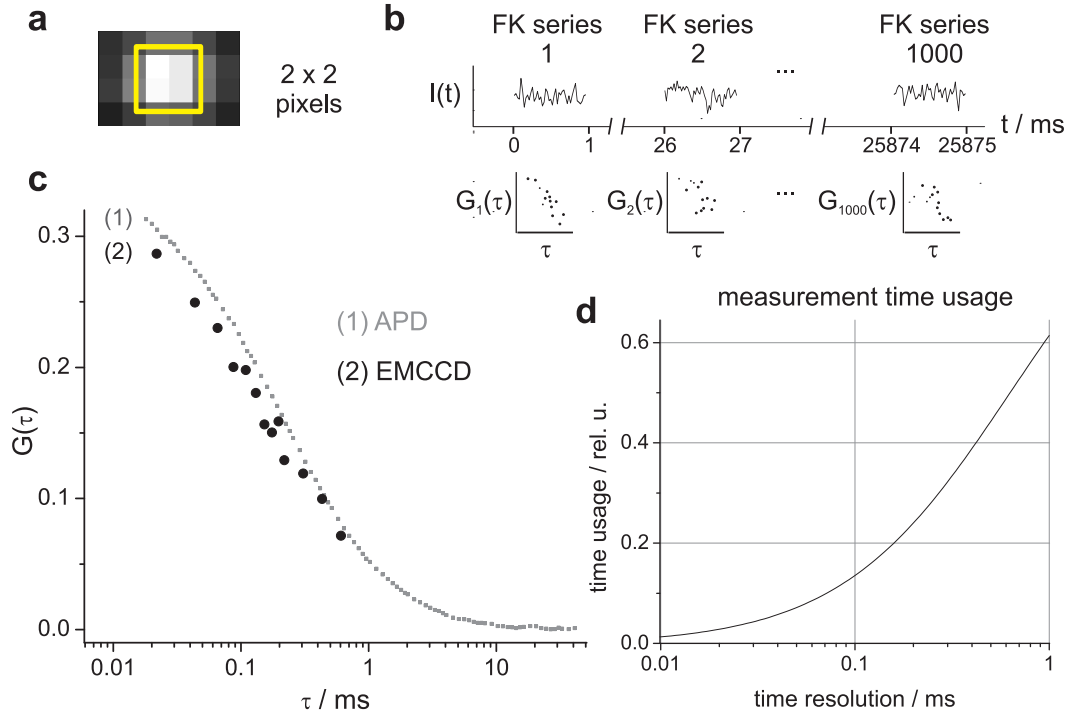


Figure 5.4.: EMCCD-FCS in fast kinetic mode. **a:** Integrated image over time from 1,000 fast kinetic series, each 40 exposures. **b:** Sketch of signal traces over time and individual autocorrelation curves. **c:** Averaged autocorrelation data from the 1,000 fast kinetic series, compared to an APD-FCS measurement. **d:** The measurement time usage depends on the time resolution.

The deduced autocorrelation data of the fast kinetic measurement (fig. 5.4 c) agrees well with a curve from APD detection (measurement time was 100 s), as in the kinetic mode. The limited time range of the autocorrelation data from EMCCD-FCS is due to the short individual fast kinetic series of only 0.87 ms, and the lower signal-to-noise ratio is due to the much shorter effective measurement time of 0.87 s. Therefore, EMCCD-FCS typically involves several measurements at different time resolutions in the fast kinetic mode or the kinetic mode to obtain a correlation curve over a sufficient time range. Examples and fit results are given in chapter 6. Before, we briefly mention the background correction, and we give an overview over the developed software for data acquisition and evaluation in sections 5.3 and 5.4.

Background correction versus signal level

The real photo-electronic signal of the CCD has to be well distinguished from the electronic offset level (the CCD baseline mentioned before) to assure a proper normalization in the correlation analysis. Therefore, background measurements were always done, which were equivalent acquisitions but with the CCD shutter closed. Background subtraction was performed to remove any fixed pattern, for example a different baseline of individual pixels. In the kinetic mode, the average dark image was subtracted from each image in the stack. In the fast kinetic mode, the mean dark image of the exposed double-chip, obtained by averaging over the number of fast kinetic series, was subtracted from each fast kinetic series.

5. EMCCD data acquisition for FCS

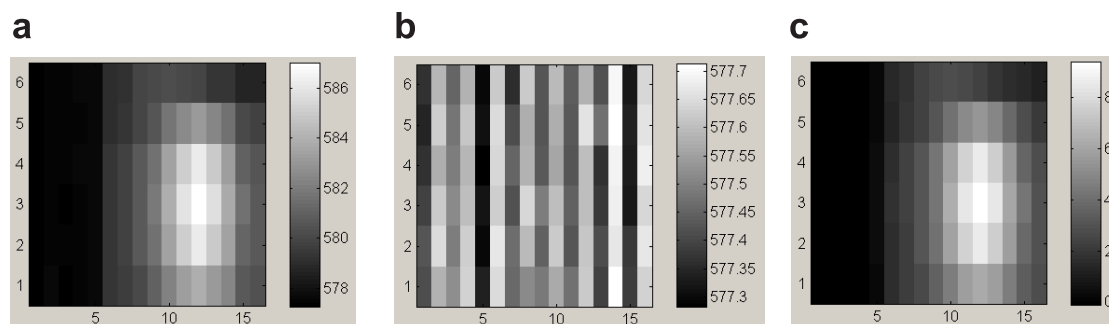


Figure 5.5.: Background subtraction. **a:** Average image of a fast kinetic measurement with exposure time of 50 μ s. **b:** Average dark image. **c:** Resulting background corrected image.

To illustrate the background variation and typical signal level in the mostly employed fast kinetic mode, the average image of a measurement with exposure time of 50 μ s is shown in fig. 5.5, together with the average dark image and the resulting background corrected image.

The baseline level is about 577 counts. The actual value is not relevant, it varies with acquisition settings and cooling temperature. It even can be intentionally decreased or increased in the software in steps corresponding to approximately 100 counts to optimize the usable dynamic range of the CCD and assure non-negative values, respectively.

More importantly, the background image exhibits brightness variations at different CCD columns of 0.4 CCD counts. According to the manufacturer, these structures are related to the horizontal readout process. We observed that they are not fixed for specific physical columns of the camera, but they change when using different acquisition settings like subregions or readout frequencies.

The maximum signal level (corrected image fig. 5.5 c) in the brightest pixel is around 9 CCD counts. Therefore the systematic background pattern does not influence the result much. But what do these 9 CCD counts mean? Can we relate them to more commonly used values in FCS? In this example, we used typical FCS measurement conditions: 1 nmol/l concentrated solution of Alexa Fluor 488 dye and a laser power of 18 μ W, which yielded a molecular brightness of 16 kcpms, deduced from APD-based detection.

We can compare the photon count level detected with the APD to the EMCCD signal (the camera model DU897 was used here: pixel size 16 μ m \times 16 μ m, conversion factor 12 electrons per one CCD count, EM-gain was 300). With the APD, we detected 40 kHz photon count rate. Assuming a quantum efficiency of the APD of 65% and that of the CCD of 95%, we therefore expect to obtain on average 2.9 electrons in the short exposure time of 50 μ s of the camera. These electrons are expected to be multiplied by the EM-gain to 877 electrons, and then converted to 73 digital counts in the CCD image. The 9 pixels, that approximately correspond to the circular pinhole of the 50 μ m optical fiber, exhibit a sum of 74 CCD counts, which is a good agreement.

At this signal level, the background variation was not of much importance. However, for lower laser powers, lower sample concentration or shorter exposure times, the background subtraction was more important. Although background can be corrected for, we performed EMCCD-FCS typically with slightly higher concentrations of fluorophores to always assure that at least 10 CCD counts of signal per pixel were detected for the shortest exposure time employed.

It has to be noted, that this simple subtraction of a time averaged reference dark measurement series was not sufficient in the fast kinetic mode. The dark measurement signal itself showed a non-zero correlation that had to be corrected for in the analysis (equation 2.52). This effect, which was

not present in the kinetic mode, might originate from a remaining varying baseline offsets across the chip and for different fast kinetic series, despite using the baseline clamp feature of the camera. For two-focus FCS measurements, presented in part III of this thesis, we deselected the baseline clamp option but used several optically shielded columns of the chip as baseline reference (section 9.1).

5.3. LabVIEW based acquisition software

Acquiring data for FCS can be partially performed with the standard camera imaging software, called ‘Andor Solis’. For example, a kinetic stack can be easily taken. However, due to the fast exposures used for FCS, the signal per frame is weak and data needs to be processed during or after the measurement in order to judge the result. Additionally, the fast kinetic mode is implemented in ‘Solis’ only as one fast kinetic series (one exposure series until the double chip is filled).

To gain complete flexibility of data acquisition in general, we operated the EMCCD by a home-written software program based on the LabVIEW (National Instruments, Austin, Texas) driver supplied by Andor (software developmental kit). The principle structure of LabVIEW is given in fig. 5.6 for an example part of the graphical program code.

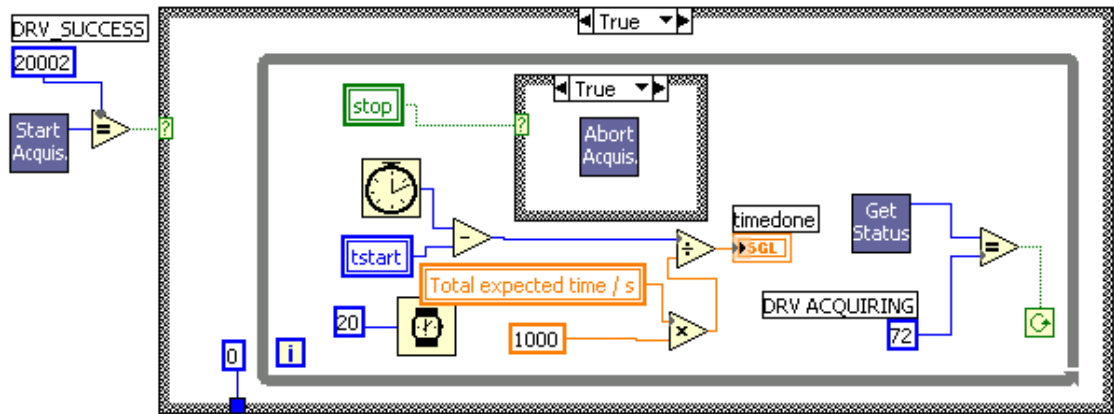


Figure 5.6.: EMCCD-FCS acquisition software: example part of the LabVIEW block diagram (the program code). The program is built by graphically connecting functions and variables. The variables relate to the controls and indicators in the front panel (fig. 5.7). The functions (virtual instruments, VIs) are either inbuilt (like the clock symbol to get the actual system time) or supplied by the manufacturer of the hardware instrumentation (like the three camera commands). In this example part, the data acquisition is started by calling the VI ‘Start Acquis’, and then a loop runs until either the user has pressed ‘STOP’ in the front panel or until the result from calling ‘Get Status’ is not any more ‘DRV ACQUIRING’, but acquisition is finished.

5. EMCCD data acquisition for FCS

The user interface of the software is shown and commented in fig. 5.7. The features and advantages of our program are the following:

- In addition to all functions of 'Solis', it is possible to perform fast kinetic acquisitions in a loop, this being the most important mode for EMCCD-FCS.
- Temporally averaged images and signal traces from designated pixels are displayed. Without this information, acquisition results can hardly be interpreted.
- Different acquisition modi can be switched by one click. Variables like the exposure time, that are different in the modi, are stored independently. In 'Solis', they would have to be changed back and forth.
- Expected and obtained measurement times and time usage are displayed.
- Cooling temperature is permanently monitored. Instable cooling results in a varying baseline (section 7.1). In 'Solis', a temperature rise was observed to be indicated only with a time delay of several minutes.
- The control of the external hardware is integrated into the LabVIEW program. For example, acousto-optical modulators are set according to the timings in the different acquisition modi (section 8.1). Automatic mirror holders are controlled to precisely position the excitation volume with respect to the center of the pixel ranges used (section 8.2).
- By programming a sequence of different acquisition types with different exposure times, it is possible to perform extended EMCCD-FCS series, as used for the measurements in part III of the thesis.

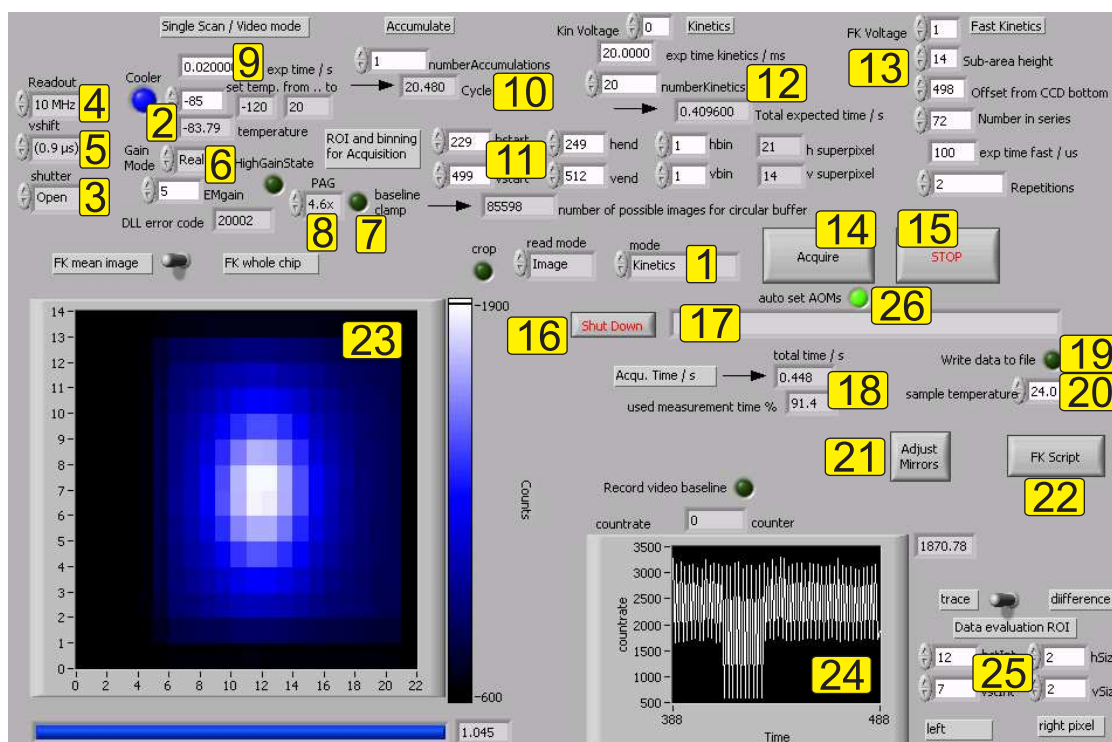


Figure 5.7.: EMCCD-FCS acquisition software: LabVIEW front panel, the user interface with controls and indicators.

1. Experiment type: single image, video mode, kinetic, fast kinetic.
2. Cooling temperature: possible range, set value, display of actual value.
3. CCD shutter control.
4. Readout frequency.
5. Vertical shift time.
6. EM-gain: gain-mode, set value.
7. Baseline clamp option.
8. Preamplifier gain.
9. Exposure time for single image and video mode (e.g. 20 ms, for alignment).
10. Display of calculated cycle time in kinetic mode.
11. Subregion and binning.
12. Kinetics settings: vertical shift voltage, exposure time, number of images, display of possible number of images storable in circular buffer of the camera, calculated total measurement time.
13. Fast kinetic settings: vertical shift voltage, number of subregion CCD rows, offset from chip bottom (typically set to chip height minus number of subregion CCD rows), number of exposures for both chips, number of fast kinetic series.
14. Start data acquisition.
15. Stop data acquisition.
16. Camera shut down with controlled temperature rise.
17. Status display: e.g. unstable temperature, wrong settings, shut down status.
18. Display of total measurement time and time usage.
19. Export data to binary file.
20. Sample temperature note.
21. Automated laser spot positioning (section 8.2).
22. Fast kinetic script for extended measurement series with different exposure times and automated spot adjustment in between.
23. Temporal averaged image.
24. Signal trace over time, summed from a pixel range define in 25.
25. Pixel range to evaluate the signal trace.
26. Option to automatically set the AOM trigger high times (section 8.1) according to the exposure time setting.

5.4. Matlab based graphical user interface data evaluation software

Acquired EMCCD image sequences were evaluated offline using a home-written Matlab program (MathWorks, Natick, Massachusetts). Matlab is a versatile software for numerical calculations of data stored in matrices (Matlab stands for MATrix LABoratory). Data sets in any format can be easily imported and processed with inbuilt algorithms and custom programmed functions. The results can be graphically represented in various plot formats and exported for the use in other programs.

Matlab is a text-based script software, but a convenient graphical user interface (GUI) can be created. The user can then repeatedly change values of variables and start different subroutines of the program. The GUI window (which features the evaluation of two-focus FCS data, see part III of this thesis) is shown and commented in fig. 5.8. The steps to process the data are the following:

1. Measurement data is loaded. The image, averaged over time, is displayed.
2. Background data is loaded (equivalent measurement with the CCD shutter closed). Background subtraction is performed to remove any fixed pattern, for example a different baseline of individual pixels.
3. Pixel range is chosen by marking a selection by mouse in the image or by typing in values. A subset range of the images of the stacks can be selected. Then, 'Go' is pressed to start data processing.
4. (Two additional corrections are performed for precise two-focus measurements, presented in part III, chapter 9, which are: 1. Enhanced baseline correction by using the left optically shielded CCD columns as reference even within the fast kinetic series. 2. Pixel-wise correction of the CCD non-linearity with light level.)
5. Signal from the pixel range is summed and averaged trace is displayed (average over 1000 images in the kinetics mode or average over the series on chip in the fast kinetic mode). This averaged trace over time serves as a check for instabilities, which can be excluded from data analysis by changing the stack subset range in (3.).
6. Signal trace is correlated by either using the Matlab inbuilt command 'xcov' (cross-covariance) and subsequent correlation data averaging on a logarithmic time scale, or by using a faster C++ based multiple-tau correlator routine (31).
7. (A third correction is done for precision two-focus measurements, the correction for the triangular averaging effect, explained in chapter 9.)
8. Correlation data can be exported to a text file and subsequently imported in Origin or Matlab (31) for curve fitting.

5.4. Matlab based graphical user interface data evaluation software

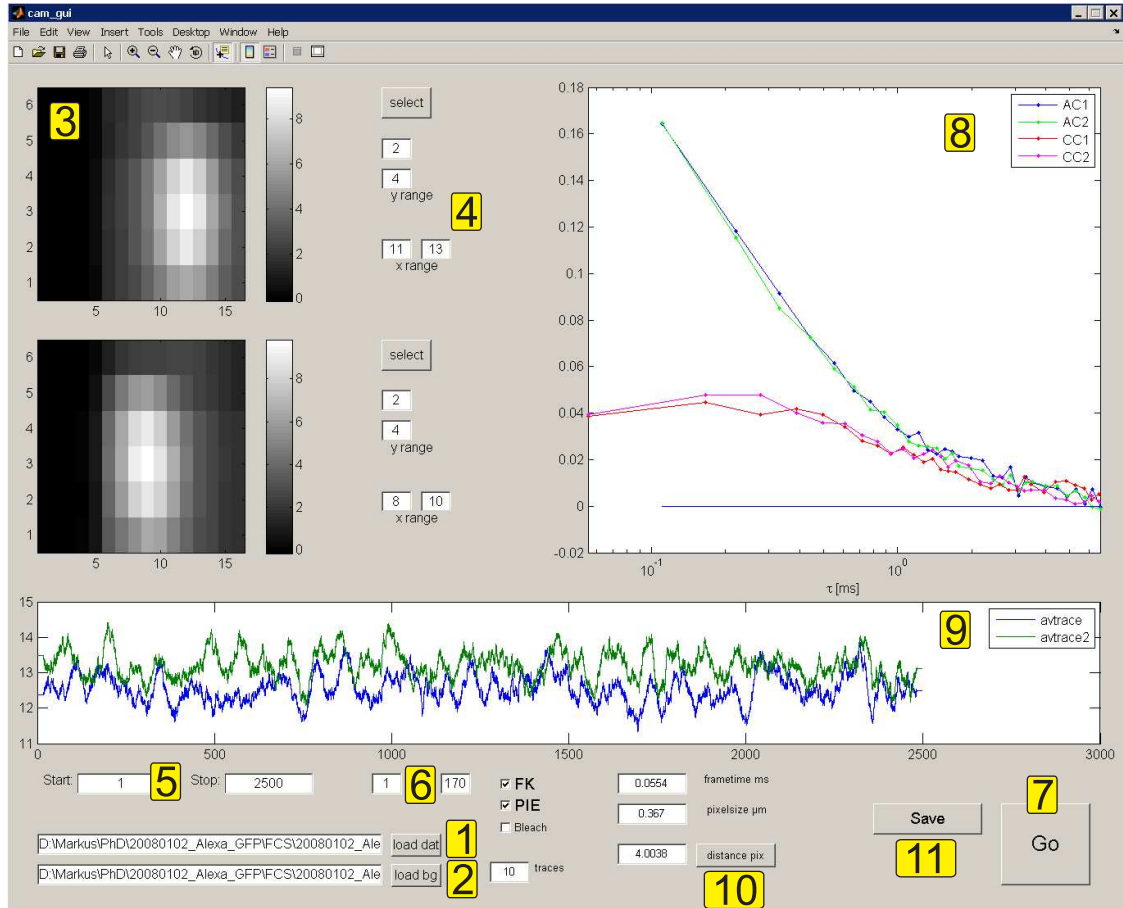


Figure 5.8.: EMCCD-FCS data evaluation software: Matlab GUI interface.

1. Load measurement data, the binary file exported in LabVIEW.
2. Load background data.
3. Average image (two images in case of two-focus FCS with alternating excitation).
4. Selection of pixel range, i.e. the 'pinhole' size, used to calculate the correlations for.
5. Option to limit the number of kinetic images or number of fast kinetic series, respectively.
6. Option to limit the number of exposures on chip for data from fast kinetic measurements.
7. Start correlation analysis.
8. Autocorrelation curve (two autocorrelation and two spatial cross-correlation curves in case of two-focus FCS).
9. Summed signal from pixel range over time to verify stable measurement conditions.
10. Calculation of distance between both spots in two-focus FCS (section 8.2).
11. Save correlation data to text file. Correlation data is then imported in Origin or Matlab (31) for curve fitting.

6. Comparison of EMCCD- and APD-based detection in FCS in solution

In this chapter, we summarize the results of EMCCD-FCS measurements in solution and compare the results to standard APD-FCS. We show that choosing different numbers of pixels for data evaluation corresponds to changing the pinhole size, which can be performed conveniently by software after the measurement. We further compare the fit results from combined fast kinetic and kinetic measurements for eGFP and the small organic dye Alexa Fluor 488.

CCD-pixels are the confocal pinhole

In the example of measurements for quantum dots in the kinetic mode (section 5.1), the signal trace was extracted from 2×2 pixels, which yielded a slightly bigger focal volume than that of the APD-detection with a $50\ \mu\text{m}$ diameter fiber. To demonstrate the influence of the pinhole size, we evaluated also the signal from 4×4 pixels, and from 1×1 pixels and 3×3 pixels from a second identical measurement with different lateral CCD position relative to the emission maximum (fig. 6.1).

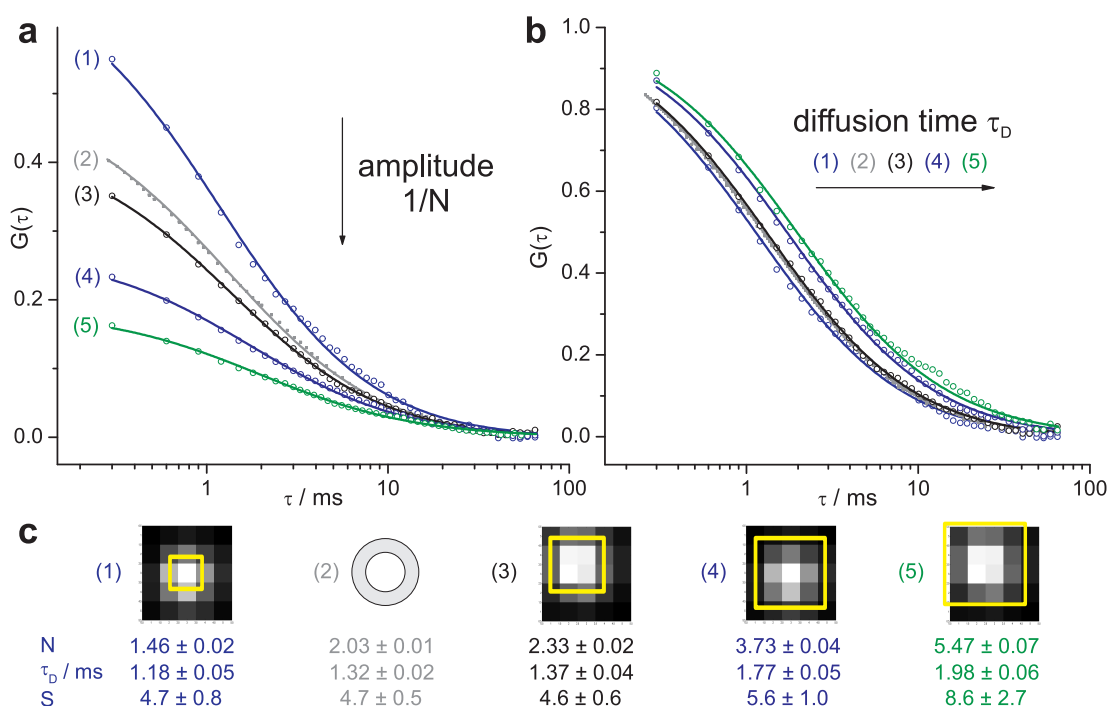


Figure 6.1.: Pixel-ranges determine the size of the confocal volume. **a:** Autocorrelation curves of quantum dots, evaluated with different pixel ranges as marked in (c), and the curve from APD-detection with a fiber of $50\ \mu\text{m}$ diameter (2) for comparison. **b:** Data from (a) normalized to $N=1$ for the fits. **c:** Fit results, showing an increase of all parameters for larger pinholes as expected.

The resulting autocorrelation curves and fit parameters show that larger pixel ranges yield bigger focal volumes, hence increased particle numbers and diffusion times. The structure parameter shows the expected trend to higher values for larger pinholes due to the less axial confinement of the focal volume. For the largest pixel range of 4×4 pixels, its relative error increases indicating that the Gaussian approximation does not describe the focal volume sufficiently any more. The APD-FCS curve with a $50 \mu\text{m}$ diameter fiber corresponds best to the EMCCD-FCS curve using 2×2 pixels ($48 \mu\text{m} \times 48 \mu\text{m}$).

Combined fast kinetic and kinetic measurements

If EMCCD-FCS is used to measure fast diffusion of commonly used fluorescent probes, the fast kinetic mode is employed. However, one measurement with a given exposure time in the fast kinetic mode gives only a part of the correlation curve, covering a time range from the cycle time to the product of cycle time and number of exposures per double chip. Additionally, measurement time usage decreases with shorter exposure times due to the constant time gap for chip readout (section 5.2).

To obtain reliable autocorrelation curves over several orders of magnitude of lag times, and to use the total measurement time efficiently, one therefore combines the results from several independent measurements with different exposure times. These can be several fast kinetic measurements (as used in part III of this thesis) or a combination of a fast kinetic and a kinetic measurement.

Results for measuring enhanced Green Fluorescent Protein (eGFP; Clontech, Mountain View, California) and Alexa Fluor 488 (Invitrogen, Karlsruhe, Germany) are given in fig. 6.2.

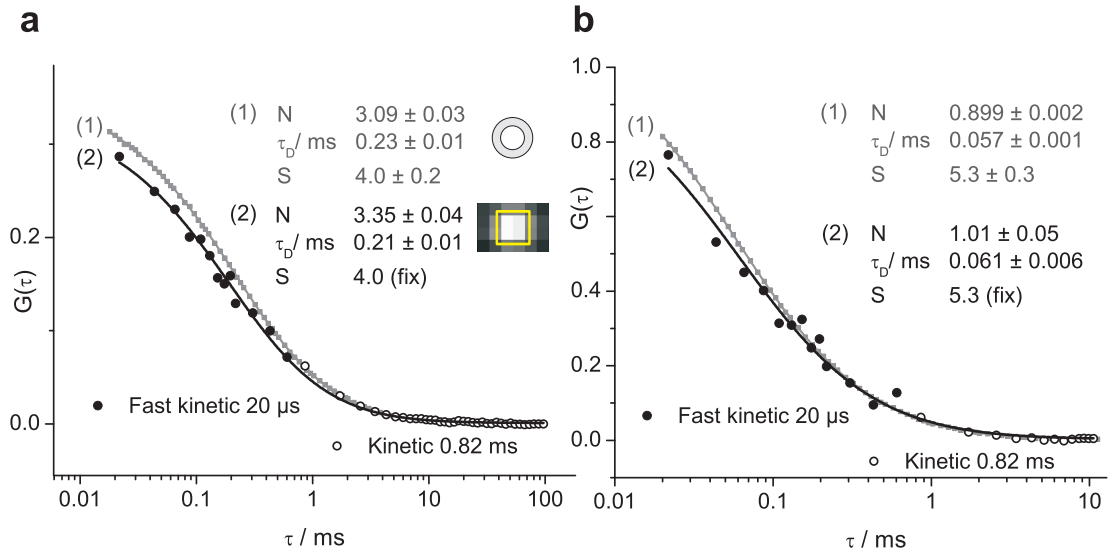


Figure 6.2.: Combined EMCCD-FCS curves from fast kinetic and kinetic acquisition. Autocorrelation curves of eGFP (a) and Alexa Fluor 488 (b). Fit results show good agreement to APD-FCS curves.

The autocorrelation curves consist of the data from a fast kinetic measurement ($20 \mu\text{s}$ exposure time, $21.8 \mu\text{s}$ cycle time, 40 exposures per chip, 1,000 series, 0.87 s effective and 26 s total measurement time) and a kinetic measurement (0.82 ms exposure time (at 3 MHz readout), 0.86 ms cycle time, 100,000 frames, 86 s total measurement time). In the data analysis, the structure parameter was fixed to the value obtained from APD-FCS measurements. The deduced particle numbers and diffusion times are in good agreement to the values obtained from APD detection.

7. Limits of the DV860 EMCCD model and prospects of the DU897 model

All EMCCD-FCS measurements presented so far were performed using the camera model iXon DV860. This camera was initially chosen for FCS because of its remarkable fast time resolution of 500 full frames per second (128×128 pixels image chip). For comparison, the camera model DU897 with the next bigger chip (512×512 pixels) exhibits a by factor 16 lower full frame rate and by factor 4 lower frame rate when using the same sized subregion of 128×128 pixels. The factor four is understandable since only unwanted rows can be binned and readout as one row whereas unwanted columns need to be still readout individually.

Despite the apparent advantage of using the model with the small number of pixels, we observed two limitations of this camera that made us decide using the model DU897 for all further FCS measurements presented in this thesis. The two properties, the baseline homogeneity across the chip and the clock induced charges, are discussed in the following for both camera models.

7.1. Baseline homogeneity across the chip and readout timings

As mentioned in section 5.2 for the camera model DV860, we had to reduce the readout frequency from 10 MHz to 3 MHz in the fast kinetic acquisition mode, since baseline inhomogeneities vertically across the chip were observed at 10 MHz readout frequency (fig. 7.1 a), which distorted the FCS curves. These repeated structures varied with acquisition parameter settings and they were not constant for different measurement days. According to the camera manufacturer, this problem was related to the readout process. It was recommended to use a reduced readout frequency of 3 MHz. At 3 MHz readout frequency, the baseline did not show any structure. For the camera model DU897, no structure was observed for all readout frequencies, hence 10 MHz readout frequency could be utilized. For two-focus FCS measurements, presented in part III of this thesis, we corrected for all baseline instabilities by using the reference signal from optically shielded columns of the chip (section 9.1).

In the fast kinetic mode, the readout frequency does not determine the time resolution but the usage of the total measurement time, which was introduced (fig. 5.4 d) as the ratio of effective measurement time (sum of all exposure times) and the total measurement time (including the chip readout) in a fast kinetic series. For the chip with 4×4 more pixels, the bigger vertical extension increases the number of exposures that can be stored on the chip by factor four, but the bigger vertical and horizontal extensions lead to a quadratically longer chip readout time by factor 16. This would result in a factor four less measurement time usage when using the model DU897 with the larger chip. However, since readout frequency was 10 MHz instead of 3 MHz, the readout time gap in between two fast kinetic series was decreased and measurement time usage was hence very similar for both camera models (fig. 7.1 b).

At similar measurement time usages, the bigger chip of the model DU897 had the advantage that individual fast kinetic series consisted of factor four more exposures stored on the double chip, and

7.1. Baseline homogeneity across the chip and readout timings

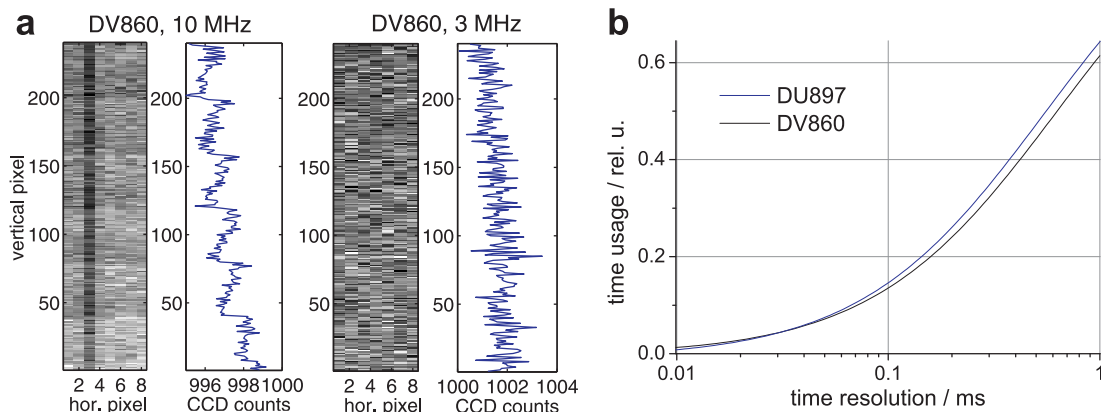


Figure 7.1.: Baseline structure at 10 MHz with the EMCCD model DV860. **a:** The EMCCD model DV860 exhibited a steplike baseline across the double chip in the fast kinetic acquisition mode (6 lines used for illumination, 20 μ s exposure time (no light, CCD shutter was closed), 21.8 μ s cycle time, 40 exposures per chip (hence 240 vertical pixels), temporal average from 1,000 fast kinetic series). The signal of the 8 horizontal pixels acquired was averaged to obtain the graphs next to the chip images. This effect was not present at 3 MHz readout frequency. The EMCCD model DU897 did not show this effect at all. **b:** The measurement time usages of the EMCCD models DU897 and DV860 were found to be very similar (DV860: 6 lines, 0.3 μ s line shift time, 40 exposures per chip, obtained chip readout time was 25 ms at 3 MHz readout frequency; DU897: 6 lines, 0.9 μ s line shift time, 170 exposures per chip, obtained chip readout time was 93 ms at 10 MHz readout frequency).

hence the time range of the correlation data was by factor four longer than the one when using the DV860 camera model.

As an unexpected drawback of the DU897 camera model, we observed strong cooling temperature fluctuations when trying to utilize the usual kinetic mode with a small subregion of 5×5 pixels and a minimal possible exposure time of 0.9 ms. After starting an extended kinetic series of several thousand exposures, the camera baseline decreased as a result of an increased cooling temperature. This increase of the cooling temperature could not be compensated by the thermoelectric cooling unit. According to the camera manufacturer, the short exposure times and predominant frame shift operations led to heat generation because of the ohmic resistance of the chip. The effect was only present at this camera model due to the bigger chip size and hence larger resistance, and due to the three-stage thermoelectric cooling (compared to a two-stage cooling at the DV860), which can achieve lower cooling temperatures but shows slower response.

However, as a substitute of the kinetic mode, we could utilize the fast kinetic mode. At exposure times corresponding to the ones used in the kinetic mode of the DV860 and DU897 camera models of 0.3 ms and 0.9 ms, the measurement time usages were around 0.3 and 0.6, respectively, so that an increase of the total measurement time of at most factor three compared to a continuous kinetic mode was not of much importance.

7.2. Clock induced charges (CICs)

Clock-induced charges (CICs) or spurious noise arise from the readout process of a CCD (section 3.3). When the photoelectrons are clocked off the chip pixel by pixel, there is a small probability that additional charges are created by impact ionization. These additional charges are present in all CCDs, but typically this form of dark signal is hidden by the readout noise or by the thermally generated charges. However, in EMCCDs, even single electrons are amplified above the read noise floor (by the same process of impact ionization in the gain register), hence all dark counts become visible.

Depending on the exposure time, thermally generated charges (electrons per pixel per second) or CICs (electrons per pixel per chip readout) can be the dominating source of dark signal. At sufficiently

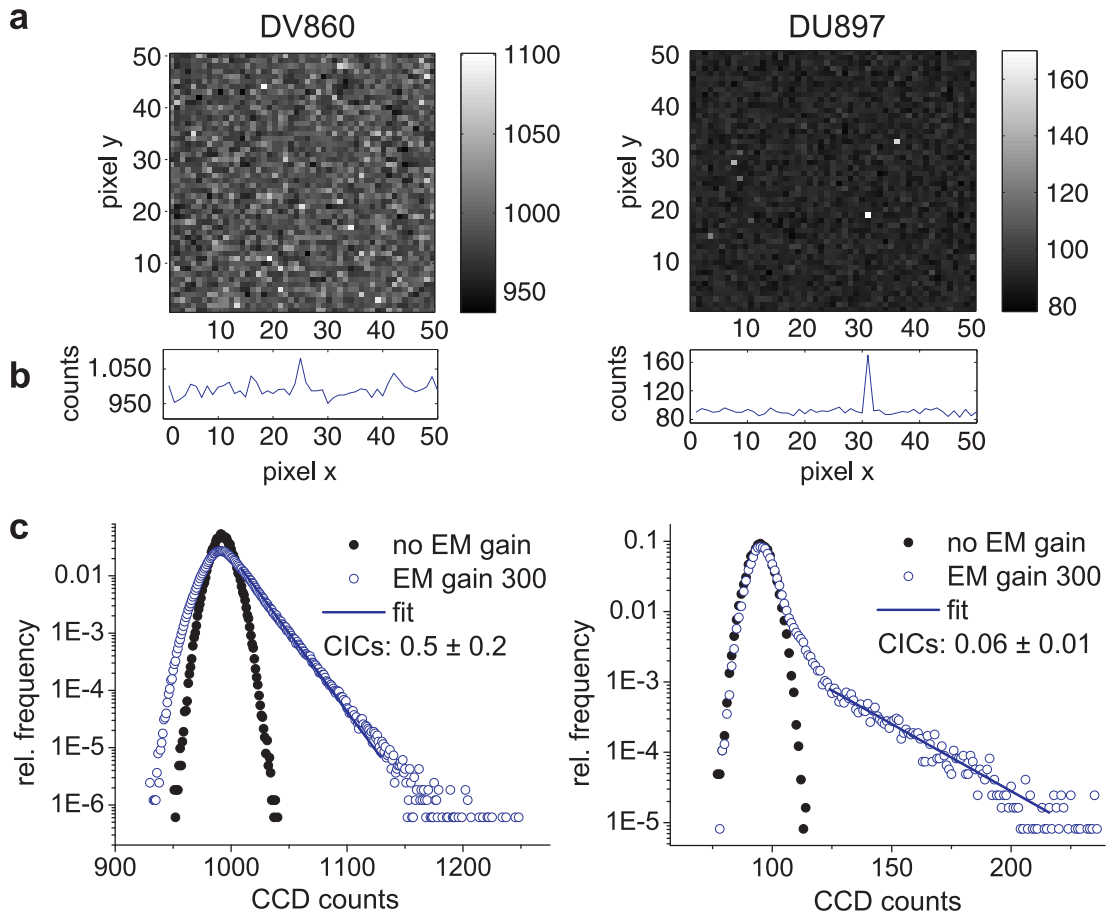


Figure 7.2.: CICs at the EMCCD models DV860 and DU897. Dark images (CCD shutter closed) with EM gain reveal the CIC characteristics of an EMCCD camera. Compared are the two EMCCD models: left column: DV860, and right column: DU897. **a:** Example dark image of 50×50 pixels. At the DU897, CICs are clearly visible as single bright pixels above the read noise floor. At the DV860, overall noise is too high to identify CICs in the image. **b:** Example plot of one horizontal line (line 21 at the DV860, and line 19 at the DU897). **c:** Relative frequency of CCD counts from repeated measurements (several hundred thousand pixels). Baseline (991 and 95 counts), readout noise (8.4 and 4.4 counts root mean squared, corresponding to 164 and 55 electrons at conversion factors of 19.9 and 12.4 electrons per count), and CIC level (0.5 and 0.06) can be deduced from the histograms, for the DV860 and DU897, respectively. Fit lines for CIC determination are according to equation 3.3 in section 3.3.

7.2. Clock induced charges (CICs)

low cooling temperature (-70 to -100 °C for most EMCCDs), classical thermally generated dark counts are specified to be on the order of 0.001 to 0.02 electrons per pixel per second. CIC levels are given, in case they are specified at all, on the order of 0.005 to 0.02 electrons per pixel *per chip readout*. At short exposure times and rapid frame rates of more than 1000 readouts per second, as for example employed in EMCCD-based FCS, the influence of the thermally generated dark counts becomes negligible, but the CICs are most important.

The CIC characteristics of a EMCCD camera can be easily visualized and quantified by acquiring a series of dark images and analysis of the histogram of CCD count signal output values (fig. 7.2). The CIC level of the two EMCCD models DV860 and DU897 were found to be different. The model DV860, initially used for FCS, exhibited a by one order of magnitude higher CIC level than the DU897 (0.5 vs. 0.06 electrons per pixel per readout, respectively). The readout noise was also higher for the DV860 model (164 vs. 55 electrons), which was in accordance with the specifications of the camera models.

The total CIC background level per second depends on the exposure time used in EMCCD-FCS. When using, for example, 50 μ s exposure time in the fast kinetic mode, then 0.06 CICs per pixel and readout will result in 1200 CICs per second - and when using the summed signal from 3x3 pixels, this results in 11 kHz CIC dark counts. For comparison, our standard APDs have a dark count signal of only 0.2 kHz. The CICs yield an uncorrelated background, which can be easily subtracted, but background noise in general decreases the signal to noise ratio of the correlation curve (19). This is especially important for the shortest exposure times, where effective measurement time usage and the signal level are very low already.

CICs can be considered as one fundamental detection limit of EMCCD technology when aiming for fast time resolution. For our FCS measurements, we typically employed slightly higher fluorophore concentration than used in APD based FCS, as mentioned before in section 5.2. This assured a better ratio of light signal to CIC background. We also tested another EMCCD of the same model DU897, which exhibited a higher CIC level due to a higher vertical shift voltage (setting +2) required for proper charge transfer efficiency. For both DU897 cameras, CIC levels were about one order of magnitude lower in the kinetic mode than in the fast kinetic mode. The value specified by the manufacturer referred to this lower one in the kinetic mode (0.005 electrons per pixel per readout). No difference of the CIC level in kinetic and fast kinetic mode was observed at the DV860 in contrast. According to the camera manufacturer, CIC level is optimized for each type of chip by employing appropriate readout patterns (shift times and voltages). However, among the few different electron multiplying chips, available from mainly two companies, there are clear differences in CIC characteristics, and the chip used in the DU897 is the best currently on the market.

Due to the lower CICs, and the uniform baseline across the chip, compared to the model DV860, we utilized the model DU897 for further FCS measurements presented in this thesis.

Conclusion of part II

In this part of the thesis, we have demonstrated initial FCS measurements with an EMCCD camera. This is an important technical step towards parallel detection with a two-dimensional array detector.

The full frame readout time resolution of 2 ms of the EMCCD model DV860 can be enhanced to 300 μ s in the quasi-continuous kinetic acquisition mode by choosing a small subregion of the chip. The time resolution is further enhanced to 20 μ s by repetitive starting a fast kinetic measurement, where only several top lines of the chip are illuminated and most of the chip is used to store the charge. The minimal sensible exposure time in this mode is only determined by the number of used CCD lines and the vertical shift speed. The comparably slow chip readout process after the rapid exposure series leads to the main drawback of this mode: the non-continuous data acquisition with increased total measurement times.

However, regardless of the limited readout speed, this demonstrates the ability of an EMCCD-camera detector to perform FCS on timescales interesting for biological applications.

We have discussed the acquisition timings and dark signal characteristics of two different EMCCD camera models. For these two specific models, the DU897 camera model with the larger number of pixels exhibits the overall better performance.

Part III.

Two-focus FCS with EMCCD detection

Two-focus FCS with EMCCD detection

Experiments presented in this part were performed in collaboration with Dr. Jonas Ries.

In this part of the thesis, we demonstrate two-focus FCS with the EMCCD-based spatial resolved detection. Two-focus FCS is a direction-sensitive extension to standard one-focus FCS (section 2.4.2), which was introduced to measure flow characteristics in microstructured channels (40). There is also a great potential of direction-sensitive FCS for the investigation of cellular processes, although measurements of transport phenomena in living cells by FCS have remained scarce (82).

Recently, two-focus FCS was recovered as a method to enhance the precision of FCS measurements (15, 47). This is because two-focus FCS does not solely rely on the calibration of the detection volume size, but parameter estimates mostly depend on the distance between both focal volumes (section 2.4.2). The distance, however, can be determined independently and is fixed, even if measurement conditions change from sample to sample, making two-focus FCS very robust against most artefacts present in one-focus FCS (15, 30, 35).

In chapters 8 and 9, we complement the spatially resolved detection by a very flexible two-focus excitation method, and we refine the EMCCD data analysis. In chapter 10, we determine diffusion coefficients of several fluorophores showing a good agreement with recently published results from two-focus FCS based on APD detection. Furthermore, we apply two-focus FCS to flow systems in microfluidic channels.

8. Two-focus excitation and detection

There are two experimental requirements needed to perform two-focus FCS measurements. First, two equally sized, laterally offset excitation volumes need to be created in the sample. And second, the fluorescence signal from the two foci has to be detected and assigned to the corresponding focal volume.

The two-focus detection is easily realized with the spatially resolved camera detection. Conveniently, both focal volumes are positioned along the horizontal direction of the camera, since the number of horizontal pixels used for data acquisition does not influence the speed of the camera. The detection settings and the distance determination are described in section 8.2.

The two-focus excitation is explained in section 8.1. It is based on splitting the laser beam and coupling the two collimated laser beams into the back aperture of the objective lens at a slightly different angle. Furthermore, alternating excitation is employed, as it is of key importance to avoid spatial cross-talk (section 2.4.2).

8.1. Fast alternating two-focus excitation

For two-focus excitation, we utilized a 488-nm laser line (Sapphire 488-20, Coherent) for measurement of fluorophores in the green spectral range (Alexa Fluor 488, Rhodamin 6G, eGFP), and a 633-nm laser line (25-LHP-991-230, Melles Griot, Bensheim, Germany) for measurements of fluorophores in the red spectral range (Atto 655, DiD), together with appropriate filter sets (LP 505 and HQ 535/70M; and LP 645 and HQ 703/95M, both AHF, Tübingen, Germany), respectively.

The laser beam was split by a beam splitter cube or by a pellicle beam splitter (Thorlabs Europe, Karlsfeld, Germany), and the two beams were reunited again by a second beam splitter, so that they entered the objective back focal plane at a slightly different angle (fig. 8.1). The angle difference determines the distance of the two foci in the sample, which is the key parameter in two-focus FCS.

To assure a highly stable setup and still a flexible choice of distances, we fixed the EMCCD to the optical table in the correct axial position of the secondary image plane, and we utilized motorized mirror mounts (piezoelectric drive, model 8816, New Focus, Santa Clara, CA, USA) to change the angle of the excitation lasers before coupled into the objective (fig. 8.1 a) with high precision. The maximum angle difference of both lasers was 0.04° , corresponding to a separation of the two foci of $1.8\text{ }\mu\text{m}$ in the sample. The distance between the motorized mirrors and the objective lens was about 200 mm, therefore the position change of the beams entering the back focal plane of the objective was at most 0.1 mm and hence negligible.

In order to allow for a quantitative description of the correlation curves with the model functions given in section 2.4.2, spatial cross-talk between the two laterally overlapping detection volumes has to be avoided. This can be easily accomplished by using alternating excitation of the two lasers and by only detecting the signal in the corresponding detection channel.

As fast switches, we utilized two acousto optical modulators (AOM, EQ Photonics, model number 3350-192, rise time of 7 ns). The trigger output of the EMCCD was fed into a fast timer-counter-board (National Instruments, model number PCI-6602), providing trigger high and low times for the AOMs.

8. Two-focus excitation and detection

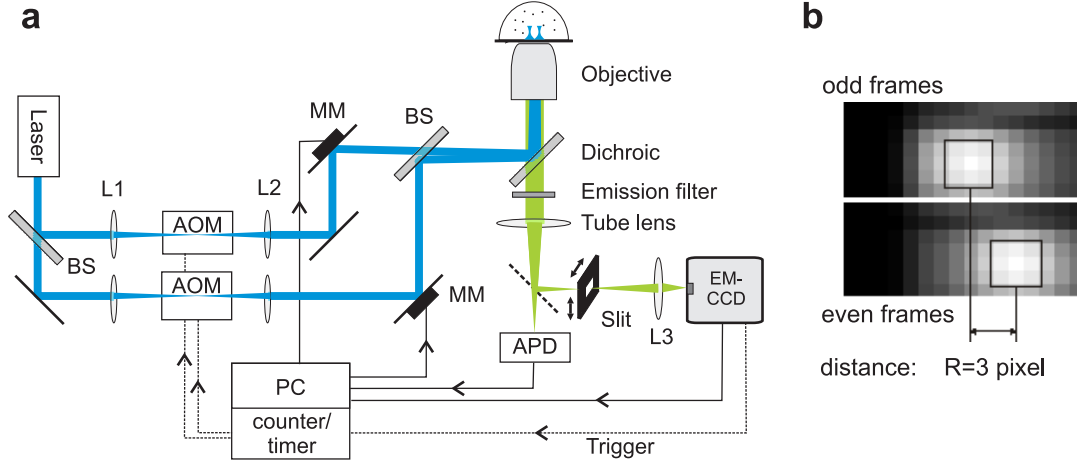


Figure 8.1.: Two-focus EMCCD-FCS setup. **a:** The laser beam is split by a beam splitter (BS). Beams are focused by lens telescopes (lenses L1 and L2) through acousto optical modulators (AOM), that serve as fast switches for alternating excitation. Computer controlled motorized mirrors (MM) allow for automatic and accurate alignment to couple both beams into the objective back focal plane at a slightly different angle. **b:** Temporal average of odd and even frames, respectively, corresponding to focus 1 and 2 with a distance of for example 3 pixels on the EMCCD or 1.1 μm in the sample. Left four CCD columns were optically shielded as baseline reference (section 9.1).

The lens pairs in the telescopes focusing the beams through the AOMs could be changed (focal lengths of 50 mm–200 mm), to obtain different laser beam diameters. Typical, we largely underfilled the back aperture of the objective. The resulting bigger focal volumes were convenient for EMCCD-FCS to obtain longer diffusion times and more sensitivity to small flow speeds (section 10.3).

8.2. Two-focus detection and automated distance adjustment

For all experiments in this part of the thesis, we utilized the camera model DU897 due to its better overall performance (chapter 7). Compared to the measurements with the model DV860, shown in part II, the pixels had a smaller size of $16\text{ }\mu\text{m} \times 16\text{ }\mu\text{m}$. The camera was solely operated in the fast kinetic acquisition mode, using different exposure times to cover a large range of correlation times.

A readout frequency of 10 MHz could be utilized for all measurements. Vertical shift time was longer ($0.9\text{ }\mu\text{s}$ per line compared to $0.3\text{ }\mu\text{s}$ for the DV860 model), and vertical clock voltage was increased to the setting +1 to achieve good charge transfer efficiency. A similar electron multiplying gain of factor 300 and a maximum preamplifier gain setting $\times 4.8$ were used. Conversion factor was 12 electrons per digital count. Thermoelectric cooling was set to the minimal possible value of -85°C .

In the detection pathway, the simple razor blade was substituted by a four-side adjustable slit (SP60, Owis, Staufen, Germany) to also mask a horizontal part of the chip (section 9.1). The lens mapping the primary image (initially 1:1) onto the EMCCD ($f = 50\text{ mm}$) was shifted as much as possible in the setup (by 20 mm) towards the EMCCD to demagnify the primary image by 1:0.71. This was done in order to use as few pixels as possible for data evaluation, to allow for as many as possible exposures per double chip in the fast kinetic mode. A higher degree of demagnification would require to use a lens with bigger focal length, but this would impractically extend the overall length of the detection path.

8.2. Two-focus detection and automated distance adjustment

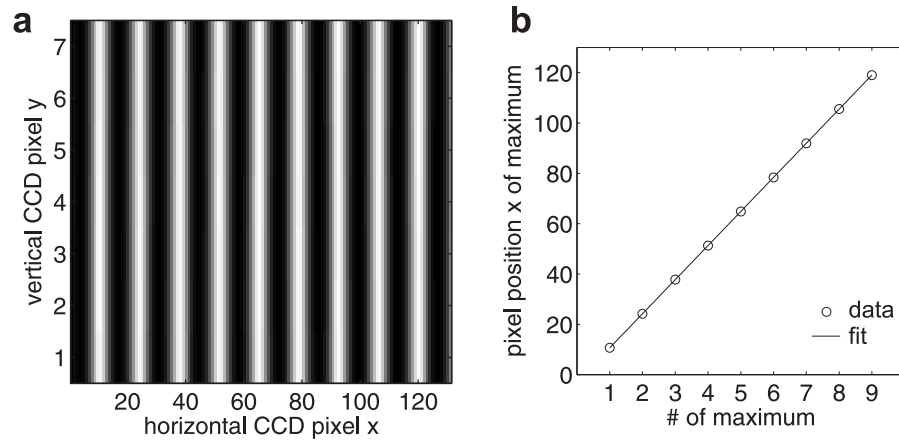


Figure 8.2.: Determination of the pixel size in the object space. **a:** Image of a calibration slide with 200 line pairs per mm. **b:** Pixel position vs. number of maxima (the bright lines). The slope of the linear fit is 13.6 pixels/line pair and a pixel size in object space of $(0.367 \pm 0.001) \mu\text{m}$ is deduced.

The distance between the two foci was determined by imaging a microscopic ruling (Ronchi Ruling Slide 200 line pairs/mm, Edmund Optics, Karlsruhe, Germany). From the image, we could determine the length of a pixel (fig. 8.2), projected back to the object space. The line pair (lp) frequency was verified by measuring the first order diffraction of a laser to $(201 \pm 1) \text{ lp/mm}$. The positions of the maximum intensities in a horizontal cross-section of the image (fig. 8.2 a) were determined by an individual second order polynomial fit around each maximum. These pixel positions were plot over the number of maximums (fig. 8.2 b) and a pixel size of $(0.367 \pm 0.001) \mu\text{m}$ was determined from the slope of the linear fit to this curve.

The focal volumes were automatically aligned on the center of a pixel or on 2×2 pixels, so that

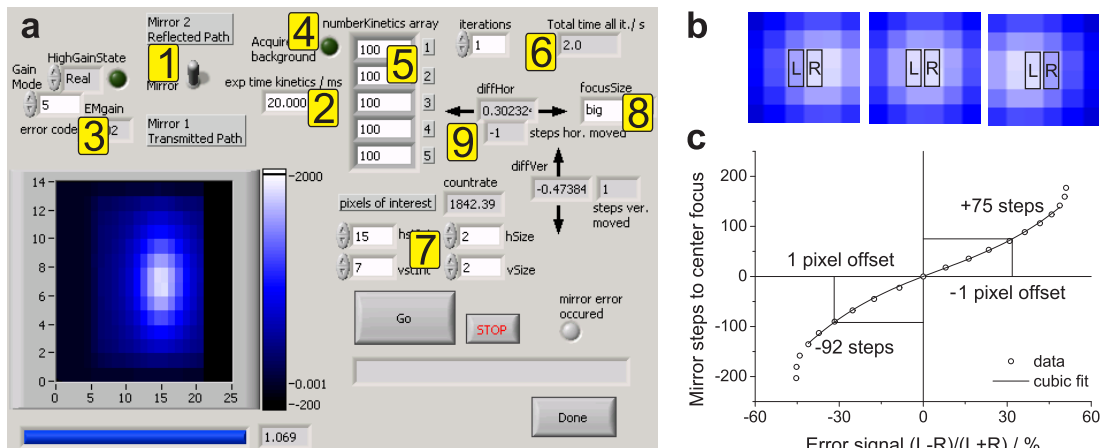


Figure 8.3.: Automated focus adjust program. **a:** LabVIEW user interface with controls of (1) beam selection, (2) exposure time, (3) EM-gain, (4) background acquisition, (5) iteration array of stack sizes, (6) calculated total time for all iterations, (7) Pixel range, (8) focus size, (9) offset error value and resulting steps that were moved to re-center the focal spot. **b:** Horizontal offset of, for example, one pixel to the right or left of the selected 2×2 pixel range. **c:** Calculation of the error signal $x = (L - R)/(L + R)$ and the correction function to re-center the focus, approximated by a cubic function.

8. Two-focus excitation and detection

the distances between both foci were integer multiples of the pixel length (for example 3 pixels in fig. 8.1 b). The alignment during data acquisition was performed via a LabVIEW subroutine (fig. 8.3 a shows the front panel of the ‘focus adjust’ program). Long exposure times (e.g. 20 ms) in the kinetic acquisition mode were employed to obtain a high signal to noise ratio in the alignment process. We used the brightness difference of pixels within or around a given pixel range as offset measure (fig. 8.3 b shows an example of a horizontal offset). Correction functions were determined empirically that related these offset error values (x) to the steps of the motorized mirror needed to center the focal spot again (fig. 8.3 c).

The different correction curves (two mirrors, two axes, different focal volume sizes employed) could be well approximated by cubic functions in the range of about one pixel offset. For a coarse adjustment of more than one pixel offset, one would manually change the angles of the mirrors. In the example in fig. 8.3 c, we obtained:

$$\text{steps}(x) = 0.00045 x^3 - 0.0083 x^2 + 2.2 x. \quad (8.1)$$

The linear term dominates, assuring that the mirror angle changes in the right direction. Typically, several iterations were necessary, so that one could start with short measurements with a few number of exposures in the kinetic measurement mode and end with an extended number of stacks for precise alignment. The resolution of the alignment was around two steps. One piezoelectric step of the mirror corresponded to a displacement of the focal spot of ≈ 5 nm in the sample.

After the measurement, the actual distance could be evaluated directly from the data acquired for FCS by fitting the average odd and even images individually with a Gaussian function (fig. 8.4). We estimated the reproducibility and accuracy of the distance determination between the foci to be below 2%, the determination of the pixel size with the grid was better than 1%. The accuracy of the distance can therefore be assumed to be better than 3%.

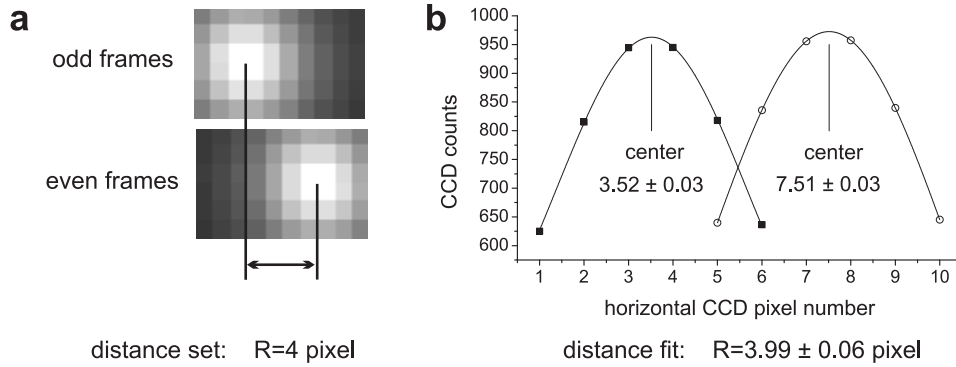


Figure 8.4.: Distance fit. Fit of the horizontal cross-sections of the temporal average images from odd and even frames (a), respectively, for a fast kinetic measurement with 100 μ s exposure and 1000 series. The obtained distance from fitting the acquired data (b), used for FCS analysis, of $R = 3.99 \pm 0.06$ pixels corresponds very well to the intended value of 4 pixels, which was set during data acquisition by the focus adjust program in this example.

To perform extended measurement series in the fast kinetic mode with different exposure times, we wrote a LabVIEW script, where different types of measurements (fast kinetic signal and background) and focal spot alignment routines could be performed automatically. Data evaluation was accordingly automatically processed by a Matlab script.

9. Refined EMCCD data processing

In part II, a qualitative agreement between the EMCCD-FCS and APD-FCS autocorrelation curves was shown. When performing two-focus FCS measurements, as presented in this part of the thesis, however, one aims for achieving precise, absolute values of diffusion coefficients. We therefore performed multiple fast kinetic series to increase the effective measurement time, to obtain average autocorrelation and spatial cross-correlation curves with sufficient signal to noise ratio (measurement results are presented in chapter 10). In turn, due to the extended measurements, we noticed that autocorrelation and cross-correlation curve parts from measurements with different exposure times did not overlap perfectly, but showed a systematic offset.

In addition to the simple background subtraction (section 5.2), we found three more corrections necessary in the data evaluation process. Two of them are related to technical properties of the EMCCD signal, concerning the baseline stability and the linearity with respect to the light level. The third correction is related to the mathematics of correlation analysis. It becomes important, when the exposure time in EMCCD-based FCS (the bin time of the fluorescence signal) is not any more small but comparable to the diffusion time.

9.1. Enhanced baseline correction

The baseline of a CCD camera is the average level of digital count values in an acquired image, when there is no light falling onto the detector. This might be called a background image, but it is not a real background originating from photoelectrons. Rather, the baseline is an electronic offset of the digitizer, which can be set by the camera manufacturer. It has to be higher than the Gaussian readout noise to always assure positive CCD count values. On the other hand, it should be as low as possible not to decrease the usable dynamic range of the digitizer (for example 14 bit). Typical values for our two EMCCD cameras were given in fig. 7.2.

Although the absolute value of the baseline is not important, baseline stability in a series of acquisitions has been a challenge in CCD technology (121). Small heat generation caused by the voltages applied to the chip in normal operation results in baseline drifts. In good cameras, drifts can be corrected for on hardware level. In our Andor EMCCDs, this is the user selectable function called baseline clamp, already mentioned in section 5.1.

This inbuilt baseline correction is performed once per chip readout, using the signal from one or several optically shielded reference rows, typically below the image or storage chip (fig. 9.1 a). It is intended for and works well to correct for baseline drifts between frames in a kinetic series. However, in the fast kinetic mode, where image series are stored on the double-chip, the baseline clamp feature can not detect the vertical baseline variations. We therefore deselected the baseline clamp option and created our own baseline correction, by masking several columns on the chip (fig. 9.1 a).

This allows to monitor all baseline variations, within one fast kinetic series and between the repeated fast kinetic exposure series. An example of the baseline variation in one fast kinetic measurement series with 146 exposures per chip and 2500 repetitions is shown in fig. 9.1 b. The varying

9. Refined EMCCD data processing

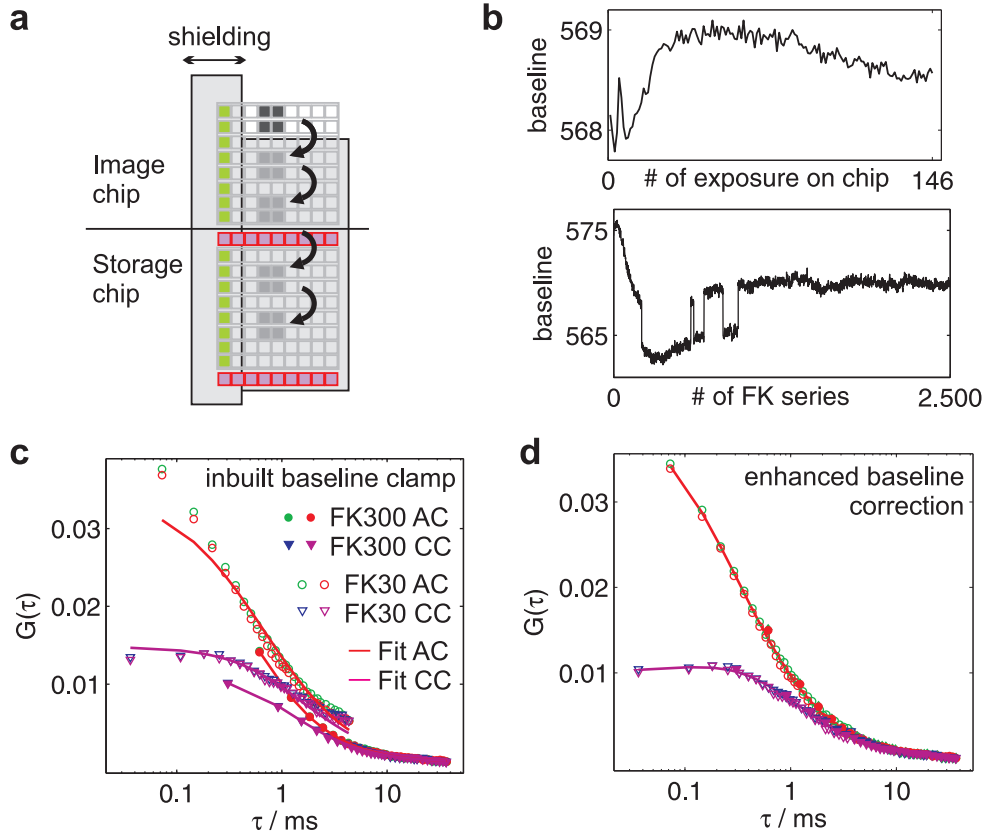


Figure 9.1.: Baseline correction in the fast kinetic mode. **a:** Reference columns on the chip, optically shielded with a mask (fig. 8.1), serve as our own baseline correction in the fast kinetic mode (the signal of the pixels marked in green; as opposed to the inbuilt baseline clamp function, which uses the reference signal from shielded CCD lines below the image or storage chip, marked in purple). **b:** Average baseline variations across the chip and between repeated fast kinetic series. **c:** When the inbuilt baseline clamp function is used, the FCS curve parts from a fast kinetic measurement with exposure time 30 μ s are offset from the one with 300 μ s. **d:** No offset is obtained with the enhanced baseline correction. Auto- and cross-correlation data are from a measurement of Atto 655 dye, explained in fig. 10.1.

baseline across the chip cannot be corrected by the standard inbuilt baseline clamp function. Therefore, subtraction of the baseline from the real signal will be incorrect, and this leads to a wrong normalization of the correlation curves. A wrong normalization can be apparent in a wrong amplitude of the correlation curve, for short curve parts seen as vertical offsets (fig. 9.1 c). The error will be highest for the fast kinetic series with the shortest exposure time and hence the lowest signal level. Using the enhanced baseline correction yields a good overlap (fig. 9.1 d).

9.2. CCD nonlinearity correction

Another property of the CCD can influence the overlap of the different FCS curve parts, a non-linearity of the output CCD signal with respect to the input photon level. We measured this property by exposing the CCD for different time durations to the fluorescence light in our usual confocal setup (fig. 9.2 a). A small non-linearity was obtained, which could be approximated by a power function $y = ax^b$

with exponent $b = 1.055 \pm 0.002$. Power functions are often used to describe CCD characteristics, and the exponent is typically called gamma factor. The factor a accounts for the arbitrary scale of light level (in our case the illumination time period, which is proportional to the accumulated light level on the EMCCD), the electron multiplication and the conversion from electrons to CCD counts. It is not important in FCS analysis since it cancels out in the definition of the normalized correlation function (equation 2.11).

The obtained power function can be utilized to correct the CCD count signal in an FCS measurement. This is performed pixel-wise and it requires in particular the correct subtraction of the baseline before (section 9.1). The small effect of the correction for the CCD nonlinearity can be seen when zooming in the overlap region of the two FCS curve parts (fig. 9.2 b). The correction shifts the first data points of the FK300 measurement towards the fit curve. The fit was performed after all corrections, hence the fit curve serves as good reference. Without correction, data point of the FK300 curves

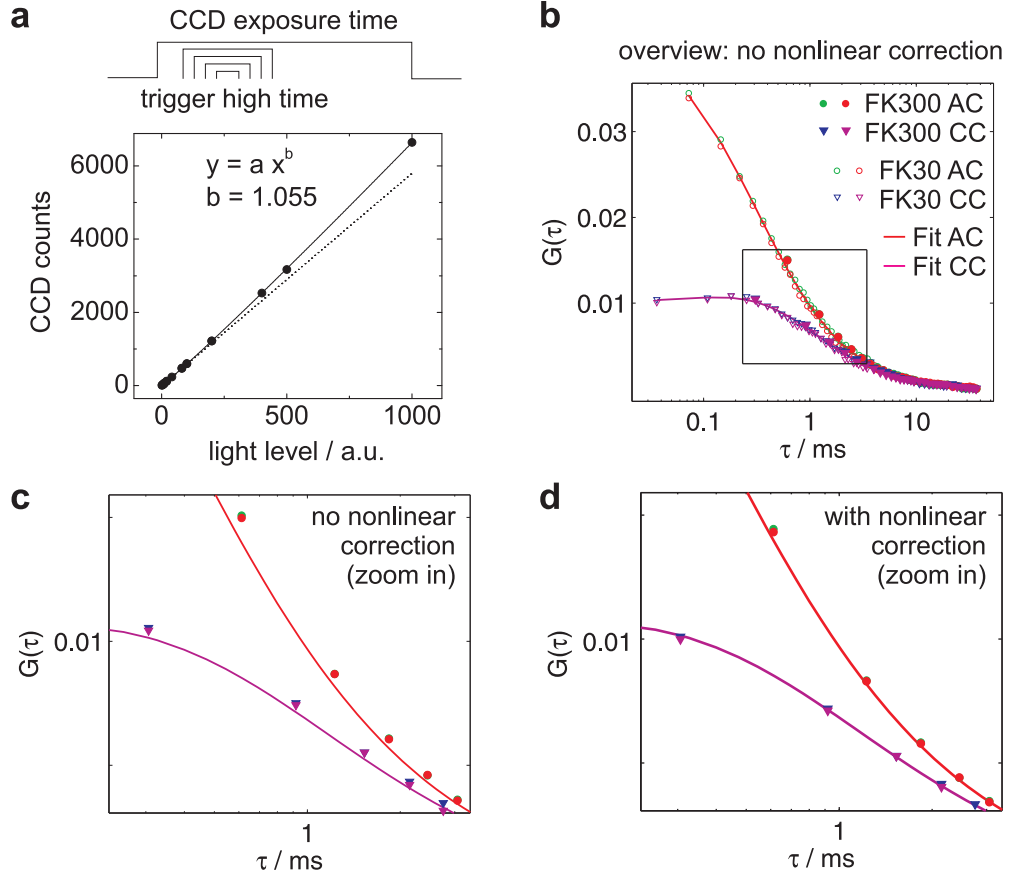


Figure 9.2.: CCD nonlinearity. **a:** In a constant exposure time, the accumulated light level on the EMCCD is varied by illumination with different time periods. The time periods are set by sending trigger high times to the AOMs (fig. 8.1 a) of different duration. The EMCCD output counts are slightly non-linear with the input light level. The dependency can be approximated by a power function with exponent 1.055 ± 0.002 . A linear function (dotted line) is shown for comparison. **b:** Same data as in fig. 9.1 d, but with a rectangle indicating the zoom range used in (c) and (d). **c:** If not corrected for, the nonlinearity of the EMCCD results in small offsets in the overlap region between the two fast kinetic series with exposure times $30 \mu\text{s}$ (FK30) and $300 \mu\text{s}$ (FK300) (zoomed part of the data in (b) with data points from fast kinetic series FK30 omitted for clarity). **d:** Employing the nonlinear correction yields a better overlap.

exhibit a small positive offset (fig. 9.2 c). When accounting for the non-linearity of the CCD signal, data points are corrected by approximately 4% and better match with the fit curve (fig. 9.2 d).

9.3. Correction for triangular averaging in correlation analysis

Yet a third correction can be applied, the correction for the triangular averaging effect in correlation analysis. This correction is even smaller than the correction for the nonlinearity of the camera, and it mainly affects the first data point (by approximately 2% in our example).

The triangular averaging effect arises by reason of the finite bin width of the intensity trace obtained from the EMCCD acquisition (31). We can for example look at the first data point of the autocorrelation function (fig. 9.3 a). If exposure time is T , then the first point of the correlation function is $G(T)$. The bin width T , however, can be considered as a sum of smaller bins, for example with a width

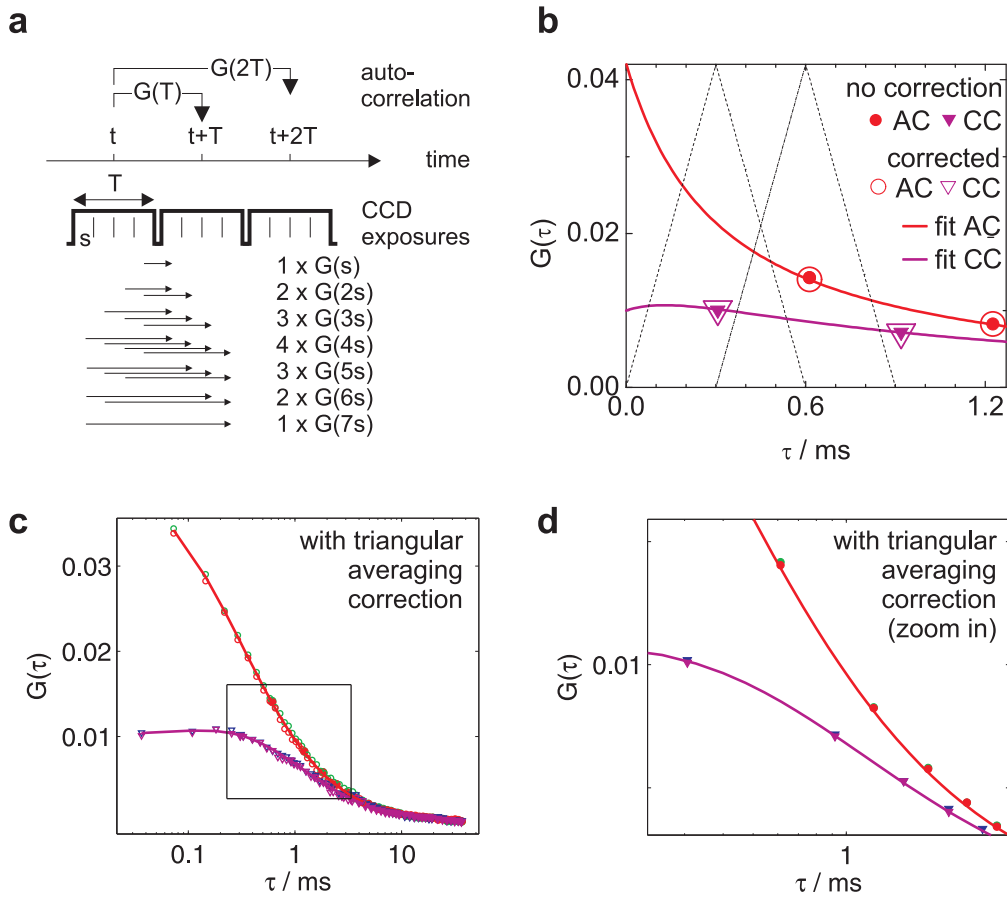


Figure 9.3.: Triangular averaging effect. **a:** Due to the finite bin time T in data acquisition by a CCD, the correlation $G(\tau)$ represents a weighted average from correlations with shorter and longer lag times. For example, $G(T)$ contains correlations from $G(0)$ to $G(2T)$. **b:** The effect can be visualized when plotting the triangular weighting functions together with the correlation curves linear over time. Open symbols denote the data points that were already corrected for the triangular averaging affect. Correction factors were around 2% only. **c and d:** A perfect overlap is achieved when applying all three corrections discussed in this chapter.

9.3. Correction for triangular averaging in correlation analysis

$s = T/4$. The correlation $G(T)$ is hence a weighted average of correlations with lag times τ ranging from s to $2T - s$, and the weighting factors are a triangular function with maximum at $\tau = T = 4s$.

If the true correlation function (calculated from small bins, or the model function) $g(\tau)$ is known, then the effect of the triangular averaging can be calculated for any lag time by integration:

$$G(\tau) = \frac{1}{T^2} \int_{-T}^T dt (T - |t|) g(\tau + t). \quad (9.1)$$

The resulting average value $G(\tau)$ consists of the dominating component $g(\tau)$, but also contributions from smaller lag times ranging down to $g(\tau - T)$ and larger lag times ranging up to $g(\tau + T)$ are represented. The magnitude of this effect can be visualized, if we plot the correlation curve on linear rather than logarithmic time scale (fig. 9.3 b).

The triangular function can be plotted together with the correlation functions, for example at the first point of the auto- and cross-correlation data from the exposure series of 300 μ s with alternating excitation. The triangular averaging effect depends on the bin width T and on the curvature of the correlation curve at τ . At the data points in fig. 9.3 b, the triangular averaging will shift the point on the convex autocorrelation function upwards (by 2%), and it will shift the point on the concave cross-correlation function downwards (by 1%).

In turn, the triangular averaging effect can be removed from the experimental data by correcting back using these factors. The correction is small, and hence almost no difference can be seen in the corrected data (fig. 9.3 d), compared to the data where only the CCD nonlinearity was corrected for (fig. 9.2 d). However, the triangular averaging effect can be easily higher. When using, for example, an exposure time of 0.9 ms and no alternating excitation, the correction factor of the first autocorrelation data point would be 12%.

To summarize chapter 9, for our measurements, the correct background subtraction by using the shielded CCD columns in the fast kinetic mode was most important to obtain good, overlapping FCS curves parts from series with different exposure times. The other two corrections were of minor importance. However, they should be still applied since they introduce systematic offsets. With all corrections, a virtually perfect overlap of the curves from measurements with different exposure times was obtained (fig. 9.3 c-d).

10. Precise determination of diffusion coefficients and flow speeds

In this chapter, we present EMCCD-based two-focus FCS measurement results. We first measure diffusion coefficients in solution of the organic fluorophores Atto 655, Alexa 488, Rh6G, and the fluorescent protein eGFP. The value for Atto 655 was recently precisely determined by APD-based two-focus FCS (15), and it can hence serve as a reliable reference. EMCCD-based two-focus FCS is furthermore well suited for measurements on membranes, where diffusion is more than two orders of magnitude slower than in solution. As an example, we measure the fluorophore DiD in a supported DOPC bilayer.

Since EMCCD-FCS allows for changing the pinhole size, we investigate the influence of differently sized individual pinholes for both foci, compared to one big pinhole for both, as throughout employed in APD-based two-focus FCS in the literature (15, 29, 30, 45, 46, 83).

Furthermore, we apply two-focus FCS to flow systems in microfluidic channels. Here, we investigate the range of flow velocities that can be measured when utilizing small organic fluorophores.

10.1. Diffusion measurements in solution and on membranes

We first measured the diffusion coefficient of Atto 655-NHS ester in solution. Fig. 10.1 shows the correlation curves for three different distances between the two foci of 0.58 μm , 0.87 μm and 1.14 μm , corresponding to 2, 3 or 4 pixels on the EMCCD (pixel size in sample space was 0.289 μm in this experiment). The correlation curves are averages in the fast kinetic mode of 10 runs with time resolution of 30 μs (total effective measurement time 2 min, total measurement time 44 min) and 5 runs with time resolution of 300 μs (total effective measurement time 9 min, total measurement time 30 min).

From fitting these three data sets, we obtained a focus waist of $\omega_0 = (0.69 \pm 0.02) \mu\text{m}$ and a diffusion coefficient of $D = (401 \pm 11) \mu\text{m}^2/\text{s}$ (mean \pm std). Laser power of the 633-nm Helium Neon laser was 50 μW , measured before the objective. We verified that an increased power up to 150 μW did not change the result, hence laser power used for the measurements was low enough to exclude photobleaching or optical saturation effects. No significant differences in the results from measuring Atto 655 NHS-ester and Atto 655 free acid were obtained. A higher diffusion coefficient by 6% for Atto 655 free acid would be expected due to the smaller molecular mass (625 and 528 Da, respectively). However, the ester was probably completely dissociated when measuring in water.

The average result of ten measurements on Atto655 NHS-ester and the free acid was $D = (400 \pm 8) \mu\text{m}^2/\text{s}$ at a temperature of $\vartheta = (22.2 \pm 0.3) ^\circ\text{C}$. Temperature was measured with a digital thermometer (Votcraft K202, Conrad, Hirschau, Germany), using a sensor cable attached to the objective lens. Taking into account the diffusion coefficient dependence on temperature (equation 2.17), this corresponds to a diffusion coefficient of $D = (431 \pm 9) \mu\text{m}^2/\text{s}$ at 25 $^\circ\text{C}$, a value in excellent agreement to the one published in (15) of $D = (426 \pm 8) \mu\text{m}^2/\text{s}$.

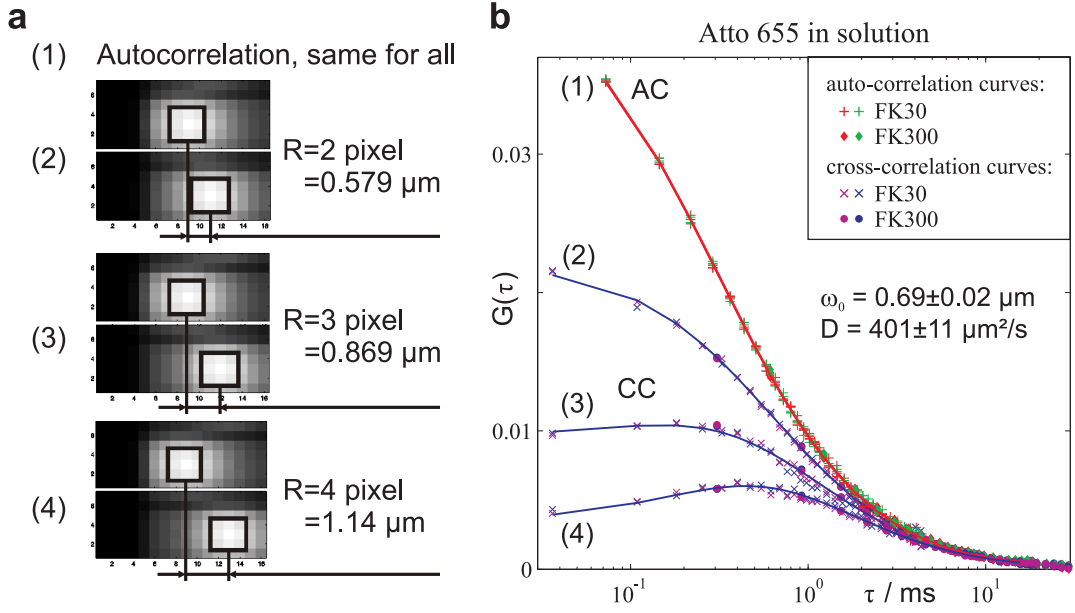


Figure 10.1.: Two-focus EMCCD-FCS on Atto 655 NHS-ester in solution. **a:** Temporal averages of odd and even frames, respectively, for distances of 2, 3 and 4 pixels on the EMCCD. **b:** Auto- and cross-correlation curves, measured at $22.2 \pm 0.3 \text{ }^\circ\text{C}$ in the fast kinetic mode. The average correlation data from 10 runs with time resolution of $30 \mu\text{s}$ and 5 runs with time resolution of $300 \mu\text{s}$ were fit to the generalized Gauss-Lorentz model (section 2.4.2). Fast kinetic series consisted of 146 exposures on chip and 2500 repetitions. Effective measurement time was $10 \times 11 \text{ s}$ and $5 \times 110 \text{ s}$, respectively; in sum 11 min. The total measurement time, including the camera readout gaps, was 74 min.

Employing a 488-nm laser, we measured two-focus EMCCD-FCS curves for Alexa 488, Rhodamine 6G and enhanced green fluorescent protein eGFP. Correlation curves and fit results are shown in fig. 10.2 and 10.3. Laser power was $70 \mu\text{W}$ for Alexa 488 and Rh6G and $40 \mu\text{W}$ for eGFP. The focus waist ω_0 varied for different sets of measurements, since different lasers were utilized, and excitation pathways were repeatedly adjusted and optimized. Within one set of measurements, the waist was constant within the experimental error of below 5%. Excitation pathways for both focal volumes were precisely adjusted to yield equal autocorrelation curves in all measurements.

The diffusion coefficients, determined at a temperature of $\vartheta = (23.0 \pm 0.5) \text{ }^\circ\text{C}$ for these measurements, can be recalculated to the values at $25 \text{ }^\circ\text{C}$: $D_{\text{Alexa 488}} = (438 \pm 19) \mu\text{m}^2/\text{s}$, $D_{\text{Rh6G}} = (445 \pm 22) \mu\text{m}^2/\text{s}$ and $D_{\text{eGFP}} = (107 \pm 5) \mu\text{m}^2/\text{s}$. They are very similar to recently determined values from APD-based two-focus FCS (83), circular scanning FCS (116) and measurements in capillary flow (122). For example, the present reference value for Rhodamine 6G is $(414 \pm 10) \mu\text{m}^2/\text{s}$, and we obtain $(445 \pm 22) \mu\text{m}^2/\text{s}$. Our value is by 7% higher, but still within the experimental error. Most importantly, we can confirm a value in this range, that is by 40% higher than the value of $(300 \pm 80) \mu\text{m}^2/\text{s}$ which had been used in most FCS publications over the last three decades.

We also measured the diffusion of the lipid dye DiD (Molecular Probes, Eugene, OR) in a supported planar DOPC bilayer (fig. 10.3 b). The bilayer was prepared on mica glued to a glass cover slide (31, 123). On membranes, photobleaching is much stronger than in solution due to the slow two-dimensional diffusion. The HeNe 633 laser was therefore attenuated with neutral density filters to $0.5 \mu\text{W}$. Furthermore, we employed smaller focal volumes than the ones for measurements in solution. Diffusion time through the focal volume was 15 ms, and therefore, a low time resolution of the

10. Precise determination of diffusion coefficients and flow speeds

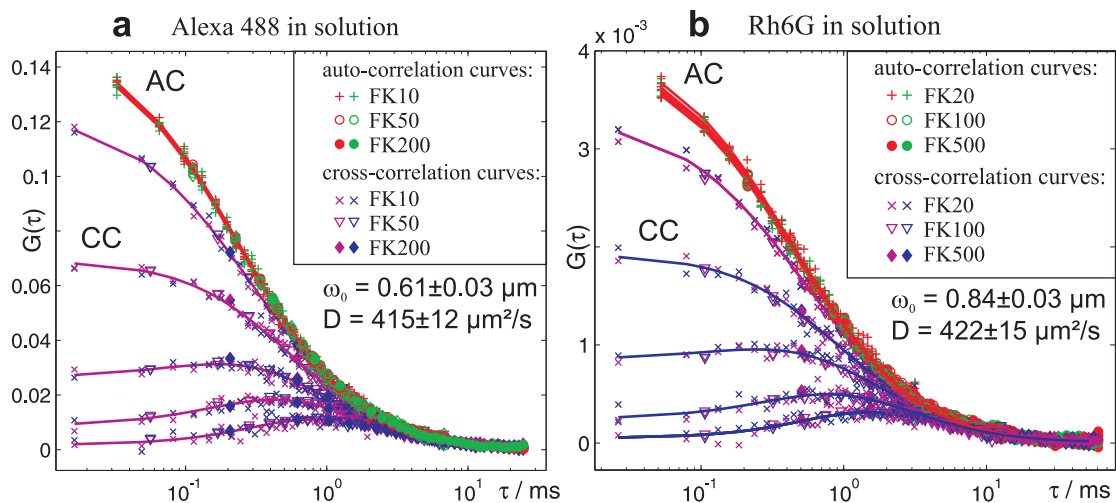


Figure 10.2.: Two-focus EMCCD-FCS on Alexa 488 and Rh6G in solution. **a:** Auto- and cross-correlation curves as in fig. 10.1, here for Alexa 488 with distances 1-5 pixels, averaged from fast kinetics measurements with time resolution of 10 μ s, 50 μ s and 200 μ s. Effective measurement time was 36 s, 90 s and 219 s, respectively. **b:** FCS curves for Rhodamine 6G, using fast kinetics with time resolution of 20 μ s, 100 μ s and 500 μ s. Effective measurement time was 44 s, 110 s and 73 s, respectively. Temperature was 23.0 ± 0.5 $^{\circ}$ C.

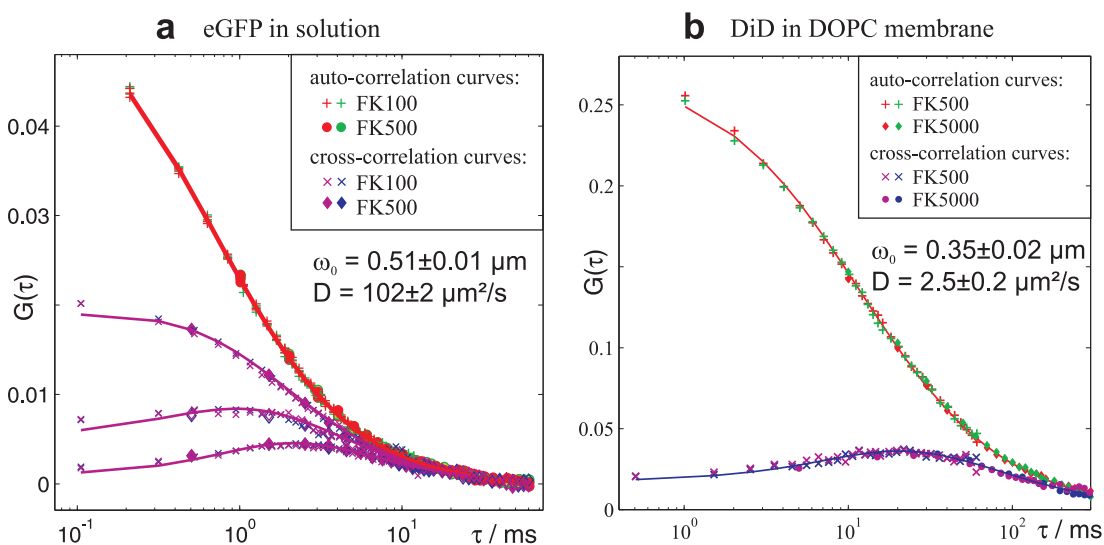


Figure 10.3.: Two-focus EMCCD-FCS on eGFP in solution and DiD in DOPC membrane. **a:** FCS curves for eGFP with distances 2-4 pixels and fast kinetics with time resolution of 100 μ s and 500 μ s. Effective measurement time was 213 s and 444 s, respectively. **b:** FCS curves for the fluorescent lipid DiD in a DOPC supported membrane bilayer, using a distance of 2 pixels and fast kinetics of 0.5 ms and 5 ms time resolution. Effective measurement time was 180 s and 365 s, respectively. FCS data from the membrane measurement was fit to a two-dimensional Gaussian model (equation 2.66 with $S \rightarrow \infty$ in section 2.4.2). Temperature was 23.0 ± 0.5 $^{\circ}$ C.

data acquisition for correlation analysis was sufficient. We used exposure times of 0.5 ms and 5 ms in the fast kinetic mode, and measurement time usage was hence comparably high (0.41 and 0.88, respectively). The deduced diffusion coefficient of $2.5 \mu\text{m}^2/\text{s}$ was in good agreement to a value of $2.6 \mu\text{m}^2/\text{s}$ obtained by two-focus scanning FCS (31).

10.2. Effect of the confocal pinhole size

In APD-based two-focus FCS, one single detection pinhole is employed (fig. 3.4 b in section 3.2), which is large enough to allow the passing of light from both overlapping focal volumes (15). This leads to comparable large axial dimensions of the detection volumes, unpractical for measurements e.g. in cells. This is not the case for EMCCD-based two-focus FCS, where pixel ranges on the camera serve as pinholes. Individual pixel ranges can be used for each of the two focal volumes, and the size can be varied in the data evaluation process (chapter 6). EMCCD-based two-focus FCS allows therefore to investigate the influence of the confocal pinhole size on the fit results.

Measurements were performed for the well characterized reference dye Rhodamine 6G in solution. Data was acquired in the fast kinetic mode with three different time resolutions of $20 \mu\text{s}$, $100 \mu\text{s}$ and $500 \mu\text{s}$, as before (fig. 10.2 b). However, in order to evaluate correlation curves for larger pinhole sizes, we used a bigger subregion on the EMCCD for data acquisition (fig. 10.4).

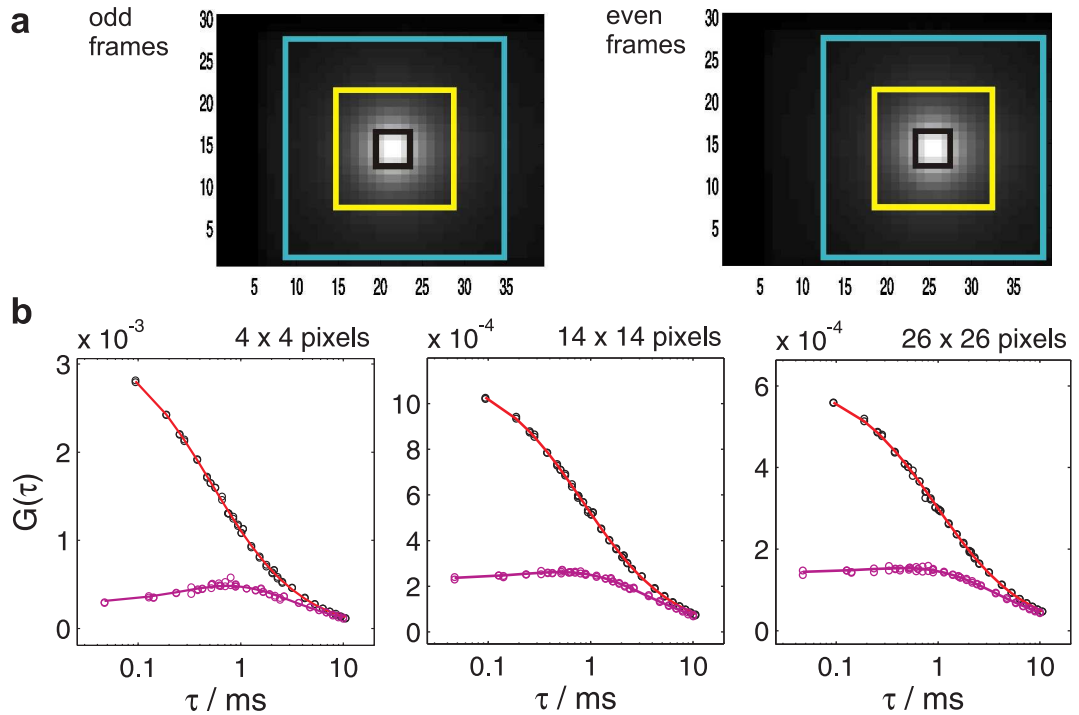


Figure 10.4.: Two-focus EMCCD-FCS on Rh6G in solution with different pinhole sizes. **a:** Temporal averages of odd and even frames, respectively, and differently sized pixel ranges on the EMCCD of 4×4 , 14×14 and 26×26 pixels used for data evaluation. Distance of the two focal volumes was four pixels. **b:** Auto- and cross-correlation data, combined from all exposures, (open circles) and fit curves (lines) for the different pinhole choices in (a). Effective measurement time was 21 min, total measurement time was 12 hours. Deduced fit parameters are given in fig. 10.5.

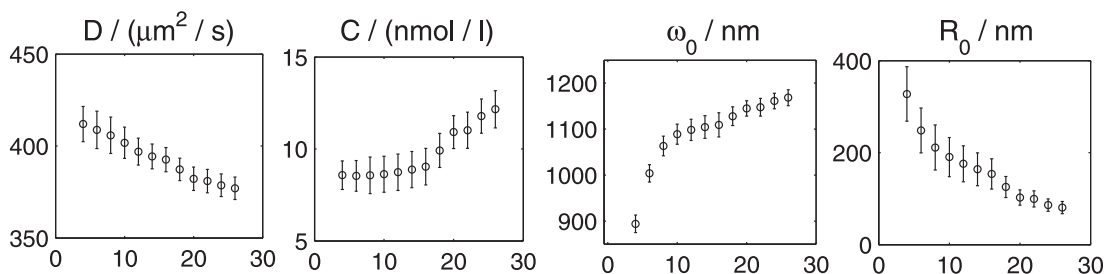
10. Precise determination of diffusion coefficients and flow speeds

The horizontal subregion was increased to 39 pixels, compared to 16 pixels in the measurements before (fig. 10.1 a). The vertical subregion, that is the number of EMCCD lines used in the fast kinetic mode, was increased to 30 lines, compared to 7 lines employed before. Only 34 exposures could be stored on the double chip of 2×512 lines, compared to 146 exposures used before. This decreased the measurement time usage by factor four. The data files were bigger by factor 2.4, according to the larger horizontal pixel range employed. Due to the limited computer random access memory, the number of repetitions of the fast kinetic series had to be reduced from 2500 to 1000. The lower number of exposures on the chip and the reduced number of repetitions resulted in a total effective measurement time of only 31 s, at a total measurement time of 18 min including the camera readout gaps, for one script series with the three exposure times.

With the automatic data acquisition script program and the stable hermetically sealed samples, we could repeat these measurement series over several days and average the correlation curves. Correlation data shown in fig. 10.4 b are averaged curves from 40 experiments. The total effective measurement time was 21 min (3 min, 7 min and 11 min for FK20, FK100 and FK500 fast kinetics, respectively) and the total overall measurement time was 12 hours.

The pinhole size influences the size of the confocal volumes. This can be directly seen from the correlation curves in fig. 10.4 b. The amplitudes are smaller for larger pinhole sizes, and the cross-correlations curve is flatter for short lag times due to a larger overlap in case of bigger focal volumes. When fitting the data, the parameters ω_0 , R_0 and S , which describe the confocal volume, were expected to change with pinhole size, whereas the parameters concentration and diffusion coefficient ideally should be constant. However, we obtained a dependency of all fit parameters (fig. 10.5).

Generalized Gauss-Lorentz model



3D-Gauss model

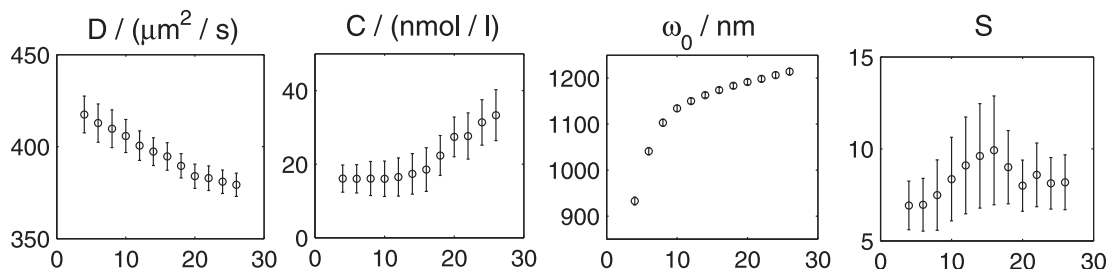


Figure 10.5.: FCS fit parameters for different pinhole sizes. Resulting parameters from fitting two-focus FCS curves as in fig. 10.4 b with two individual pinholes to the generalized Gauss-Lorentz or the 3D-Gauss model (section 2.4.2), respectively, plotted against the pinhole side length in pixels on the EMCCD. All fit parameters depend on the pinhole size. Error bars are 95% confidence intervals of the parameter estimates.

Both fit models yield similar dependencies for the diffusion coefficient D , the concentration C and the focal waist ω_0 . The parameter R_0 in the generalized Gauss-Lorentz model also clearly depends on the pinhole size whereas the structure parameter S in the 3D-Gauss model is rather constant. We verified that using circular pixel ranges on the EMCCD (as for example shown in fig. 10.7 a) instead of square pixel ranges led to only minor changes of the resulting absolute values, and to the same dependencies on pinhole size.

In spite of the dependencies, which indicate the inability of both theoretical models to completely describe the focal volumes, the variation of the diffusion coefficient over the whole range of pinhole sizes is only about 10%. This is still a range in agreement with the expected value of $(393 \pm 20) \mu\text{m}^2/\text{s}$ at a temperature of $\vartheta = (23.0 \pm 0.5)^\circ\text{C}$ when assuming about 3% relative error in the distance determination (section 8.2). Both models yield by factor two different concentration values, probably due to the different assumptions on the focal geometry. However, for both models, the concentration is rather constant up to pinhole sizes of 14×14 pixels. This indicates that the focal volume deviates from both models for too large pinholes.

The choice of the pinhole size determines the size of the detection volume, but also the amount of signal taken for data evaluation. If we look at these two parameters, we see that one can either opt for comparably small detection volumes or for a high molecular brightness (figure 10.6). A medium pinhole side length (or diameter in case of a circular pinhole) of for example 14 pixels corresponds to $5.1 \mu\text{m}$ in sample space. The ratio of pinhole diameter and focus waist ω_0 is 4.7 in this case. This is comparable to pinhole choices in typical APD-based one-focus FCS setups, where ratios of 3 to 6 are employed depending on the optimization towards best conditions for a Gaussian detection volume (18), or for obtaining maximum counts per molecule (38).

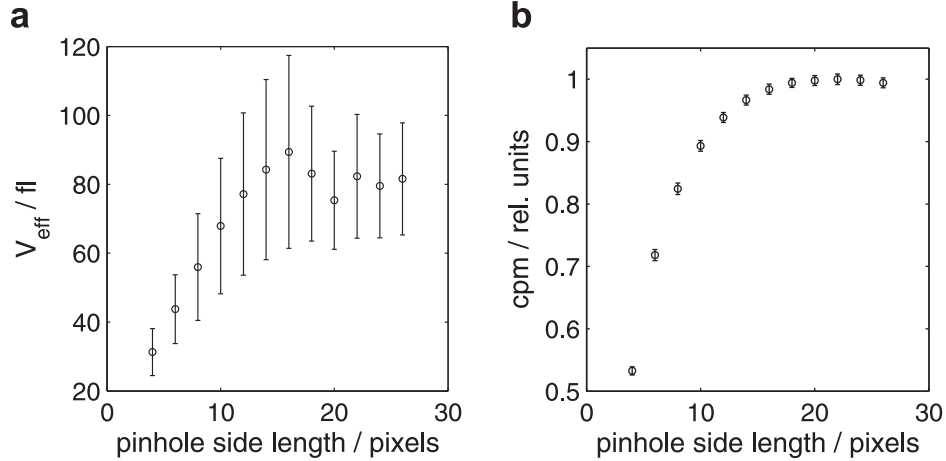


Figure 10.6.: Effective volume size and effective molecular brightness. Increasing the pinhole size up to 14×14 pixels enlarges the effective focal volume (a) and increases the counts per molecule (cpm) (b). The cpm are calculated by dividing the summed CCD signal over the pixel range by the number of molecules in the effective focal volume (equation 2.32), and they are normalized to the maximum value obtained for largest pinholes.

We next compared the results from using two individual pinholes to the situation of one common axially centered pinhole for both focal volumes as used in APD-based two-focus FCS (15). As an example, we used quasi-circular pixel ranges on the EMCCD for this comparison (fig. 10.7), although square pixel ranges gave the same results. For a large common pinhole, we obtained similar fit results. However, using a pinhole with a diameter smaller than 20 pixels led to strong deviations of

10. Precise determination of diffusion coefficients and flow speeds

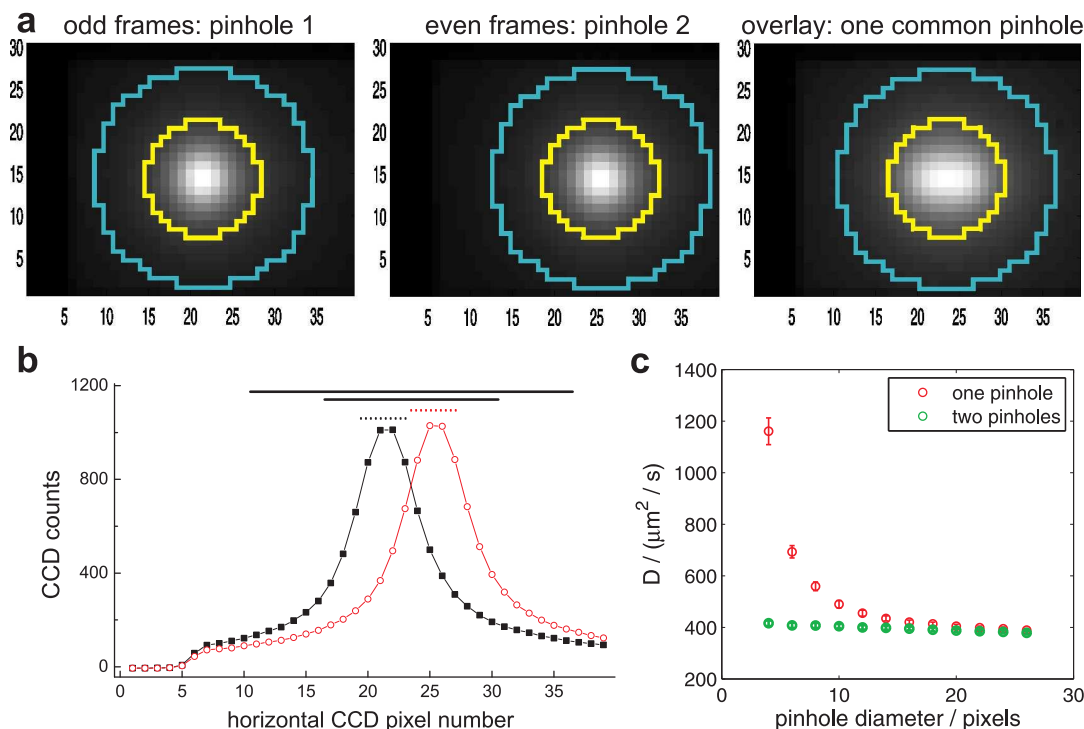


Figure 10.7.: Two-focus FCS with two individual or one common pinhole. **a:** Temporal averages of odd and even frames, respectively, and the overlay image. Marked are here quasi-circular pixel ranges of diameter 26 and 14 pixels. Either two individual symmetric pinholes around each focus were chosen, or one common pinhole for both foci, as used in APD-based two-focus FCS (15). **b:** Horizontal cross section at line 15 through the two individual images in (a). The horizontal bars above the curves indicate the pinhole diameters used to collect the data. Solid bars are diameters of 14 and 26 pixels for one common pinhole, and the dotted lines are two individual pinholes of 4 pixels diameter. **c:** The diffusion coefficient increases when using one small common pinhole for both spots, but it is much less dependent on pinhole size when using two individual pinholes.

the parameter estimates, for example to an increased diffusion coefficient (figure 10.7 c). This is understandable since the centered pinhole is asymmetric to the focus maxima and it hence distorts the assumed perfectly symmetric individual molecule detection functions (30). The pinhole diameter of 20 pixels, which was necessary to obtain a diffusion coefficient in the expected range, corresponds to $7.3 \mu\text{m}$ in sample space. The ratio of pinhole diameter and focus waist ω_0 is about 7 in this case. In APD-based two-focus FCS setups, similar large ratios of for example 9 and 14 have been employed (15, 83).

We conclude that individual pinholes are advantageous to obtain robust parameter estimates, especially when utilizing relatively small pinhole sizes for better confinement of the detection volumes. The possibility to have individual symmetric pinholes around each focus and changeable pinhole sizes, even in case of overlapping foci, is a unique feature of the EMCCD-based detection. For the measurements with two individual pinholes, we notice that the diffusion coefficient determination is rather independent on the employed theoretical model. However, the deduced concentrations are more sensitive to the assumptions on the focal volume geometry. It requires further experimental and theoretical investigation to completely explain these dependencies.

10.3. Determination of minute flows in micro channels

Experiments presented in this section were performed in collaboration with Dr. Ilaria Fortunati.

Although two-focus FCS has recently attained attention for its application to measure precise diffusion coefficients, it was first introduced and has mainly been used thereafter to measure directional motion, for example the flow characteristics in microfluidic channels (40, 42, 88). These channels can be parts of microfabricated devices for chemical analysis, clinical diagnostics, drug discovery, genomics and proteomics research. Advantages of miniaturization are small sample consumption, rapid analysis, and an integrated approach to perform different tasks as mixing, detection, sorting, amplification etc., in a single microfluidic device. The different tasks can be optimized with different flow velocities and hence a good understanding of the flow characteristics inside a microfluidic channel is necessary.

When FCS is used in microfluidic channels to measure flow velocity profiles, and by two-focus FCS also flow directions, there is always a lower limit for the accessible flow velocity. It is reached when diffusion dominates the FCS curve over flow, so that FCS curves for pure diffusion are indistinguishable within the noise of the experimental data from FCS curves for diffusion and flow.

This limit depends on the diffusion coefficient of the probe, but also on the focal volume size and the distance between the foci in two-focus FCS (equation 2.65). As a first approximation, the detectable flow velocity scales proportionally with the diffusion coefficient and inversely proportional with the size parameter ω_0 of the focal volume (fig. 10.8). This means that, for example, a ten times smaller flow velocity can be measured by either using a fluorescent probe with a ten times smaller diffusion coefficient, or by employing a focal volume with a ten times larger lateral radius.

Since focal volume size can not be changed easily in most standard FCS setups, typically larger fluorescent probes with a smaller diffusion coefficient like polystyrene beads or quantum dots have been used in the literature to study small flows (42). However, in many cases, the use of standard small organic fluorophores is advantageous, since:

- Fluorophores are single molecules with a defined size, diffusion coefficient and molecular brightness. In contrast, a sample of quantum dots or beads always exhibits a size and brightness distribution. This leads to additional noise in the correlation curves and requires longer measurement times to obtain a good average.
- Quantum dots and beads tend to form aggregates and stick to surfaces, and they can thereby block narrow channels. Sticking can as well occur for organic fluorophores, dependent on the affinity of the dye towards the specific material of the device, for example glass or polymeric materials. However, out of the huge list of available fluorophores, typically an appropriate non-interacting dye can be found easily.
- Organic fluorophores and fluorescent proteins are the standard labels for the biomolecules of interest. Probes as quantum dots or beads with large dimensions can change the physical properties or the biological function of the biomolecules. Moreover, for flow measurements, the large tracers could themselves modify the flow properties.

The aim of the study was therefore to measure the range of detectable flow velocities in a typical microfluidic channel when using our EMCCD-based two-focus FCS setup, compared to a standard one-focus APD-based setup. Our two-focus setup had comparably large focal volumes ($\omega_0 = 1.2 \mu\text{m}$) when compared to the commercial one-focus setup (Zeiss ConfoCor3, $\omega_0 = 0.19 \mu\text{m}$).

10. Precise determination of diffusion coefficients and flow speeds

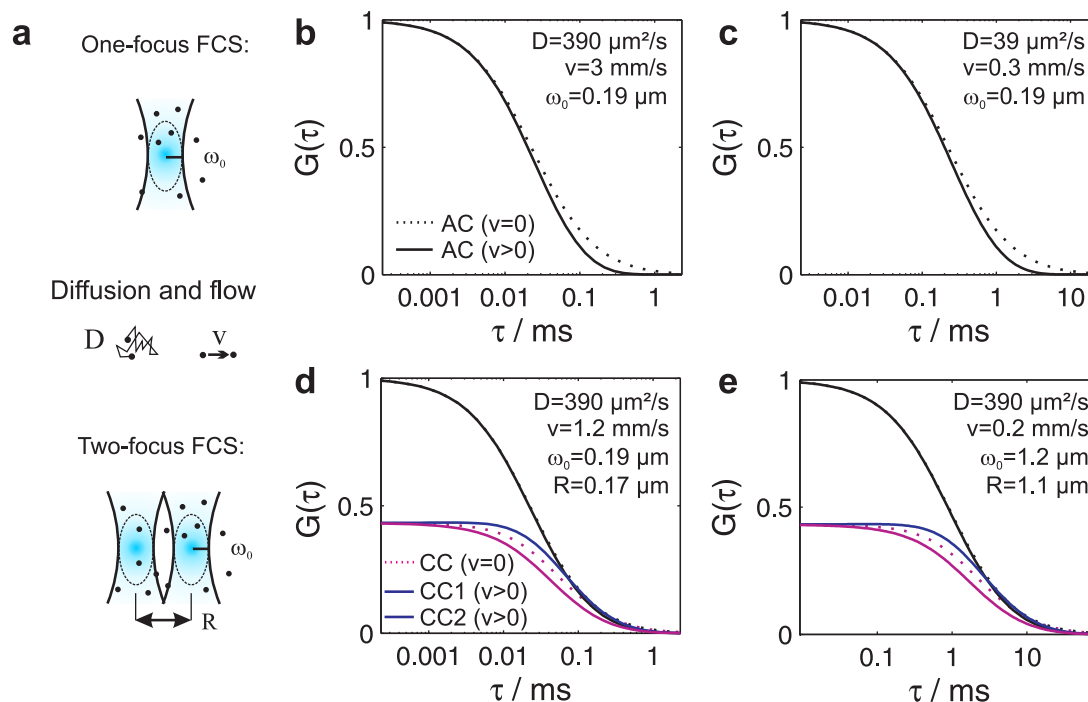


Figure 10.8.: Sensitivity of one and two-focus FCS to measure a flow process overlayed by diffusion. **a:** Sketch of molecules undergoing diffusion and flow, and the parameters which describe the detection volumes in case of a one-focus and two-focus FCS setup. **b–e:** Normalized FCS curves, calculated using equation 2.65 with parameters as given in the graphs and structure parameter $S = 5$, showing examples with clear differences for the case with and without flow. **b and c:** One-focus FCS. **b:** Using a diffraction limited detection volume ($\omega_0 = 0.19 \mu\text{m}$) and standard organic fluorophores ($D = 390 \mu\text{m}^2/\text{s}$), comparably large flow velocities on the order of mm/s are required to show an apparent effect on the autocorrelation (AC) curve. **c:** To access smaller flow speeds, larger fluorescent particles with a lower diffusion coefficient are usually employed. **d and e:** Two-focus FCS increases the sensitivity to detect flow processes overlayed by diffusion. **d:** In two-focus FCS, the cross-correlation curves (CC1 and CC2) are more sensitive to flow than the autocorrelation curve (AC). At a flow speed of for example 1.2 mm/s, the autocorrelation curves with and without flow almost don't differ, but the two cross-correlation curves split up clearly. **e:** Employing larger detection volumes, the sensitivity to detect small flow velocities is increased inversely proportional to the focal volume size. The overlap (R/ω_0) of the two focal volumes does not change the sensitivity. However, it has to be kept around one to obtain a measurable amplitude of the cross-correlation curves.

10.3. Determination of minute flows in micro channels

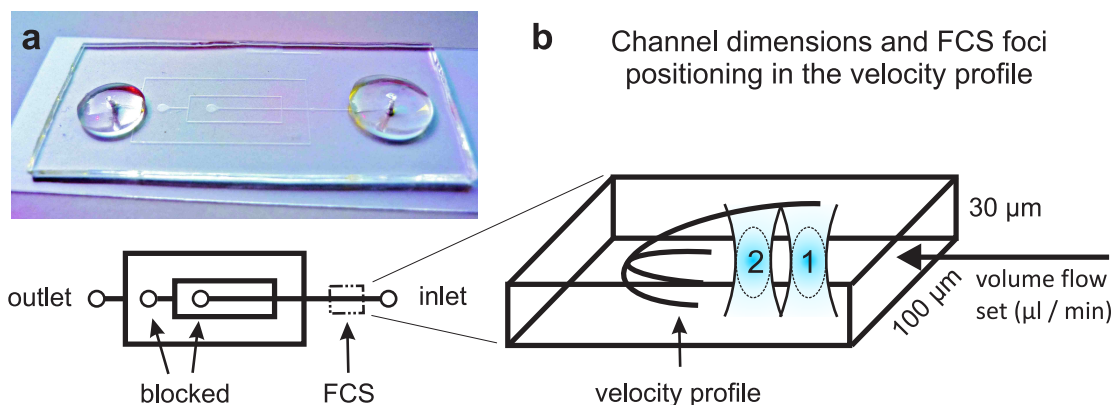


Figure 10.9.: The microfluidic channel. **a:** Photographic picture and schematic drawing of the employed PDMS microstructure. **b:** Dimensions of the channel and sketch of the FCS foci (not to scale) positions in the middle of the channel.

We employed nanomolar concentrated solution of the organic fluorophore Alexa Fluor 488 and used a polydimethylsiloxane (PDMS) microstructure, sealed to a coverglass (fig. 10.9). The structure would allow to connect four tubes to investigate mixing processes or hydrodynamic focusing. However, to investigate the range of accessible flow velocities, we only employed the simplest case of one inlet and one outlet, the two middle ones were not used and blocked. The inlet was connected with a tube to a syringe pump (KD Scientific, model KDS210, Holliston, MA, USA), where different volumetric flow rates (in microliter per minute) could be set.

Measurements were done in the center of the channel. Laser power in each of the two excitation foci was 70 μW measured before the objective. Two-focus FCS was performed with similar EMCCD settings as before. Fast kinetic measurements were done, using 14 upper CCD lines and 72 exposures

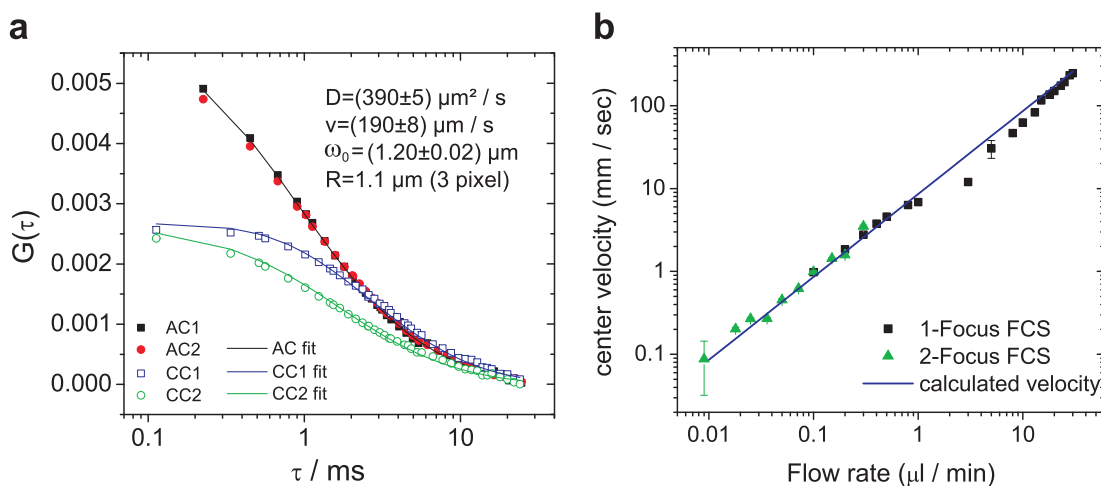


Figure 10.10.: Flow measurement results. **a:** Two-focus auto- and cross-correlation data and fit results for a measurement at a low flow rate of 0.018 $\mu\text{l}/\text{min}$. **b:** Deduced flow velocities from one-focus APD-FCS and two-focus EMCCD-FCS for different applied flow rates, showing good agreement to the expected flow velocities. Smaller flow velocities can be measured with the two-focus FCS setup.

10. Precise determination of diffusion coefficients and flow speeds

per double chip. Confocal pinhole size was 10×10 EMCCD pixels and the distance between the two foci was $1.1 \mu\text{m}$ (3 pixels).

Two sets of fast kinetic measurements with exposure times of $100 \mu\text{s}$ and $500 \mu\text{s}$ were performed. Effective measurement times were 0.7 min and 0.6 min, respectively, and total measurement times were 11 min and 2.3 min, respectively. A measurement curve for a low flow rate of $0.018 \mu\text{l/min}$ is shown in fig. 10.10 a, together with a fit to equation 2.65. A flow velocity of $v = (190 \pm 8) \mu\text{m/s}$ was deduced.

The measured flow velocities for different applied flow rates are given in fig. 10.10 b, together with results from one-focus FCS measurements at a commercial APD-based setup with a diffraction limited focal volume. With the flexible EMCCD-based setup, about factor ten smaller flow velocities could be measured. This is in accordance to the estimated gain in sensitivity (see fig. 10.8), which would be expected to be on the order of factor two to three due to using two-focus FCS, and times a factor six due to the larger focal volume size employed.

The obtained velocities were in good agreement to the expected maximum flow velocities in the center of the channel, which were calculated from the applied volume flow rate and the measured channel cross-section and pseudo-parabolic flow profile.

Conclusion of part III

In this part of the thesis, we have performed two-focus FCS measurements with an EMCCD camera. Owing to the flexible camera detection, our implementation is very versatile. It allows for variable and accurately determined distances between both spots. Furthermore, adequate symmetric confocal pinholes for both overlapping detection volumes can be chosen by the pixels, leading to a tight axial confinement.

We measured accurate diffusion coefficients of several fluorescent molecules in solution and on a planar lipid membrane and we reproduced the values in the literature obtained by recent APD-based two-focus FCS measurements. Furthermore, we employed the two-focus setup to measure laminar flow in a microfluidic channel. With our two-focus setup, utilizing the flexibility to employ comparably large focal volumes, we could measure about one order of magnitude smaller flow velocities compared to the commercial one-focus FCS setup.

We have analyzed and corrected all non-linearities that arise from EMCCD detection. This list of corrections can serve as a guideline for checking the performance of novel EMCCD detector models or other camera technologies that are to be used for FCS. The main limitation of the current EMCCD camera models is still the sequential readout of the chip, leading to dominating readout gaps and hence a much longer overall measurement time compared to APD-FCS. However, this is a technical limitation, that is likely to be solved in future camera generations.

Part IV.

FCS in developmental biology

FCS in developmental biology

Experiments presented in this part were performed in collaboration with Shuizi Rachel Yu.

In this part of the thesis, FCS is applied to explore molecular processes in living zebrafish embryos. The aim of the study is the investigation of the concentration gradient of the morphogen fibroblast growth factor 8 (Fgf8).

Chapter 11 briefly introduces the model system zebrafish, the basic concept of morphogens and the specific questions that are to be answered by FCS. For a detailed introduction into the developmental biology, the reader is referred to reference (124).

In chapter 12, results from one-focus FCS measurements are presented. The main result is the simple but important finding, that morphogen molecules largely diffuse as single molecules through the extracellular space. Precise values of the deduced diffusion coefficients are given. Additionally, FCS allows to identify a minor fraction of molecules that interact with a previously suggested extracellular matrix (ECM) component.

Two-focus EMCCD-based FCS, presented in chapter 13, specifically addresses the question whether there is any deviation from random Brownian motion. It is shown that there is no directional component in extracellular morphogen movement.

In chapter 14, the obtained *in vivo* morphogen concentration gradient is mathematically described and key parameters are extracted from the data. It is shown that endocytosis shapes the gradient by controlling the half life time of the morphogen within the extracellular space.

11. Introduction to Zebrafish embryo model system and the morphogen Fgf8

The development of a single fertilized egg cell into a whole multicellular organism is one of the most fascinating but also one of the most complex processes that are investigated in modern life sciences. Developmental genetics aims for understanding the influence of the genome on the phenotype in embryonic development. The three basic aspects in development are cell growth, cell differentiation and morphogenesis.

On the level of single molecules, morphogenesis is controlled by substances called morphogens. These are signalling molecules which can induce distinct cellular responses in a concentration-dependent manner. It is well accepted that tightly controlled concentration gradients of morphogens exist in developing tissue (125, 126). Cells in the target field of these concentration gradients can determine their position relative to the morphogen source, leading to a differential gene expression.

In this study, zebrafish (*Danio rerio*) serves as model organism for vertebrate development. An overview of zebrafish embryonic development is given in Fig. 11.1. Main advantages over other model organisms are:

- small size and optical transparency,
- large number of offspring and short generation time and
- robustness to microinjection for insertion of mRNA or fluorescent dyes.

Many examples of morphogens have previously been described, including fibroblast growth factor 8 (Fgf8) in zebrafish embryonic development (126–132). Fgf8 serves key inductive functions during vertebrate development, for example, in the early formation of the brain, heart and limbs (127–129). In gastrulating zebrafish embryos, Fgf8 is expressed in cells at the blastoderm margin, and it activates

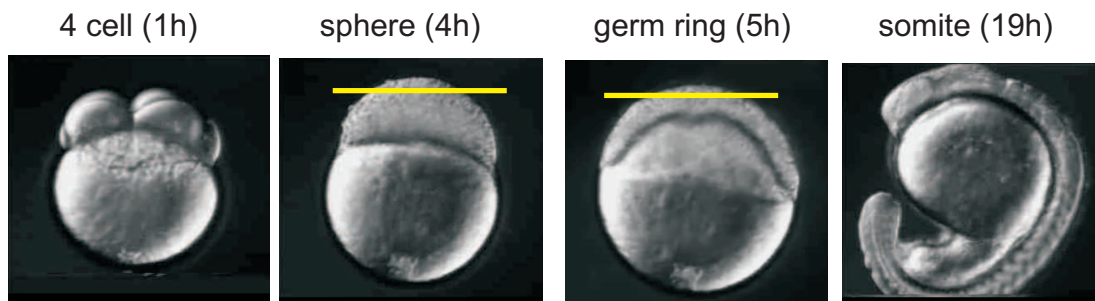


Figure 11.1.: Zebrafish embryonic development. Four developmental stages with names and hours after fertilization (images taken from <http://zfin.org>). Our measurements are performed between sphere and germ ring stages in one confocal section as denoted by the yellow line in the images.

11. Introduction to Zebrafish embryo model system and the morphogen Fgf8

its downstream target genes in successively broader domains away from its source towards the animal pole (127, 130–132).

How morphogens such as Fgf8 move through a tissue and set up concentration gradients remains debated (133–142).

In the 1970's, Francis Crick proposed that simple diffusion and spatially uniform degradation is sufficient for setting up gradients (133). This mechanism has been considered in various systems (136–141) and it has been shown that a random walk model can accurately describe the DPP morphogen gradient in *Drosophila* wing disks (140). Moreover, studies have suggested that morphogens can be sequestered from target tissue via receptor-mediated removal (132, 142). Meanwhile, alternative models including receptor aided bucket-brigade mechanism (134) and directed transport (141) have been proposed for morphogen spreading. However, a full biophysical description of morphogen gradient formation is still lacking. Physically, morphogen propagation may obey normal or anomalous diffusion, convection, directed intra- or extracellular transport, ligand-receptor binding kinetics or a combination of these.

The questions, that need to be addressed here, are:

- How does the morphogen Fgf8 move through the extracellular space?
- Does Fgf8 occur as single molecules or aggregates? Does it interact with ECM components?
- Does Fgf8 form a concentration gradient?
- If yes, is the gradient affected by endocytosis of the target cells?

FCS is uniquely suited for answering these questions. Previously, other fluorescent techniques such as optical imaging (141) and fluorescence recovery after photobleaching (FRAP) (140, 141) have been used for examining morphogen dynamics. Imaging can give a static picture of a gradient. Techniques like FRAP and FCS, however, can explore the dynamic state of the molecules forming the gradient.

In comparison to FRAP, the advantages of FCS are:

- FCS has fast sub-microsecond temporal resolution, making it ideal for assessing even the fast molecular dynamics such as diffusion of single molecules in the living embryo.
- FCS requires only nanomolar concentration of fluorescent molecules, therefore minimizing the interference of the labeling with the system.
- FCS is a single-molecule sensitive and direction-sensitive technique.
- FCS uses very low laser power, thus reducing photobleaching and the risk of damaging the live samples due to heating.

Here we report an FCS-based assay for examining the Fgf8 concentration gradient. By directly measuring the mobility of single Fgf8 molecules in living zebrafish embryos, we determine the gradient formation mechanism.

Labeling of Fgf8 and testing its functionality

In order to investigate any (bio-) molecule of interest with FCS, it has to be fluorescent. A strong and specific fluorescence signal can be obtained by an efficient labeling of the molecule. This is achieved by either biochemical labeling (143, 144) or molecular cloning with fluorescent proteins (145, 146). The great advantage of using fluorescent proteins is the direct expression of the tagged protein of interest by the cell or organism itself rather than external labeling and subsequent insertion.

For our study, we first tagged Fgf8 with enhanced green fluorescent protein (Fgf8-EGFP; Fig. 11.2 a). Fgf8-EGFP was readily taken up by target cells, and was recruited onto cell membranes by Fgf receptors (Fig. 11.2 b-c) (147).

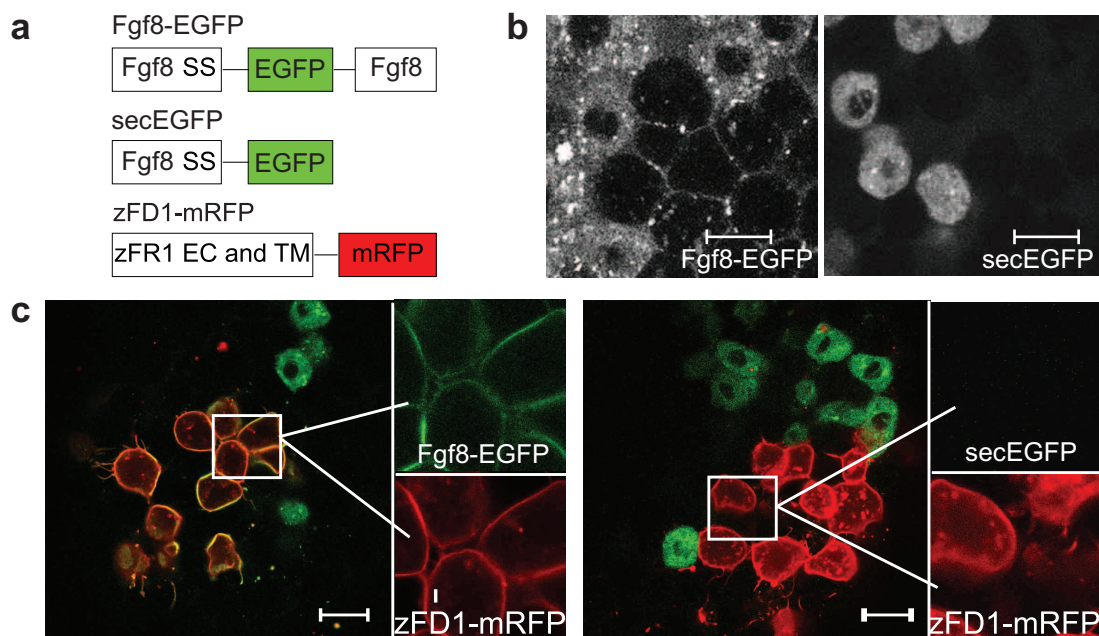


Figure 11.2.: Labeling of Fgf8 and proof of interaction. **a:** Fgf8-EGFP, secEGFP and zFD1-mRFP (monomeric red fluorescent protein) constructs. SS, zebrafish Fgf8 signal peptide (1-22 amino acids); zFR1, zebrafish Fgf receptor 1. EC and TM denote zFR1 extracellular and transmembrane domains (1-390 amino acids). **b:** In blastomere-injected embryos, Fgf8-EGFP is taken up into vesicular structures in target cells, whereas secEGFP is not (bright cells in the images are protein expressing cells). **c:** Fgf8-EGFP accumulates on zFD1-overexpressing cells, whereas secEGFP does not. Green: Fgf8-EGFP or secEGFP; red: zFD1-mRFP. Scale bars, 20 μm.

11. Introduction to Zebrafish embryo model system and the morphogen Fgf8

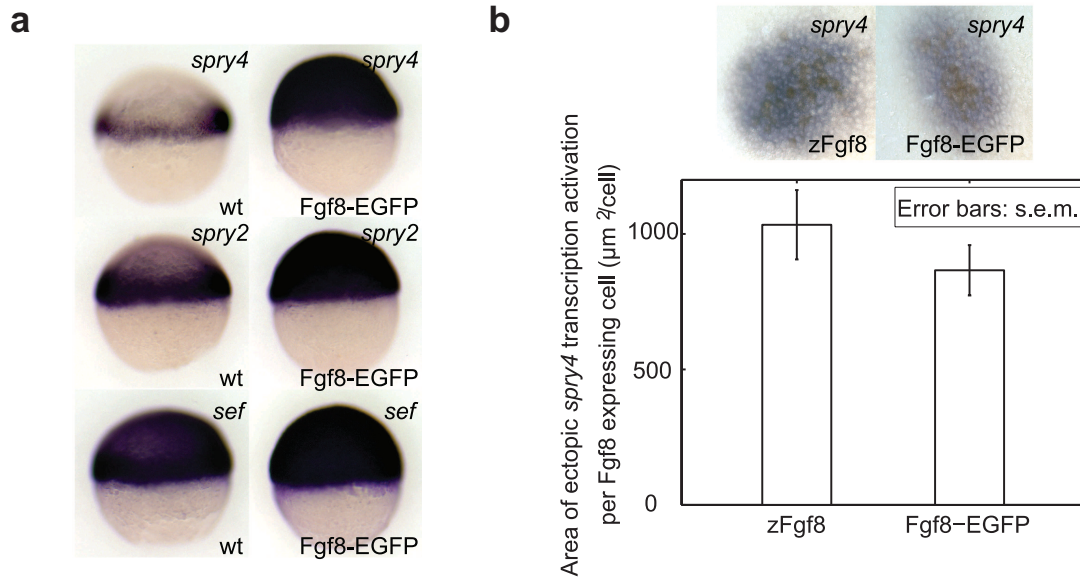


Figure 11.3.: Fgf8-EGFP has similar signalling capacities as non-labeled Fgf8. **a:** Global expression of Fgf target genes *spry4*, *spry2* and *sef* in embryos at 50% epiboly stage upon injection of 200 pg *fgf8-egfp* mRNA at single cell stage, side view with dorsal to the right. **b:** Comparison of signalling range of non-labeled zebrafish Fgf8 with Fgf8-EGFP. Brown: *zFgf8* or Fgf8-EGFP overexpressing cells, which were transplanted at 30% gastrula stage into the animal pole of a host embryo where *spry4* was not endogenously expressed at this stage of development; Blue: ectopic *spry4* expression. The difference in the ectopic *spry4* transcription activation area per Fgf8 expressing cell in the case of the untagged and EGFP tagged Fgf8 is not statistically significant: (1034 ± 128 , *zFgf8*, $n = 7$) vs. (866 ± 93 , Fgf8-EGFP, $n = 9$) $\mu\text{m}^2/\text{cell}$.

At equimolar concentrations, the fusion protein showed a similar capacity to induce target gene expression as untagged Fgf8 (Fig. 11.3).

As a negative control, we created a secreted version of EGFP (secEGFP). This protein was not recruited onto cell membranes and was not taken up by target cells, as expected (Fig. 11.2). Furthermore, we verified by western blot that the full-length fusion protein was the only EGFP-containing species in the extracellular space of *fgf8-egfp* messenger-RNA-injected embryos (148).

12. One-focus FCS in embryos

One-focus FCS was performed using a commercial ConfoCor2 (Zeiss) system with a C-Apochromat $\times 40$, NA 1.2 water immersion objective. The ConfoCor2 system was calibrated using Alexa Fluor 488 dye ($D = 414 \mu\text{m}^2/\text{s}$ at 25°C) (149) in solution to determine the focal volume parameters $\omega_0 = (0.19 \pm 0.01) \mu\text{m}$ and $S = (5.5 \pm 0.6)$ (mean \pm s.d., $n = 15$). EGFP and Alexa Fluor 488 were excited by a 488-nm line of an Ar-Ion laser using a power of $5 \mu\text{W}$. The emission was collected using a 505-550-nm band-pass filter. Measurement time was 10×10 s.

12.1. Major free diffusion of single morphogen molecules

To investigate how Fgf8 spreads into its target tissue, we took FCS measurements in the extracellular space of gastrulating zebrafish. Embryos were mounted with animal pole oriented to the top and vegetal pole to the bottom (Fig. 12.1 a) in 1% low melting point agarose. FCS measurements were taken in confocal planes approximately $15 \mu\text{m}$ below the enveloping layer of the embryos. To mimic the physiological situation of a restricted morphogen source, we injected two picograms of *fgf8-egfp* mRNA (124) into a single cell at 32-cell stage (blastomere injection) as shown in Fig. 12.1 b. The progeny of the injected cell formed a restricted source of the fluorescent protein in gastrulating embryos (Fig. 12.1 b-c).

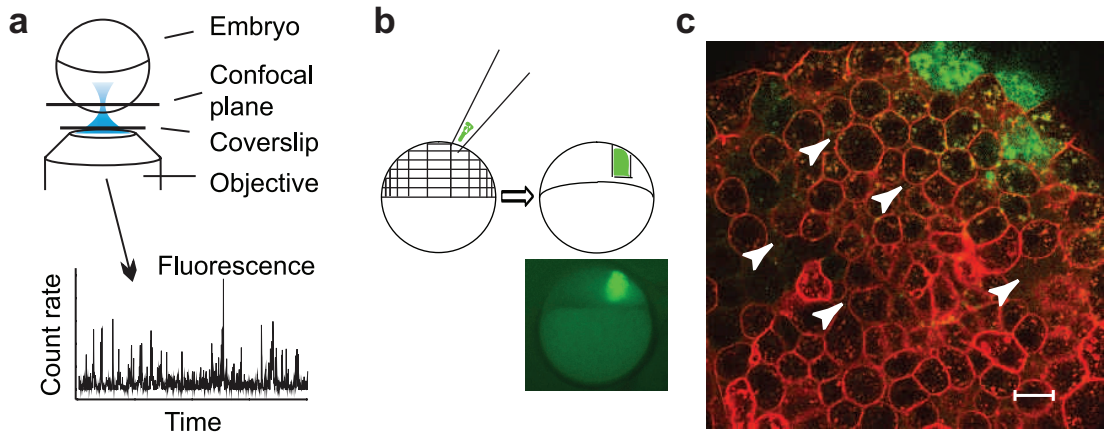


Figure 12.1.: FCS and embryo setup. **a:** Schematic setup for mounting the embryos. **b:** Sketch of blastomere injection and an injected embryo at sphere stage. **c:** Confocal image of a blastomere-injected embryo at 30% gastrula stage. Green: Fgf8-EGFP; red: mRFP-glycosyl phosphatidylinositol (GPI; a membrane marker); arrowheads denote extracellular spaces where FCS measurements are taken. Scale bar $20 \mu\text{m}$.

12. One-focus FCS in embryos

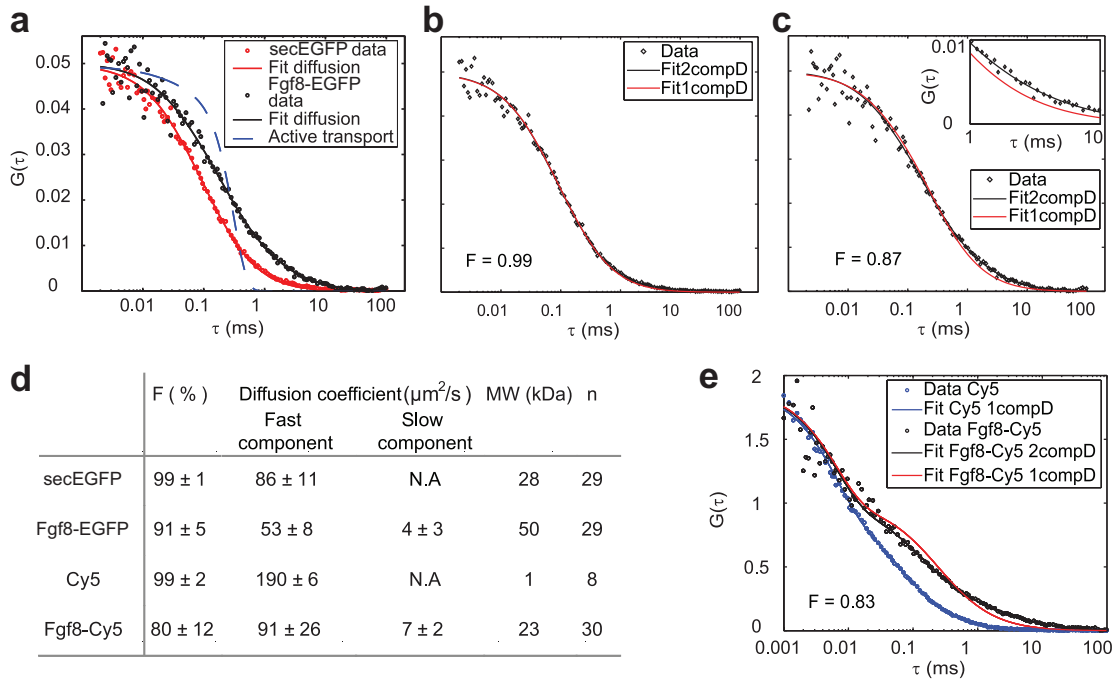


Figure 12.2.: One-focus FCS results. **a:** Comparison of autocorrelation curves for secEGFP (red) and Fgf8-EGFP (black) fit with three-dimensional diffusion model; the Fgf8-EGFP autocorrelation curve is also fit with a directional transport only model (blue). **b-c:** The two curves are displayed again separately in (b) secEGFP and (c) Fgf8-EGFP in order to see the fit with one (red) or two-component (black) diffusion model. F: fraction of the fast moving fluorescent species in the two-component fit model. **d:** Fit results of autocorrelation curves measured in zebrafish embryos. MW: molecular weight (without signal peptide). Data are mean \pm s.d. of n measurements. **e:** Fgf8-Cy5 in zebrafish embryos fit with one (red) or two-component (black) diffusion model. Cy5 in zebrafish embryos fit with one-component diffusion model (blue) for comparison.

FCS autocorrelation curves fit well to a three-dimensional diffusion model, but not with alternative models such as directional active transport only (Fig. 12.2 a). In a two-component fit, most of the molecules ((91 \pm 5)%) had a diffusion coefficient of $D_{\text{Fgf8-EGFP}} = (53 \pm 8) \mu\text{m}^2/\text{s}$ (mean \pm s.d.) that was on the same order of magnitude as that of secEGFP of $D_{\text{secEGFP}} = (86 \pm 11) \mu\text{m}^2/\text{s}$ (Figs. 12.2 b-d). Fgf8-EGFP moved slightly slower than secEGFP, as is expected for a larger molecule.

For a receptor-mediated bucket-brigade mechanism (134), we would expect most of the ligand to have a diffusion coefficient similar to that of the lateral mobility of the Fgf receptor in the cell membrane, which is about 100-fold smaller (59) than the one we measured for Fgf8, thus arguing against this mechanism for Fgf8 spreading.

The Fgf8-EGFP diffusion coefficient in the zebrafish embryos is two orders of magnitude larger than that reported for DPP ($0.10 \mu\text{m}^2/\text{s}$) in *Drosophila* wing discs (140). This supports the notion that the two morphogens have very different propagation mechanisms in their respective target tissues. DPP is transported by transcytosis involving repeated cycles of endocytosis and exocytosis through target cells (135, 140). This is likely to occur much slower than the free diffusion of Fgf8-EGFP in the extracellular space.

In addition, we analysed recombinant Fgf8 protein labeled with an organic dye Cy5. To create a restricted source of Fgf8-Cy5, Polystyrene microbeads (45 μm , Polysciences) were soaked in 50 ng/ml

12.2. Minor slow diffusion due to interaction with extracellular matrix components

Fgf8-Cy5 solution overnight before they were implanted at the animal pole of the zebrafish embryos at sphere stage. FCS was used to measure the diffusion coefficient of the labeled protein in the extracellular space around the bead. Cy5 was excited by a 633-nm HeNe laser, using a laser power of 7 μW and a 650-nm long-pass emission filter. The autocorrelation curve of Fgf8-Cy5 fit also well to a three-dimensional diffusion model (Fig. 12.2 e). The majority of molecules ($(80 \pm 12)\%$) had a diffusion coefficient of $D_{\text{Fgf8-Cy5}} = (91 \pm 26) \mu\text{m}^2/\text{s}$ (Fig. 12.2 d).

This shows that different fluorescent tags did not affect the mechanism of Fgf8 propagation. The similarity of the diffusion coefficients of Fgf8-EGFP, Fgf8-Cy5 and secEGFP to that of EGFP in buffer ($95 \mu\text{m}^2/\text{s}$) (116) suggests that these molecules all move as single molecules by free Brownian diffusion through the extracellular space.

12.2. Minor slow diffusion due to interaction with extracellular matrix components

We detected a small fraction of the extracellular Fgf8-EGFP ($(9 \pm 5)\%$) that was moving significantly slower ($(4 \pm 3) \mu\text{m}^2/\text{s}$) than the diffusing majority. This fraction was also present for Fgf8-Cy5 but not for secEGFP (Fig. 12.2 d), suggesting Fgf8-specific interactions within the extracellular space.

One likely contributor to the slow moving Fgf8 is its potential interactions with extracellular matrix (ECM) components such as heparan sulphate proteoglycans (HSPGs). HSPGs are cell-surface or extracellular matrix glycoproteins that are modified by the addition of one or several glycosaminoglycan (GAG) chains. It has been suggested that they interact and are required for the distribution and signalling of various Fgf growth factors (150) and other signalling molecules (151).

To test if the slow component might reflect interactions with ECM, we performed heparinase I (HepI, H2519 Sigma) injections into extracellular space. HepI is an enzyme which cleaves heparin and heparan sulfate sugar chains (152). Zebrafish embryos injected with HepI into the extracellular space at 256-cell stage showed expansion of expression of Fgf target genes such as *spry4* and *pea3* during gastrulation stages (148), indicating an increased range of Fgf signalling. A similar phenomenon was observed after treatment with HepII and Chondroitinase.

These results suggest that HSPGs are required to restrict the signalling range of Fgfs. HepI, through cleaving proteoglycans, might release cell-surface or ECM bound Fgfs and thus allow long-range signalling. Consistently, FCS measurements showed a one-third reduction in the percentage of slow moving Fgf8 in the HepI treated embryos ($5.6 \pm 0.5\%$) in comparison to the control embryos ($8.6 \pm 0.9\%$) (median \pm s.e.m., $n = 231$, Fig. 12.3). The diffusion coefficients of the fast and slow fraction, respectively, were similar in HepI treated embryos ($D_{\text{fast,HepI}} = (44 \pm 6) \mu\text{m}^2/\text{s}$, $D_{\text{slow,HepI}} = (4 \pm 4) \mu\text{m}^2/\text{s}$) and in the control embryos ($D_{\text{fast,control}} = (53 \pm 8) \mu\text{m}^2/\text{s}$, $D_{\text{slow,control}} = (4 \pm 3) \mu\text{m}^2/\text{s}$). Hence, only the fraction was reduced. The effect was significant but small, since the slow diffusing fraction was already a minor component.

To test the opposite effect, whether we could also increase the fraction of slow moving Fgf8, we injected heparan sulphate (the negatively charged sugar chain of HSPG, H7640 Sigma) into the extracellular space of zebrafish embryos. This resulted in a considerable increase in the slow moving Fgf8 component (control ($8.6 \pm 0.9\%$) vs. heparan sulphate injected ($36 \pm 5\%$), median \pm s.e.m., $n = 146$, Fig. 12.3).

12. One-focus FCS in embryos

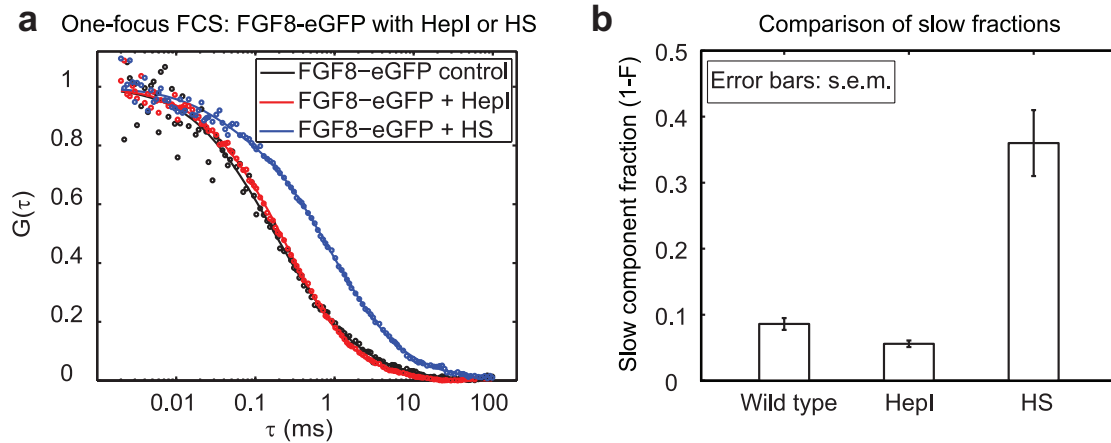


Figure 12.3.: The slow moving fraction of Fgf8. **a:** One-focus Fgf8-EGFP autocorrelation curves in the presence of HepI (red) or heparan sulphate (HS; blue). **b:** Deduced fractions of slow moving Fgf8. Significant changes suggest that the slow component reflects the interaction of Fgf8 with the matrix component HSPG.

Together, we propose that:

1. The majority of the extracellular Fgf8 are freely-diffusing. This allows the molecules to spread quickly into the target tissue and to set up morphogen gradient.
2. HSPG bound Fgf8 contributes to the minor slow-moving Fgf8 fraction detected in FCS and this interaction affects the correct Fgf8 signal propagation. HSPGs could act as co-receptors for Fgf8 signalling (150), or they could be involved in sequestering Fgf molecules close to the source and therefore contribute to the shaping of the Fgf gradient.

13. Two-focus EMCCD-FCS in embryos

With standard one-focus APD-FCS, we have ruled out the directional active-transport-only model for Fgf8 tissue propagation (Fig. 12.2 a). However, to examine whether Fgf8 movement has any active transport component, we used two-focus FCS (part III).

To achieve a better sensitivity to potential deviations from pure diffusion (as discussed in section 10.3), we employed comparably large focal volumes in our EMCCD-based two-focus setup ($\omega_0 = 0.68 \mu\text{m}$), when compared to the size of the diffraction-limited focal volume ($\omega_0 = 0.19 \mu\text{m}$) in the commercial one-focus setup, used in chapter 12. Figure 13.1 shows the theoretical two-focus curves that would be expected in case of pure diffusion or directional propagation of morphogen molecules ($D = 60 \mu\text{m}^2/\text{s}$, $v = 0$ to $v = 50 \mu\text{m}/\text{s}$).

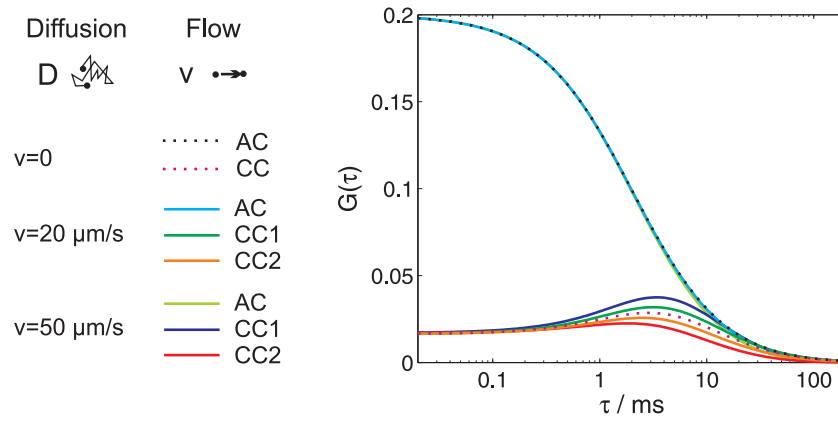


Figure 13.1.: Theoretical two-focus FCS curves with diffusion and flow. Model autocorrelation (AC) and cross-correlation curves (forward cross-correlation CC1, and backward cross-correlation CC2) using equation 2.65 in case of pure diffusion ($D = 60 \mu\text{m}^2/\text{s}$, $v = 0$) and in case of a combination of diffusion and flow ($D = 60 \mu\text{m}^2/\text{s}$, $v = 20 \mu\text{m}/\text{s}$ and $v = 50 \mu\text{m}/\text{s}$). Two-focus FCS is more sensitive to detect deviations from pure diffusion than one-focus FCS (as discussed in section 10.3, fig. 10.8).

The home-built two-focus setup (part III) was used with the following parameters. The two focal volumes had a lateral distance of $R = 1.1 \mu\text{m}$ in the sample. Laser power in each of the two excitation foci was $21 \mu\text{W}$ measured before the objective. Fluorescence was detected by the EMCCD model DU897. The EMCCD was operated in the fast kinetic acquisition mode, where only the upper seven lines of the image chip were used. With alternating excitation by AOMs, 146 exposures of $200 \mu\text{s}$ were taken and stored on the chip. Each single measurement consisted of 1,000 repetitions. The effective measurement time was 60 s for each focal volume (4 runs \times 15 s each). The total measurement time was $9\times$ longer owing to the camera readout time gaps in the non-continuous fast kinetic acquisition mode (section 5.2). Due to the non-continuous mode, the maximal correlation time was at 15 ms.

Typical two-focus FCS measurement data of Fgf8-EGFP in embryos are shown in Fig. 13.2 b. The auto- and cross-correlation curves were globally fit to a model including both diffusion and directed transport (equation 2.65). The forward and backward cross-correlation curves were identical within

13. Two-focus EMCCD-FCS in embryos

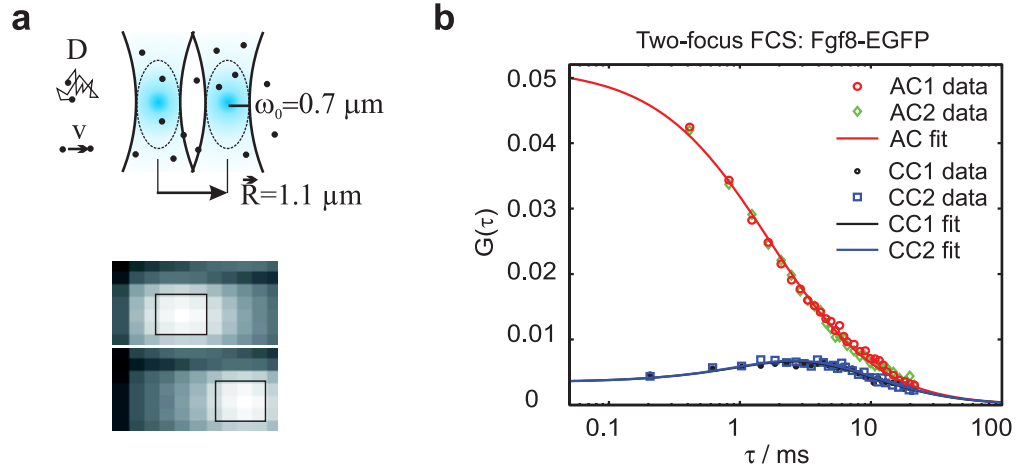


Figure 13.2.: Two-focus FCS results. **a:** Fluorescence from the two laterally shifted and alternately excited large focal volumes is detected with an electron multiplying CCD camera (integrated images over time of odd and even exposures, respectively), and intensity traces are extracted from the 3x3 pixel regions marked in the images. **b:** Two-focus autocorrelation (red and green) and cross-correlation (blue and black) data for Fgf8-EGFP fit with a diffusion-directed transport model. The two cross-correlation curves are identical within the experimental error confirming that there is no deviation from pure diffusion.

the experimental error. From the ten measurements for Fgf8-EGFP in the extracellular space of zebrafish embryos, a diffusion coefficient of $D = (64 \pm 6) \mu\text{m}^2/\text{s}$ and a speed constant of $v = (2 \pm 4) \mu\text{m}/\text{s}$ were obtained (mean \pm s.d.). The statistical variation of the two cross-correlation curves determines the detection limit, which is approximately $v = 5 \mu\text{m}/\text{s}$. However, even if there was a directionality below this detection limit, the overall fast diffusion would dominate and determine the morphogen spread within the small extracellular spaces.

This confirms that the dominant driving force for Fgf8 propagation in target tissues is diffusion and there is no evidence for directed motion. Our finding agrees with the fact that free diffusion is a more efficient mechanism than directed motion for a molecule to traverse complex multicellular tissue (139).

14. Exploring the morphogen concentration gradient

A morphogen functions by providing positional information through formation of a protein concentration gradient (125, 126). Here, we visualize and describe the formation of the morphogen gradient in the living embryos.

The FCS measurements (chapter 12) were taken in various extracellular spaces and therefore at different distances from the expressing cells (Figs. 12.1 c and 14.1 a). From this data, we could extract the spatial concentration profile. As a measure for concentrations at particular positions in the embryos, the mean photon count rate I of the FCS measurement was used. It was a more robust measure for concentration than the deduced particle number N , when the focal volume was distorted in *in vivo* measurements due to mismatch between the refractive index of water and that of the embryonic tissue (148).

14.1. A stable morphogen gradient *in vivo*

The protein concentration decreased with increasing distance from the source in gastrulating zebrafish embryos, confirming that Fgf8-EGFP did establish a gradient in its target tissue. In contrast, secEGFP concentration remained nearly constant over distance (Fig. 14.1 b).

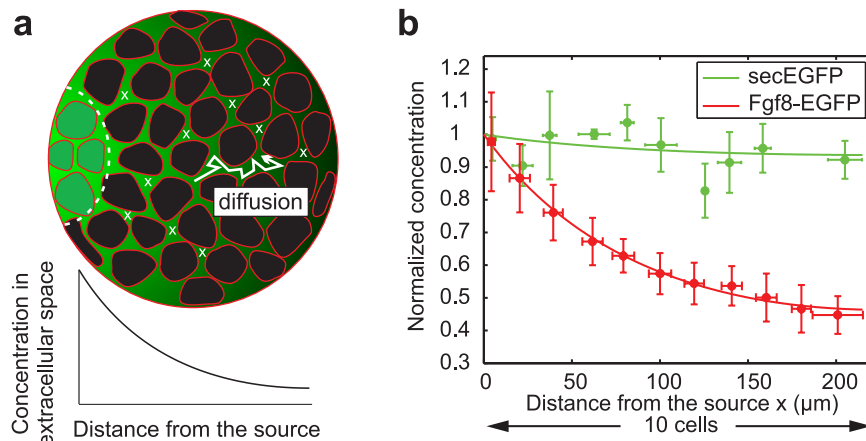


Figure 14.1.: Concentration gradient of Fgf8. **a:** Schematic drawing of a confocal section of the embryo (compare to Fig. 12.1 c). From the FCS measurements performed at different distances from the source (indicated by crosses), we can evaluate the extracellular concentration gradient. **b:** The Fgf8-EGFP concentration decreases as the distance from its source increases whereas that of secEGFP remains constant in gastrulating zebrafish embryos. Data from 40 embryos are binned in 20-μm intervals and fit with a radial model (section 14.2). Error bars denote s.d.

14. Exploring the morphogen concentration gradient

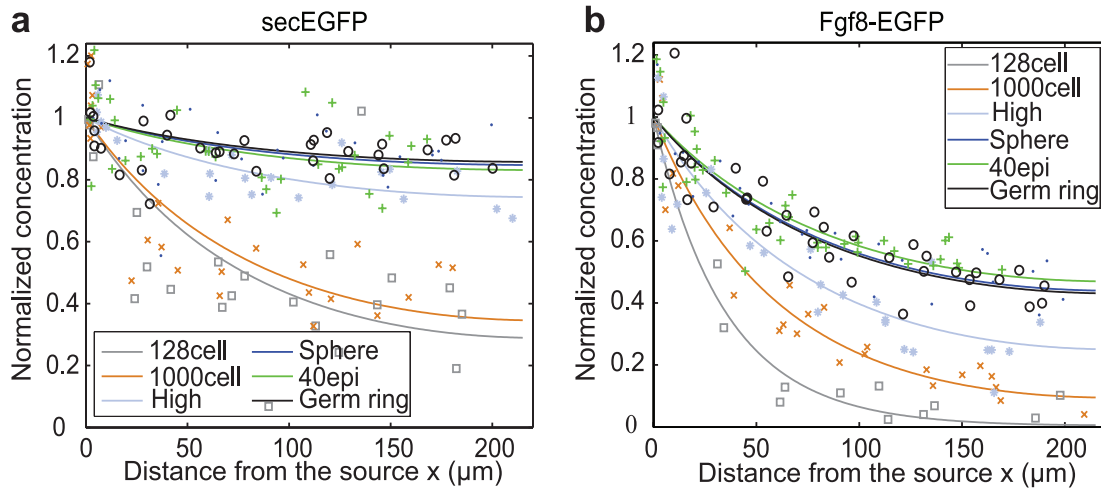


Figure 14.2.: Formation and maintenance of Fgf8-EGFP concentration gradient in the zebrafish embryos. Concentration measurements were taken for both secEGFP (a) and Fgf8-EGFP (b) in blastomere injected embryos (Fig. 12.1 b) at 128-cell, 1000-cell, high, sphere, 40% epiboly and germ-ring stages, corresponding to 0.75, 1.5, 2, 3, 4 and 5 hour after *secegf* or *fgf8-egfp* mRNA injection (embryos were kept at room temperature throughout the experiment). The concentration gradient of secEGFP becomes flat but that of Fgf8-EGFP is maintained from sphere stage ($n = 3$ embryos for each developmental stage).

The FCS autocorrelation measurements showed that Fgf8-EGFP had a similar diffusion coefficient to that of secEGFP (Fig. 12.2 d) meaning that both secreted molecules would be capable of spreading throughout the developing embryos by the time the concentration measurements were taken. Concentration measurements taken at different developmental stages showed that secEGFP reached uniform distribution from sphere stage onwards, whereas Fgf8-EGFP maintained its gradient from the same stage (3 hours after *secegf* / *fgf8-egfp* mRNA injection when embryos were incubated at room temperature throughout the experiment, Fig. 14.2). Therefore, it was not the diffusion that limited the availability of the morphogen molecules throughout the tissue. Rather, only the presence of a sink for Fgf8 in the target tissue could sustain the shape of its gradient.

All of the concentration data used for the following calculation of the gradient decay length and the half-life time of extracellular Fgf8-EGFP were collected for embryos that were incubated at 28 °C till sphere stage and then kept at room temperature during FCS measurements. The embryos used were between sphere and germ-ring stage (2 hours after sphere stage at room temperature).

14.2. Mathematical model and deduced key parameters

The observed Fgf8 gradient can be described by a simple model (140) assuming a localized source and equilibrium between diffusion and degradation (sink) as expressed in the following reaction-diffusion equation:

$$\frac{\partial C(\vec{r}, t)}{\partial t} = D \nabla^2 C(\vec{r}, t) - k C(\vec{r}, t) \quad (14.1)$$

in which $C(\vec{r}, t)$ is the concentration of the signalling molecule at position \vec{r} , t is the time, ∇^2 is the Laplace operator, D is the diffusion coefficient and k is the degradation rate. The localized source is taken into account by an appropriate boundary condition.

We solved equation 14.1 for the particular geometry of the embryos. At gastrulation stage, a clone of expressing cells formed the restricted source of Fgf8-EGFP, which was typically extended in the vertical direction (Fig. 12.1 b). This allowed us to consider the system only within the two-dimensional confocal plane of measurement. In a confocal image, several expressing cells could be identified. The boundary of this source was typically curved and it could be approximated by an arc of a circle of radius r_0 (Fig. 14.3 a).

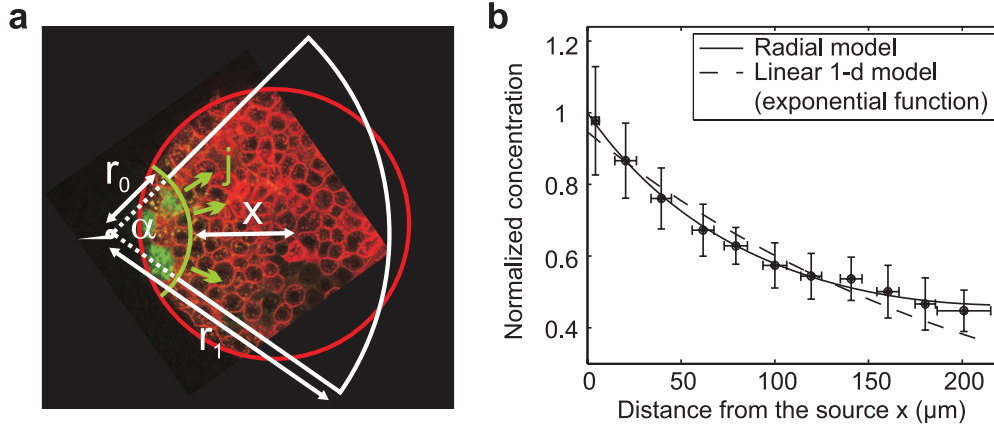


Figure 14.3.: Modelling of Fgf8-EGFP concentration gradient. **a:** The morphogen source boundary (green) and the circular shape of the sample in the confocal plane of measurement (red circle) can be approximated by two arcs of concentric circles of radii r_0 and r_1 . The target tissue can be approximated by a wedge delimited by these two arcs. We assume there is: 1. a morphogen current j at r_0 and 2. reflective boundary condition at r_1 and at the sides of the wedge. Concentrations are measured at distances x from the source boundary. **b:** The morphogen gradient of Fgf8-EGFP can be well described by the radial symmetric model. For comparison, a fit to an exponential function (1-dimensional linear model) is shown which describes the data less accurately.

Equation 14.1 describes the propagation of morphogens in the target tissue. The molecules diffuse, and they are degraded with a position-independent rate k . Morphogen production is expressed by a constant current j across the source boundary at $r = r_0$. The molecules are reflected back when reaching the enveloping layer of the embryos. The reflective boundary can be approximated by an arc of a bigger circle with radius r_1 , concentric to the smaller circle, and the sides of a wedge (Fig. 14.3 a) with an angle $\alpha \in (0, 2\pi)$.

With this radial symmetry, equation 14.1 reads:

$$\frac{\partial C(r, t)}{\partial t} = D \nabla^2 C(r, t) - k C(r, t) \quad (14.2)$$

where

$$\nabla^2 = \frac{\partial^2}{\partial r^2} + \frac{1}{r} \frac{\partial}{\partial r} \quad (14.3)$$

is the Laplace operator in the cylindrical coordinate system.

The steady-state solution of equation 14.2 is:

$$C(r) = \frac{j}{\sqrt{k D}} \frac{I_1(r_1/\lambda) K_0(r/\lambda) + K_1(r_1/\lambda) I_0(r/\lambda)}{I_1(r_1/\lambda) K_1(r_0/\lambda) - K_1(r_1/\lambda) I_1(r_0/\lambda)} \quad (14.4)$$

14. Exploring the morphogen concentration gradient

where

$$\lambda = \sqrt{\frac{D}{k}} \quad (14.5)$$

The following boundary conditions have been used:

1. There was a constant current j of morphogen being produced over the source boundary at r_0 :

$$j = -D \left. \frac{\partial C(r, t)}{\partial r} \right|_{r=r_0} \quad (14.6)$$

2. The morphogen molecules were reflected back at r_1 :

$$\left. \frac{\partial C(r, t)}{\partial r} \right|_{r=r_1} = 0 \quad (14.7)$$

and at the sides of the wedge.

Note that the solution (equation 14.4) does not depend on the wedge angle α due to the radial symmetry. In equation 14.4, $I_0(x)$ and $I_1(x)$ are the modified Bessel functions of the first kind, $K_0(x)$ and $K_1(x)$ are the modified Bessel functions of the second kind. The two radii were estimated by analyzing the confocal images as shown in Fig. 14.3 a. We obtained $r_0 = (85 \pm 15) \mu\text{m}$ and $r_1 = (310 \pm 10) \mu\text{m}$ (mean \pm s.e.m., $n = 10$ embryos).

Equation 14.4 can be rewritten as:

$$C(x) = \frac{j}{\sqrt{k} D} \frac{I_1((r_0 + x_L)/\lambda) K_0((r_0 + x)/\lambda) + K_1((r_0 + x_L)/\lambda) I_0((r_0 + x)/\lambda)}{I_1((r_0 + x_L)/\lambda) K_1(r_0/\lambda) - K_1((r_0 + x_L)/\lambda) I_1(r_0/\lambda)} \quad (14.8)$$

in terms of the measured distance x from the source boundary ($x = r - r_0$, Fig. 14.3 a). In equation 14.8, the radial distance from the source boundary to the reflective boundary is denoted as $x_L = r_1 - r_0 = (225 \pm 25) \mu\text{m}$.

The steady-state solution describes the Fgf8 concentration gradient very well (equation 14.8 and Fig. 14.3 b). The steepness of the decay of protein concentration against distance from source can be described by the decay length λ (equations 14.8 and 14.5).

By globally fitting the measured data from 40 embryos, we obtained a value of $\lambda = (197 \pm 7) \mu\text{m}$ (best fit value \pm 95% confidence interval), corresponding to an average of around nine cell diameters. At this distance from the source, the concentration of Fgf8-EGFP had decayed by approximately 50% (Figs. 14.1 b and 14.3 b).

Taking the value of the diffusion coefficient D determined in FCS, the degradation rate of the signalling molecule $k = D/\lambda^2 = (1.3 \pm 0.3) \cdot 10^{-3} \text{s}^{-1}$ could be calculated. The half-life time $t_{0.5}$ follows by $t_{0.5} = \ln(2)/k$. For Fgf8-EGFP, we obtained a half life time of about $(9 \pm 2) \text{min}$. In contrast, secEGFP had a much longer half-life of 84 min.

Note that we have used a two-dimensional radial model to describe the concentration profile (equation 14.8; Fig. 14.3 a) as an approximation of the real shape of the source and the target tissue in the zebrafish embryos. The experimental gradient data could be very well described by equation 14.8 (Fig. 14.3 b). For comparison, we also plotted the fit curve from an exponential model function, which described the data less well:

$$C(x) = \frac{j}{\sqrt{k} D} \exp\left(-\frac{x}{\lambda}\right) \quad (14.9)$$

The exponential function is the solution to equation 14.1 assuming a one-dimensional system in which the source boundary is a line and the target tissue is considered to be without the distal boundary. It is the limiting case of equation 14.8 when $r_0 \gg x_L \gg x$ and it has been used frequently to describe morphogen gradients in *Drosophila* embryos (141) and wing imaginal discs (140). However in the zebrafish embryos, the assumption of a radial symmetry and a finite domain with reflective boundary conditions is more appropriate.

14.3. Direct measurement of the half-life time

To validate the assumed model for gradient formation, and to confirm the indirectly inferred half life time, we measured the degradation directly. We injected 0.2 ng of the Cy5-labeled recombinant Fgf8 protein directly into the extracellular space between sphere and dome stage. The injection was done at five different positions in the embryo to ensure fast and even distribution of the protein throughout the embryo. After about 15 min, concentration of the labeled protein was determined at different positions in the extracellular space over time (Fig. 14.4).

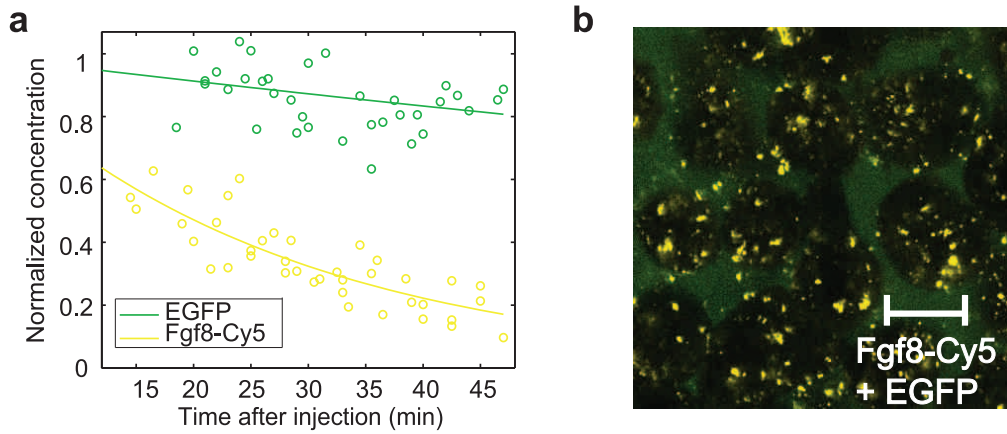


Figure 14.4.: Degradation rate of Fgf8-Cy5. a: Plot of the concentration of Fgf8-Cy5 and EGFP in the extracellular space of zebrafish embryos against time (protein concentrations are normalized to 1 at the time of injection $t = 0$ min). Data are fit with an exponential model (equation 14.10). The half-life of Fgf8-Cy5 averages to (18 ± 4) min (best fit value \pm 95% confidence interval, $n = 4$) and that of EGFP is (153 ± 21) min (best fit value \pm 95% confidence interval, $n = 2$). **b:** Confocal image of an embryo that was injected with Fgf8-Cy5 and EGFP into the extracellular space at the same time. Only Fgf8-Cy5 was taken up into the cells, whereas EGFP remained in the extracellular space. The embryo is oriented with animal pole to the top. Yellow: Fgf8-Cy5; Green: EGFP; Scale bars: 20 μ m.

The decrease in the count rate of Fgf8-Cy5 over time was fit with an exponential model, which is the solution of equation 14.1 with $\nabla C(\vec{r}, t) = 0$:

$$C(t) = C_0 \exp(-k t) = C_0 2^{-\frac{t}{t_{0.5}}} \quad (14.10)$$

and the half-life time $t_{0.5}$ of the molecule averaged to (18 ± 4) min (best fit value \pm 95% confidence interval, $n = 4$, Fig. 14.4 a). Control experiment where recombinant EGFP (BioVision) was injected together with Fgf8-Cy5 at the same time showed that only Fgf8-Cy5 was taken up into the target cells (Fig. 14.4 b). The concentration of EGFP in the extracellular space decreased much slower over time than that of Fgf8-Cy5 ($t_{0.5} = (153 \pm 21)$ min, best fit value \pm 95% confidence interval, $n = 2$).

14. Exploring the morphogen concentration gradient

The half-life time of Fgf8-Cy5 determined in this way was comparable to that calculated from the Fgf8-EGFP concentration profile confirming that we can estimate the half-life using the simple diffusion-degradation model (equation 14.1) and the diffusion coefficient D of the fast diffusing fraction measured with FCS. However, there exists a two-fold difference between the calculated half-life of Fgf8-EGFP and the measured one for Fgf8-Cy5 and this could be due to several reasons:

- The secreted Fgf8-EGFP protein was of eukaryotic origin whereas the injected Fgf8-Cy5 protein was produced in bacteria. These two proteins could have different post-translational modifications on them and thus have slightly different uptake and degradation kinetics.
- In the equations we used for fitting the spatial or temporal concentration profiles of Fgf8 (equations 14.1, 14.8 and 14.10), the Fgf8 degradation was assumed to be linearly dependent on the concentration of extracellular morphogens, and the degradation rate k was assumed to be spatially and temporally independent. However, it has been suggested that morphogens can enhance their own degradation via negative feedback loops, causing the degradation rate to be higher than first order, and that this self-enhanced degradation confers robustness of morphogen gradients to fluctuations in their production rates (153). It has been shown that Fgf downstream targets *SPRY4*, *SPRY2* and *SEF* are antagonists for Fgf signalling (130, 154), so it is likely that self-enhanced degradation also occurs for Fgf8. A model including higher order degradation would therefore affect the values of both the inferred half-life of Fgf8-EGFP (deduced from the steady-state solution of equation 14.1 and the measured half-life of Fgf8-Cy5 in equation 14.10). Although our model fit well the measured spatial and temporal concentration profiles (Figs. 14.3 b and 14.4 a), we cannot at the moment rule out more complex types of degradation kinetics.

14.4. Endocytosis controls the morphogen gradient

It was shown in section 14.1 that a stable morphogen gradient was established and maintained only for Fgf8-EGFP, not for the non-interacting secEGFP. Only the presence of a sink for Fgf8 in the target tissue could sustain the shape of its gradient. One mechanism for generating a sink for Fgf8 is by receptor-mediated endocytosis. Changing the level of endocytosis should therefore influence the shape of the concentration gradient. To test this, we overexpressed two proteins, respectively, by injecting their mRNA into the cytoplasm of embryos at one-cell stage.

First, we partially blocked endocytosis by overexpressing a dominant negative version of Dynamin (dnDYN). Dynamin is a GTPase required for the scission of endocytic vesicles from cell membranes (155). Endocytosis of Fgf8-EGFP was reduced in dnDYN-overexpressing embryos (Fig. 14.5), and the gradient of Fgf8-EGFP became much shallower compared to that of the control embryos ($\lambda_{\text{dnDYN}} = (271 \pm 29) \mu\text{m}$, Fig. 14.6).

To test the opposite effect, we overexpressed RAB5c. This is a GTPase required for the fusion of endocytic vesicles with early endosomes (155), hence overexpression should increase endocytosis. The amount of Fgf8-EGFP inside the target cells was increased (Fig. 14.5) and the gradient of Fgf8-EGFP became steeper ($\lambda_{\text{RAB5c}} = (164 \pm 14) \mu\text{m}$; Fig. 14.6). The decrease in the decay length in RAB5c-overexpressing embryos was significant but small, probably owing to other rate-limiting steps in the uptake of Fgf8 upstream or parallel to RAB5c.

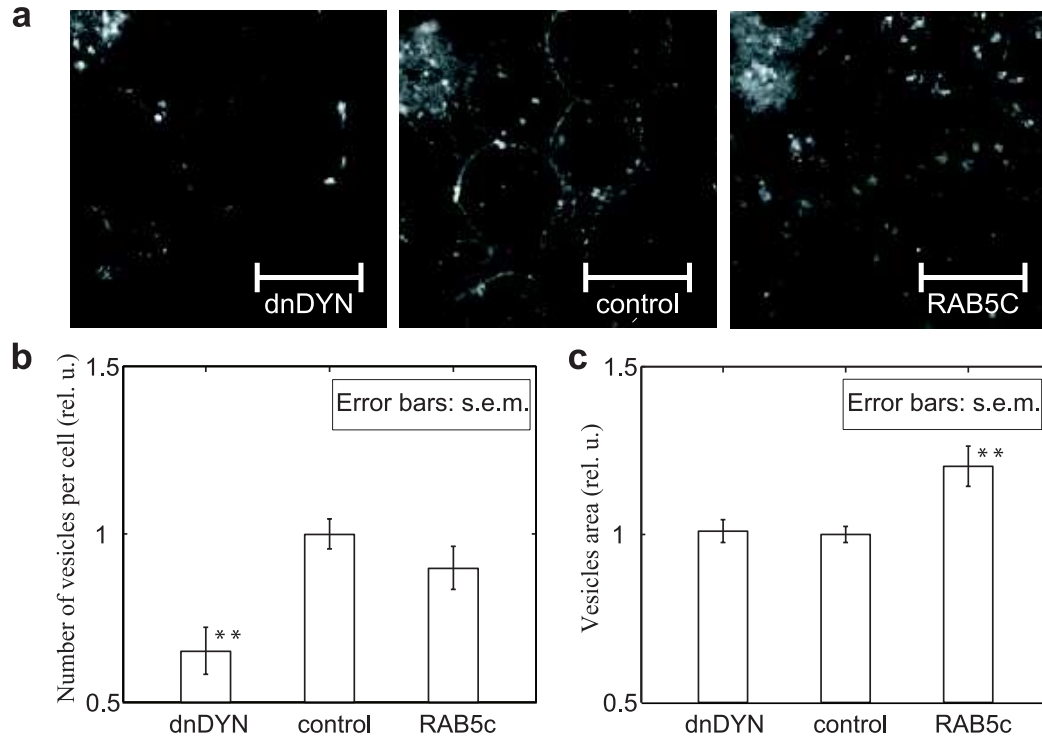


Figure 14.5.: Effect of dominant negative Dynamin and RAB5c on the endocytosis of Fgf8-EGFP into target cells. a: Comparison of uptake of Fgf8-EGFP in dnDYN overexpressing, control and RAB5c overexpressing embryos. The Fgf8-EGFP secreting cells are in the left upper corner. Motiontracking II (156) was used for quantifying the number and the mean area of EGFP vesicles in 5 cells closest to the source of each embryo. Scale bars: 20 μm . **b:** The number of vesicles is significantly decreased in dnDYN overexpressing embryos in comparison to that in the control embryos (the number of vesicles are normalized with respect to the average of the number of vesicles in the control embryos on each day of the experiment) whereas it does not change significantly in RAB5c overexpressing embryos. Control (1.00 ± 0.05) vs. dnDYN (0.65 ± 0.07) vs. RAB5c (0.90 ± 0.06), mean \pm s.e.m., $n = 10$ for control, $n = 7$ for dnDYN embryos and $n = 14$ for RAB5c embryos, $p = 0.0008$ for control vs. dnDYN and $p = 0.2$ for control vs. RAB5c using Student's 2-tailed t-test. **c:** The mean normalized area of the vesicles does not change significantly in dnDYN overexpressing embryos in comparison to that in the control embryos, where it is increased significantly in RAB5c overexpressing embryos. Control (1.00 ± 0.02) vs. dnDYN (1.01 ± 0.03) vs. RAB5c (1.20 ± 0.06), mean \pm s.e.m., $p = 0.8$ for control vs. dnDYN and $p = 0.005$ for control vs. RAB5c using Student's 2-tailed t-test. Altogether, the dnDYN overexpressing embryos have 35% less vesicles in the target cells than the control embryos and no significant change in the mean area of the vesicles. The RAB5c overexpressing embryos have vesicles of 20% more mean area in the target cells than the control embryos and no significant change in the number of the vesicles.

The diffusion coefficient of Fgf8-EGFP in the presence of dnDYN or RAB5c did not differ from the control ($D_{\text{Fgf8-EGFP dnDYN}} = (55 \pm 14) \mu\text{m}^2/\text{s}$, $n = 34$ and $D_{\text{Fgf8-EGFP RAB5c}} = (53 \pm 14) \mu\text{m}^2/\text{s}$, $n = 23$, mean \pm s.d.; Fig. 12.2 d). Therefore, the change in the decay length λ can be attributed to a change in the degradation rate k . The corresponding calculated half life time of the morphogen in the extracellular space was increased to 15 min in dnDYN-overexpressing embryos and decreased to 6 min in RAB5c ones.

14. Exploring the morphogen concentration gradient

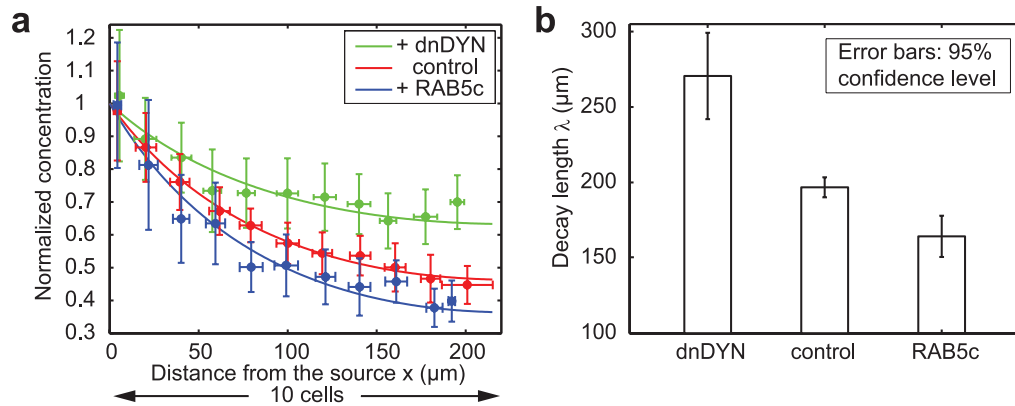


Figure 14.6.: Endocytosis regulates extracellular Fgf8 concentration gradient. **a:** The Fgf8-EGFP concentration gradient becomes shallower in *dnodyn*-injected embryos ($n = 13$) and steeper in *rab5c-cfp*-injected embryos ($n = 12$), compared to the controls ($n = 40$). Error bars denote s.d. **b:** Comparison of the decay length λ in *dnodyn*-, control and *rab5c-cfp*-injected embryos. Error bars denote the 95% confidence level.

These results confirm the prediction of a previously suggested restrictive clearance mechanism (132), in which endocytosis via cell surface receptors acts as a sink for removing Fgf8 protein from the extracellular space. Endocytosis of Fgf8 by its target cells is important for maintaining and shaping its protein gradient in tissue.

Conclusion of part IV

By employing FCS in a live embryo system, we directly measured the molecular dynamics of Fgf8 within its morphogen gradient. We showed that the majority of morphogen molecules diffused as single molecules with a high diffusion coefficient comparable to the one in buffer. A small fraction of molecules moved approximately by factor 10 slower. We could attribute this component to interaction of Fgf8 with the extracellular matrix component HSPG.

Our results support a simple mechanism, involving a localized source, Brownian diffusion through the extracellular space and a sink in the target tissue generated by receptor-mediated endocytosis, to form and maintain a morphogen gradient. The decay length of the gradient could be influenced by altering the rate of endocytosis with biochemical treatments. This study shows the potential of FCS to obtain crucial data such as diffusion coefficients and degradation rates *in vivo*.

Recently, similar applications of FCS to living organisms have been reported (59, 157–160). Protein dynamics were investigated before the asymmetric first cell division in eggs of *Caenorhabditis elegans* (157). In references (158) and (59), dissociation constants were determined in living zebrafish embryos. Thereby, the interaction of proteins could be directly quantified under physiological conditions, and substantial differences were obtained compared to measurements in cell culture (158). In (159), FCS was applied to zebrafish and *Drosophila* embryos. Measurements of blood flow velocities, and diffusion coefficients of eGFP labeled proteins in the cytoplasm and on the membrane were performed. Furthermore, penetration depth was investigated with one and two-photon excitation.

The quantitative information of physical parameters, obtained in such FCS measurements, can serve as a baseline for further experimental and theoretical studies of molecular processes in developmental biology.

Conclusion and outlook

In this thesis, we developed a spatially resolved detection strategy for fluorescence correlation spectroscopy by means of an electron multiplying CCD camera. Two different EMCCD models were tested that showed good results of FCS measurements compared to classical APD point detection. EMCCD detection for FCS required tailored data acquisition concepts and multiple data evaluation steps and corrections of the raw signal, and measurement times were longer due to the sequential readout of the camera. However, these technical limitations were outbalanced by the obvious benefits of a flexible, array-based, parallel data acquisition for FCS.

As a first application, two-focus FCS was demonstrated, largely benefiting from the flexible EMCCD-based detection. Precise diffusion coefficients could be obtained from measurements of different fluorescent molecules in solution, and measurements in a flow channel were performed. The detection sensitivity of small flow velocities within a dominating diffusion could be enhanced by employing two large and overlapping focal volumes with alternating excitation.

FCS was further employed to questions in developmental biology. In living zebrafish embryos, two-focus EMCCD-FCS measurements were performed to explore the propagation mechanism of Fgf8 morphogen molecules. With EMCCD-FCS and standard APD-FCS measurements, the morphogen concentration gradient could be visualized and quantified. From the knowledge of the physical parameters obtained by FCS, the dynamics of morphogen formation and maintenance could be explored.

When this project was started in 2004, EMCCD cameras were on the market for about four years. They were used for imaging but not yet for any FCS applications. The first two reports about EMCCD-FCS were published in 2006 (96, 97).

Thereafter, the number of publications about utilizing EMCCD cameras for FCS has been increasing steadily, and some groups performing FCS with standard point detectors suggest to utilize the advantages of EMCCD-based detection in the future. The analysis of fluorescence fluctuation data from EMCCD detection for molecular brightness measurements has been investigated recently (161).

It can be anticipated that EMCCD technology will develop further towards faster time resolution. Moreover, charge integrating devices as CCDs are only one out of several promising technologies suitable for parallel acquisition. Single-photon counting APD array detectors are constantly developed further towards more detector elements and higher sensitivity. As well, CMOS technology may see a come back into the scientific field. The latest CMOS generation was announced to exhibit a low read noise of only a few electrons, but considerably higher frame rates compared to EMCCDs. It remains exciting to follow which technology will establish itself, to become the standard detector for parallel FCS in the near future.

Bibliography

1. Rigler, R., Ü. Mets, J. Widengren, and P. Kask, 1993. Fluorescence correlation spectroscopy with high count rate and low background: analysis of translational diffusion. *Eur. Biophys. J.* 22:169–175.
2. Bacia, K., S. A. Kim, and P. Schwille, 2006. Fluorescence cross-correlation spectroscopy in living cells. *Nat. Methods* 3:83–89.
3. Rigler, R., and E. S. Elson, 2001. Fluorescence Correlation Spectroscopy: Theory and Applications. Springer series in chemical physics; 65. Springer.
4. Haken, H., and H. C. Wolf, 2003. Molekülphysik und Quantenchemie: Einführung in die experimentellen und theoretischen Grundlagen. Springer.
5. Taylor, A. J., R. B. Gibson, and J. P. Roberts, 1988. Two-photon absorption at 248 nm in ultraviolet window materials. *Opt. Lett.* 13:814–816.
6. Schwille, P., U. Haupts, S. Maiti, and W. W. Webb, 1999. Molecular Dynamics in Living Cells Observed by Fluorescence Correlation Spectroscopy with One- and Two-Photon Excitation. *Biophys. J.* 77:2251–2265.
7. Shaner, N. C., M. Z. Lin, M. R. McKeown, P. A. Steinbach, K. L. Hazelwood, M. W. Davidson, and R. Y. Tsien, 2008. Improving the photostability of bright monomeric orange and red fluorescent proteins. *Nat. Methods* 5:545–551.
8. Hendrix, J., C. Flors, P. Dedecker, J. Hofkens, and Y. Engelborghs, 2008. Dark States in Monomeric Red Fluorescent Proteins Studied by Fluorescence Correlation and Single Molecule Spectroscopy. *Biophys. J.* 94:4103–4113.
9. Michalet, X., F. F. Pinaud, L. A. Bentolila, J. M. Tsay, S. Doose, J. J. Li, G. Sundaresan, A. M. Wu, S. S. Gambhir, and S. Weiss, 2005. Quantum Dots for Live Cells, in Vivo Imaging, and Diagnostics. *Science* 307:538–544.
10. Fu, C.-C., H.-Y. Lee, K. Chen, T.-S. Lim, H.-Y. Wu, P.-K. Lin, P.-K. Wei, P.-H. Tsao, H.-C. Chang, and W. Fann, 2007. Characterization and application of single fluorescent nanodiamonds as cellular biomarkers. *Proc. Natl. Acad. Sci. USA* 104:727–732.
11. Chen, Y., J. Vela, H. Htoon, J. L. Casson, D. J. Werder, D. A. Bussian, V. I. Klimov, and J. A. Hollingsworth, 2008. "Giant" Multishell CdSe Nanocrystal Quantum Dots with Suppressed Blinking. *J. Am. Chem. Soc.* 130:5026–5027.
12. Walling, M. A., J. A. Novak, and J. R. E. Shepard, 2009. Quantum Dots for Live Cell and In Vivo Imaging. *Int. J. Mol. Sci.* 10:441–491.
13. Haustein, E., 2005. Fluorescence fluctuation spectroscopy on freely diffusing and spatially confined single molecules. Ph.D. thesis, TU Dresden.

Bibliography

14. Schwille, P., 1996. Fluoreszenz-Korrelations-Spektroskopie: Analyse biochemischer Systeme auf Einzelmolekülebene. Ph.D. thesis, TU Carolo-Wilhelmina zu Braunschweig.
15. Dertinger, T., V. Pacheco, I. von der Hocht, R. Hartmann, I. Gregor, and J. Enderlein, 2007. Two-Focus Fluorescence Correlation Spectroscopy: A New Tool for Accurate and Absolute Diffusion Measurements. *ChemPhysChem* 8:433–443.
16. Widengren, J., 1996. Fluorescence correlation spectroscopy, photophysical aspects and applications. Ph.D. thesis, KI Stockholm.
17. Kestin, J., M. Sokolov, and W. A. Wakeham, 1978. Viscosity of Liquid Water in the Range -8 °C to 150 °C. *J. Phys. Chem. Ref. Data* 7:941–948.
18. Hess, S. T., and W. W. Webb, 2002. Focal Volume Optics and Experimental Artifacts in Confocal Fluorescence Correlation Spectroscopy. *Biophys. J.* 83:2300–2317.
19. Koppel, D. E., 1974. Statistical accuracy in fluorescence correlation spectroscopy. *Phys. Rev. A* 10:1938–1945.
20. Dittrich, P. S., and P. Schwille, 2001. Photobleaching and stabilization of fluorophores used for single-molecule analysis with one- and two-photon excitation. *Appl. Phys. B* 73:829–837.
21. Widengren, J., and R. Rigler, 1996. Mechanisms of photobleaching investigated by fluorescence correlation spectroscopy. *Bioimaging* 4:149–157.
22. Nishimura, G., and M. Kinjo, 2004. Systematic Error in Fluorescence Correlation Measurements Identified by a Simple Saturation Model of Fluorescence. *Anal. Chem.* 76:1963–1970.
23. Nagy, A., J. Wu, and K. M. Berland, 2005. Characterizing observation volumes and the role of excitation saturation in one-photon fluorescence fluctuation spectroscopy. *J. Biomed. Opt.* 10:44015.
24. Davis, L. M., and G. Shen, 2006. Accounting for Triplet and Saturation Effects in FCS Measurements. *Curr. Pharm. Biotechnol.* 7:287–301.
25. Meseth, U., T. Wohland, R. Rigler, and H. Vogel, 1999. Resolution of Fluorescence Correlation Measurements. *Biophys. J.* 76:1619–1631.
26. Widengren, J., Ü. Mets, and R. Rigler, 1995. Fluorescence Correlation Spectroscopy of Triplet States in Solution: A Theoretical and Experimental Study. *J. Phys. Chem.* 99:13368–13379.
27. Haupts, U., S. Maiti, P. Schwille, and W. W. Webb, 1998. Dynamics of fluorescence fluctuations in green fluorescent protein observed by fluorescence correlation spectroscopy. *Proc. Natl. Acad. Sci. USA* 95:13573–13578.
28. Enderlein, J., I. Gregor, D. Patra, and J. Fitter, 2004. Art and Artefacts of Fluorescence Correlation Spectroscopy. *Curr. Pharm. Biotechnol.* 5:155–161.
29. Enderlein, J., I. Gregor, D. Patra, T. Dertinger, and U. B. Kaupp, 2005. Performance of Fluorescence Correlation Spectroscopy for Measuring Diffusion and Concentration. *ChemPhysChem* 6:2324–2336.
30. Dertinger, T., A. Loman, B. Ewers, C. B. Müller, B. Krämer, and J. Enderlein, 2008. The optics and performance of dual-focus fluorescence correlation spectroscopy. *Opt. Express* 16:14353–14368.

31. Ries, J., 2008. Advanced Fluorescence Correlation Techniques to Study Membrane Dynamics. Ph.D. thesis, TU Dresden.
32. Enderlein, J., and I. Gregor, 2005. Using fluorescence lifetime for discriminating detector after-pulsing in fluorescence-correlation spectroscopy. *Rev. Sci. Instrum.* 76:033102.
33. Nagy, A., J. Wu, and K. M. Berland, 2005. Observation Volumes and γ -Factors in Two-Photon Fluorescence Fluctuation Spectroscopy. *Biophys. J.* 89:2077–2090.
34. Berland, K., and G. Shen, 2003. Excitation saturation in two-photon fluorescence correlation spectroscopy. *Appl. Optics* 42:5566–5576.
35. Loman, A., T. Dertinger, F. Koberling, and J. Enderlein, 2008. Comparison of optical saturation effects in conventional and dual-focus fluorescence correlation spectroscopy. *Chemical Physics Letters* 459:18–21.
36. Schwille, P., F.-J. Meyer-Almes, and R. Rigler, 1997. Dual-Color Fluorescence Cross-Correlation Spectroscopy for Multicomponent Diffusional Analysis in Solution. *Biophys. J.* 72:1878–1886.
37. Weidemann, T., M. Wachsmuth, M. Tewes, K. Rippe, and J. Langowski, 2002. Analysis of Ligand Binding by Two-Colour Fluorescence Cross-Correlation Spectroscopy. *Single Mol.* 3:49–61.
38. Bacia, K., 2005. Dynamic Processes in Membranes Studied by Fluorescence Correlation Spectroscopy. Ph.D. thesis, TU Dresden.
39. Heinze, K. G., A. Koltermann, and P. Schwille, 2000. Simultaneous two-photon excitation of distinct labels for dual-color fluorescence crosscorrelation analysis. *Proc. Natl. Acad. Sci. USA* 97:10377–10382.
40. Brinkmeier, M., K. Dörre, J. Stephan, and M. Eigen, 1999. Two-Beam Cross-Correlation: A Method To Characterize Transport Phenomena in Micrometer-Sized Structures. *Anal. Chem.* 71:609–616.
41. Müller, C. B., K. Weiß, W. Richtering, A. Loman, and J. Enderlein, 2008. Calibrating Differential Interference Contrast Microscopy with dual-focus Fluorescence Correlation Spectroscopy. *Opt. Express* 16:4322–4329.
42. Felten, M., W. Staroske, M. S. Jaeger, P. Schwille, and C. Duschl, 2008. Accumulation and filtering of nanoparticles in microchannels using electrohydrodynamically induced vortical flows. *Electrophoresis* 29:2987–2996.
43. Müller, B. K., E. Zaychikov, C. Bräuchle, and D. C. Lamb, 2005. Pulsed Interleaved Excitation. *Biophys. J.* 89:3508–3522.
44. Thews, E., M. Gerken, R. Eckert, J. Zäpfel, C. Tietz, and J. Wrachtrup, 2005. Cross Talk Free Fluorescence Cross Correlation Spectroscopy in Live Cells. *Biophys. J.* 89:2069–2076.
45. Thonig, D., 2008. Zwei-Fokus Fluoreszenz-Korrelations-Spektroskopie. Diploma thesis, TU Dresden.
46. Korlann, Y., T. Dertinger, X. Michalet, S. Weiss, and J. Enderlein, 2008. Measuring diffusion with polarization-modulation dual-focus fluorescence correlation spectroscopy. *Opt. Express* 16:14609–14616.

Bibliography

47. Ries, J., and P. Schwille, 2006. Studying Slow Membrane Dynamics with Continuous Wave Scanning Fluorescence Correlation Spectroscopy. *Biophys. J.* 91:1915–1924.
48. Thompson, N. L., 1991. Topics in Fluorescence Spectroscopy, Vol. 1: Techniques, Plenum Press, chapter Fluorescence Correlation Spectroscopy, 337.
49. Aragón, S. R., and R. Pecora, 1975. Fluorescence Correlation Spectroscopy and Brownian Rotational Diffusion. *Biopolymers* 14:119–138.
50. Gösch, M., H. Blom, J. Holm, T. Heino, and R. Rigler, 2000. Hydrodynamic Flow Profiling in Microchannel Structures by Single Molecule Fluorescence Correlation Spectroscopy. *Anal. Chem.* 72:3260–3265.
51. Widengren, J., and R. Rigler, 1998. Fluorescence Correlation Spectroscopy as a Tool to Investigate Chemical Reactions in Solutions and on Cell Surfaces. *Cell. Mol. Biology* 44:857–878.
52. Wohland, T., K. Friedrich, R. Hovius, and H. Vogel, 1999. Study of Ligand-Receptor Interactions by Fluorescence Correlation Spectroscopy with Different Fluorophores: Evidence That the Homopentameric 5-Hydroxytryptamine Type 3(As) Receptor Binds Only One Ligand. *Biochemistry* 38:8671–8681.
53. Kettling, U., A. Koltermann, P. Schwille, and M. Eigen, 1998. Real-time enzyme kinetics monitored by dual-color fluorescence cross-correlation spectroscopy. *Proc. Natl. Acad. Sci. USA* 95:1416–1420.
54. Jahnz, M., and P. Schwille, 2005. An ultrasensitive site-specific DNA recombination assay based on dual-color fluorescence cross-correlation spectroscopy. *Nucleic Acids Res.* 33:e60.
55. Bacia, K., C. G. Schuette, N. Kahya, R. Jahn, and P. Schwille, 2004. SNAREs Prefer Liquid-disordered over "Raft" (Liquid-ordered) Domains When Reconstituted into Giant Unilamellar Vesicles. *J. Biol. Chem.* 279:37951–37955.
56. Bacia, K., I. V. Majoul, and P. Schwille, 2002. Probing the Endocytic Pathway in Live Cells Using Dual-Color Fluorescence Cross-Correlation Analysis. *Biophys. J.* 83:1184–1193.
57. Slaughter, B. D., J. W. Schwartz, and R. Li, 2007. Mapping dynamic protein interactions in MAP kinase signaling using live-cell fluorescence fluctuation spectroscopy and imaging. *Proc. Natl. Acad. Sci. USA* 104:20320–20325.
58. Ohrt, T., J. Mütze, W. Staroske, L. Weinmann, J. Höck, K. Crell, G. Meister, and P. Schwille, 2008. Fluorescence correlation spectroscopy and fluorescence cross-correlation spectroscopy reveal the cytoplasmic origination of loaded nuclear RISC in vivo in human cells. *Nucleic Acids Res.* 36:6439–6449.
59. Ries, J., S. R. Yu, M. Burkhardt, M. Brand, and P. Schwille, 2009. Modular scanning FCS quantifies receptor-ligand interactions in living multicellular organisms. *Nat. Methods* 6:643–645.
60. Hwang, L. C., and T. Wohland, 2004. Dual-Color Fluorescence Cross-Correlation Spectroscopy Using Single Laser Wavelength Excitation. *ChemPhysChem* 5:549–551.
61. Hwang, L. C., and T. Wohland, 2005. Single wavelength excitation fluorescence cross-correlation spectroscopy with spectrally similar fluorophores: Resolution for binding studies. *J. Chem. Phys.* 122:114708.

62. Hwang, L. C., and T. Wohland, 2007. Recent Advances in Fluorescence Cross-correlation Spectroscopy. *Cell Biochem. Biophys.* 49:1–13.
63. Hwang, L. C., M. Gösch, T. Lasser, and T. Wohland, 2006. Simultaneous Multicolor Fluorescence Cross-Correlation Spectroscopy to Detect Higher Order Molecular Interactions Using Single Wavelength Laser Excitation. *Biophys. J.* 91:715–727.
64. Heinze, K. G., M. Jahnz, and P. Schwille, 2004. Triple-Color Coincidence Analysis: One Step Further in Following Higher Order Molecular Complex Formation. *Biophys. J.* 86:506–516.
65. Burkhardt, M., K. G. Heinze, and P. Schwille, 2005. Four-color fluorescence correlation spectroscopy realized in a grating-based detection platform. *Opt. Lett.* 30:2266–2268.
66. Hwang, L. C., M. Leutenegger, M. Gösch, T. Lasser, P. Rigler, W. Meier, and T. Wohland, 2006. Prism-based multicolor fluorescence correlation spectrometer. *Opt. Lett.* 31:1310–1312.
67. Michalet, X., O. H. W. Siegmund, J. V. Vallerga, P. Jelinsky, J. E. Millaud, and S. Weiss, 2007. Detectors for single-molecule fluorescence imaging and spectroscopy. *J. Mod. Opt.* 54:239–281.
68. Luong, A. K., C. C. Gradinaru, D. W. Chandler, and C. C. Hayden, 2005. Simultaneous Time- and Wavelength-Resolved Fluorescence Microscopy of Single Molecules. *J. Phys. Chem. B* 109:15691–15698.
69. Lansford, R., G. Bearman, and S. E. Fraser, 2001. Resolution of multiple green fluorescent protein color variants and dyes using two-photon microscopy and imaging spectroscopy. *J. Biomed. Opt.* 6:311–318.
70. Dickinson, M. E., G. Bearman, S. Tille, R. Lansford, and S. E. Fraser, 2001. Multi-Spectral Imaging and Linear Unmixing Add a Whole New Dimension to Laser Scanning Fluorescence Microscopy. *Biotechniques* 31:1272, 1274–6, 1278.
71. Sinclair, M. B., J. A. Timlin, D. M. Haaland, and M. Werner-Washburne, 2004. Design, construction, characterization, and application of a hyperspectral microarray scanner. *Appl. Opt.* 43:2079–2088.
72. Frederix, P. L. T. M., M. A. H. Asselbergs, W. G. J. H. M. Van Sark, D. J. Van den Heuvel, W. Hamelink, E. L. D. Beer, and H. C. Gerritsen, 2001. High Sensitivity Spectrograph for Use in Fluorescence Microscopy. *Appl. Spectrosc.* 55:1005–1012.
73. Suzuki, Y., T. Tani, K. Sutoh, and S. Kamimura, 2002. Imaging of the fluorescence spectrum of a single fluorescent molecule by prism-based spectroscopy. *FEBS Lett.* 512:235–239.
74. Adams, M. C., W. C. Salmon, S. L. Gupton, C. S. Cohan, T. Wittmann, N. Prigozhina, and C. M. Waterman-Storer, 2003. A high-speed multispectral spinning-disk confocal microscope system for fluorescent speckle microscopy of living cells. *Methods* 29:29–41.
75. Dickinson, M. E., C. W. Waters, G. H. Bearman, R. Wolleschensky, S. Tille, and S. E. Fraser, 2002. Sensitive imaging of spectrally overlapping fluorochromes using the LSM 510 META. *Proc. SPIE* 4620:123–136.
76. Birk, H., J. Engelhardt, R. Storz, N. Hartmann, J. Bradl, and H. Ulrich, 2002. Programmable beam-splitter for confocal laser scanning microscopy. *Proc. SPIE* 4621:16–27.

Bibliography

77. Previte, M. J. R., S. Pelet, K. H. Kim, C. Buehler, and P. T. C. So, 2008. Spectrally Resolved Fluorescence Correlation Spectroscopy Based on Global Analysis. *Anal. Chem.* 80:3277–3284.
78. Restelli, A., I. Rech, P. Maccagnani, M. Ghioni, and S. Cova, 2007. Monolithic silicon matrix detector with 50 μm photon counting pixels. *J. Mod. Opt.* 54:213–223.
79. Rech, I., S. Marangoni, D. Resnati, M. Ghioni, and S. Cova, 2009. Multipixel single-photon avalanche diode array for parallel photon counting applications. *J. Mod. Opt.* 56:326–333.
80. Blazej, J., I. Prochazka, K. Hamal, B. Sopko, and D. Chren, 2006. Gallium-based avalanche photodiode optical crosstalk. *Nucl. Instrum. Meth. A* 567:239–241.
81. Zappa, F., S. Tisa, S. Cova, P. Maccagnani, R. Saletti, and R. Roncella, 2005. Single-photon imaging at 20,000 frames/s. *Opt. Lett.* 30:3024–3026.
82. Köhler, R. H., P. Schwille, W. W. Webb, and M. R. Hanson, 2000. Active protein transport through plastid tubules: velocity quantified by fluorescence correlation spectroscopy. *J. Cell Sci.* 113:3921–3930.
83. Müller, C. B., A. Loman, V. Pacheco, F. Koberling, D. Willbold, W. Richtering, and J. Enderlein, 2008. Precise measurement of diffusion by multi-color dual-focus fluorescence correlation spectroscopy. *Europhys. Lett.* 83:46001.
84. Blom, H., M. Johansson, A.-S. Hedman, L. Lundberg, A. Hanning, S. Hård, and R. Rigler, 2002. Parallel fluorescence detection of single biomolecules in microarrays by a diffractive-optical-designed 2 x 2 fan-out element. *Appl. Opt.* 41:3336–3342.
85. Blom, H., M. Johansson, M. Gösch, T. Sigmundsson, J. Holm, S. Hård, and R. Rigler, 2002. Parallel flow measurements in microstructures by use of a multifocal 4 x 1 diffractive optical fan-out element. *Appl. Opt.* 41:6614–6620.
86. Ohsugi, Y., and M. Kinjo, 2009. Multipoint fluorescence correlation spectroscopy with total internal reflection fluorescence microscope. *J. Biomed. Opt.* 14:014030.
87. Gösch, M., A. Serov, T. Anhut, T. Lasser, A. Rochas, P.-A. Besse, R. S. Popovic, H. Blom, and R. Rigler, 2004. Parallel single molecule detection with a fully integrated single-photon 2x2 CMOS detector array. *J. Biomed. Opt.* 9:913–921.
88. Dittrich, P. S., and P. Schwille, 2002. Spatial Two-Photon Fluorescence Cross-Correlation Spectroscopy for Controlling Molecular Transport in Microfluidic Structures. *Anal. Chem.* 74:4472–4479.
89. LeCaptain, D. J., and A. V. Orden, 2002. Two-Beam Fluorescence Cross-Correlation Spectroscopy in an Electrophoretic Mobility Shift Assay. *Anal. Chem.* 74:1171–1176.
90. Jaffiol, R., Y. Blancquaert, A. Delon, and J. Derouard, 2006. Spatial fluorescence cross-correlation spectroscopy. *Appl. Opt.* 45:1225–1235.
91. Blancquaert, Y., A. Delon, J. Derouard, and R. Jaffiol, 2006. Spatial fluorescence cross-correlation spectroscopy between core and ring pinholes. In R. Grzymala, and O. Haeberlé, editors, *Biophotonics and New Therapy Frontiers*. Proc. of SPIE, volume 6191, 61910B1–61910B9.

92. Didier, P., J. Godet, and Y. Mély, 2009. Two-Photon Two-Focus Fluorescence Correlation Spectroscopy with a Tunable Distance Between the Excitation Volumes. *J. Fluoresc.* 19:561–565.
93. Blancquaert, Y., J. Gao, J. Derouard, and A. Delon, 2008. Spatial fluorescence cross-correlation spectroscopy by means of a spatial light modulator. *J. Biophoton.* 1:408–418.
94. Ferrand, P., M. Pianta, A. Kress, A. Aillaud, H. Rigneault, and D. Marguet, 2009. A versatile dual spot laser scanning confocal microscopy system for advanced fluorescence correlation spectroscopy analysis in living cell. *Rev. Sci. Instrum.* 80:083702.
95. Robbins, M. S., and B. J. Hadwen, 2003. The Noise Performance of Electron Multiplying Charge-Coupled Devices. *IEEE Trans. Electron Dev.* 50:1227–1232.
96. Kannan, B., J. Y. Har, P. Liu, I. Maruyama, J. L. Ding, and T. Wohland, 2006. Electron Multiplying Charge-Coupled Device Camera Based Fluorescence Correlation Spectroscopy. *Anal. Chem.* 78:3444–3451.
97. Burkhardt, M., and P. Schwille, 2006. Electron multiplying CCD based detection for spatially resolved fluorescence correlation spectroscopy. *Opt. Express* 14:5013–5020.
98. Sisan, D. R., R. Arevalo, C. Graves, R. McAllister, and J. S. Urbach, 2006. Spatially Resolved Fluorescence Correlation Spectroscopy Using a Spinning Disk Confocal Microscope. *Biophys. J.* 91:4241–4252.
99. Needleman, D. J., Y. Xu, and T. J. Mitchison, 2009. Pin-Hole Array Correlation Imaging: Highly Parallel Fluorescence Correlation Spectroscopy. *Biophys. J.* 96:5050–5059.
100. Hashmi, S. M., M. Loewenberg, and E. R. Dufresne, 2007. Spatially extended FCS for visualizing and quantifying high-speed multiphase flows in microchannels. *Opt. Express* 15:6528–6533.
101. Kannan, B., L. Guo, T. Sudhaharan, S. Ahmed, I. Maruyama, and T. Wohland, 2007. Spatially Resolved Total Internal Reflection Fluorescence Correlation Microscopy Using an Electron Multiplying Charge-Coupled Device Camera. *Anal. Chem.* 79:4463–4470.
102. Sankaran, J., M. Manna, L. Guo, R. Kraut, and T. Wohland, 2009. Diffusion, Transport, and Cell Membrane Organization Investigated by Imaging Fluorescence Cross-Correlation Spectroscopy. *Biophys. J.* 97:2630–2639.
103. Matsumoto, M., T. Sugiura, and K. Minato, 2007. Spatially resolved fluorescence correlation spectroscopy based on electron multiplying CCD. In Wilson, T and Periasamy, A, editor, Confocal, Multiphoton, and Nonlinear Microscopic Imaging III. volume 6630 of *Proc. SPIE*, 63017.
104. Wohland, T., X. Shi, J. Sankaran, and E. H. K. Stelzer, 2010. Single Plane Illumination Fluorescence Correlation Spectroscopy (SPIM-FCS) probes inhomogeneous three-dimensional environments. *Opt. Express* 18:10627–10641.
105. Petersen, N. O., P. L. Höddelius, P. W. Wiseman, O. Seger, and K.-E. Magnusson, 1993. Quantitation of Membrane Receptor Distributions by Image Correlation Spectroscopy: Concept and Application. *Biophys. J.* 65:1135–1146.
106. Wiseman, P. W., and N. O. Petersen, 1999. Image Correlation Spectroscopy. II. Optimization for Ultrasensitive Detection of Preexisting Platelet-Derived Growth Factor- β Receptor Oligomers on Intact Cells. *Biophys. J.* 76:963–977.

Bibliography

107. Wiseman, P. W., C. M. Brown, D. J. Webb, B. Hebert, N. L. Johnson, J. A. Squier, M. H. Ellisman, and A. F. Horwitz, 2004. Spatial mapping of integrin interactions and dynamics during cell migration by Image Correlation Microscopy. *J. Cell Sci.* 117:5521–5534.
108. Kolin, D. L., D. Ronis, and P. W. Wiseman, 2006. k-Space Image Correlation Spectroscopy: A Method for Accurate Transport Measurements Independent of Fluorophore Photophysics. *Biophys. J.* 91:3061–3075.
109. Digman, M. A., P. Sengupta, P. W. Wiseman, C. M. Brown, A. R. Horwitz, and E. Gratton, 2005. Fluctuation Correlation Spectroscopy with a Laser-Scanning Microscope: Exploiting the Hidden Time Structure. *Biophys. J.* 88:L33–36.
110. Digman, M. A., C. M. Brown, P. Sengupta, P. W. Wiseman, A. R. Horwitz, and E. Gratton, 2005. Measuring Fast Dynamics in Solutions and Cells with a Laser Scanning Microscope. *Biophys. J.* 89:1317–1327.
111. Hebert, B., S. Costantino, and P. W. Wiseman, 2005. Spatiotemporal Image Correlation Spectroscopy (STICS) Theory, Verification, and Application to Protein Velocity Mapping in Living CHO Cells. *Biophys. J.* 88:3601–3614.
112. Petersen, N. O., 1986. Scanning Fluorescence Correlation Spectroscopy. I. Theory and Simulation of Aggregation Measurements. *Biophys. J.* 49:809–815.
113. Pan, X., H. Yu, X. Shi, V. Korzh, and T. Wohland, 2007. Characterization of flow direction in microchannels and zebrafish blood vessels by scanning fluorescence correlation spectroscopy. *J. Biomed. Opt.* 12:014034.
114. Ries, J., S. Chiantia, and P. Schwille, 2009. Accurate Determination of Membrane Dynamics with Line-Scan FCS. *Biophys. J.* 96:1999–2008.
115. Berland, K. M., P. T. C. So, Y. Chen, W. W. Mantulin, and E. Gratton, 1996. Scanning Two-Photon Fluctuation Correlation Spectroscopy: Particle Counting Measurements for Detection of Molecular Aggregation. *Biophys. J.* 71:410–420.
116. Petrášek, Z., and P. Schwille, 2008. Precise Measurement of Diffusion Coefficients using Scanning Fluorescence Correlation Spectroscopy. *Biophys. J.* 94:1437–1448.
117. Mackay, C. D., R. N. Tubbs, R. Bell, D. J. Burt, P. Jerram, and I. Moody, 2001. Sub-Electron Read Noise at MHz Pixel Rates. In M. M. Blouke, J. Canosa, and N. Sampat, editors, *Sensors and Camera Systems for Scientific, Industrial, and Digital Photography Applications II*. volume 4306 of *Proc. SPIE*, 289–298.
118. Zhang, L., L. Neves, J. S. Lundeen, and I. A. Walmsley, 2009. A characterization of the single-photon sensitivity of an electron multiplying charge-coupled device. *J. Phys. B: At. Mol. Opt. Phys.* 42:114011.
119. Basden, A. G., C. A. Haniff, and C. D. Mackay, 2003. Photon counting strategies with low-light-level CCDs. *Mon. Not. R. Astron. Soc.* 345:985–991.
120. Bachir, A. I., D. L. Kolin, K. G. Heinze, B. Hebert, and P. W. Wiseman, 2008. A guide to accurate measurement of diffusion using fluorescence correlation techniques with blinking quantum dot nanoparticle labels. *J. Chem. Phys.* 128:225105.

121. Roundy, C. B., 1997. CCD camera baseline calibration and its effects on imaging processing and laser beam analysis. *SPIE*, volume 3110, 860–879.
122. Culbertson, C. T., S. C. Jacobson, and J. M. Ramsey, 2002. Diffusion coefficient measurements in microfluidic devices. *Talanta* 56:365–373.
123. Chiantia, S., N. Kahya, and P. Schwille, 2005. Dehydration Damage of Domain-Exhibiting Supported Bilayers: An AFM Study on the Protective Effects of Disaccharides and Other Stabilizing Substances. *Langmuir* 21:6317–6323.
124. Yu, S. R., 2009. Biophysical characterization of fibroblast growth factor 8 signalling and morphogen gradient formation in vivo. Ph.D. thesis, TU Dresden.
125. Wolpert, L., 1969. Positional Information and the Spatial Pattern of Cellular Differentiation. *J. Theor. Biol.* 25:1–47.
126. Tabata, T., and Y. Takei, 2004. Morphogens, their identification and regulation. *Development* 131:703–712.
127. Reifers, F., H. Böhli, E. C. Walsh, P. H. Crossley, D. Y. R. Stainier, and M. Brand, 1998. Fgf8 is mutated in zebrafish acerebellar (ace) mutants and is required for maintenance of midbrain-hindbrain boundary development and somitogenesis. *Development* 125:2381–2395.
128. Reifers, F., E. C. Walsh, S. Léger, D. Y. R. Stainier, and M. Brand, 2000. Induction and differentiation of the zebrafish heart requires fibroblast growth factor 8 (fgf8/acerebellar). *Development* 127:225–235.
129. Goldfarb, M., 1996. Functions of Fibroblast Growth Factors in Vertebrate Development. *Cytokine Growth Factor Rev.* 7:311–325.
130. Fürthauer, M., F. Reifers, M. Brand, B. Thisse, and C. Thisse, 2001. sprouty4 acts in vivo as a feedback-induced antagonist of FGF signaling in zebrafish. *Development* 128:2175–2186.
131. Raible, F., and M. Brand, 2001. Tight transcriptional control of the ETS domain factors Erm and Pea3 by Fgf signaling during early zebrafish development. *Mech. Dev.* 107:105–117.
132. Scholpp, S., and M. Brand, 2004. Endocytosis Controls Spreading and Effective Signaling Range of Fgf8 Protein. *Curr. Biol.* 14:1834–1841.
133. Crick, F., 1970. Diffusion in Embryogenesis. *Nature* 225:420–422.
134. Kerszberg, M., and L. Wolpert, 1998. Mechanisms for Positional Signalling by Morphogen Transport: a Theoretical Study. *J. Theor. Biol.* 191:103–114.
135. Entchev, E. V., A. Schwabedissen, and M. González-Gaitán, 2000. Gradient Formation of the TGF- β Homolog Dpp. *Cell* 103:981–991.
136. Strigini, M., and S. M. Cohen, 2000. Wingless gradient formation in the Drosophila wing. *Curr. Biol.* 10:293–300.
137. McDowell, N., J. B. Gurdon, and D. J. Grainger, 2001. Formation of a functional morphogen gradient by a passive process in tissue from the early Xenopus embryo. *Int. J. Dev. Biol.* 45:199–207.

Bibliography

138. Gregor, T., W. Bialek, R. R. de Ruyter van Steveninck, D. W. Tank, and E. F. Wieschaus, 2005. Diffusion and scaling during early embryonic pattern formation. *Proc. Natl. Acad. Sci. USA* 102:18403–18407.
139. Lander, A. D., 2007. Morpheus Unbound: Reimagining the Morphogen Gradient. *Cell* 128:245–256.
140. Kicheva, A., P. Pantazis, T. Bollenbach, Y. Kalaidzidis, T. Bittig, F. Jülicher, and M. González-Gaitán, 2007. Kinetics of Morphogen Gradient Formation. *Science* 315:521–525.
141. Gregor, T., E. F. Wieschaus, A. P. McGregor, W. Bialek, and D. W. Tank, 2007. Stability and Nuclear Dynamics of the Bicoid Morphogen Gradient. *Cell* 130:141–152.
142. Boldajipour, B., H. Mahabaleshwar, E. Kardash, M. Reichman-Fried, H. Blaser, S. Minina, D. Wilson, Q. Xu, and E. Raz, 2008. Control of Chemokine-Guided Cell Migration by Ligand Sequestration. *Cell* 132:463–473.
143. Magde, D., E. L. Elson, and W. W. Webb, 1974. Fluorescence Correlation Spectroscopy. II. An Experimental Realization. *Biopolymers* 13:29–61.
144. Panchuk-Voloshina, N., R. P. Haugland, J. Bishop-Stewart, M. K. Bhalgat, P. J. Millard, F. Mao, W.-Y. Leung, and R. P. Haugland, 1999. Alexa Dyes, a Series of New Fluorescent Dyes that Yield Exceptionally Bright, Photostable Conjugates. *J. Histochem. Cytochem.* 47:1179–1188.
145. Tsien, R. Y., 1998. The green fluorescent protein. *Annu. Rev. Biochem.* 67:509–544.
146. Shaner, N. C., P. A. Steinbach, and R. Y. Tsien, 2005. A guide to choosing fluorescent proteins. *Nat. Methods* 2:905–909.
147. Amaya, E., T. J. Musci, and M. W. Kirschner, 1991. Expression of a Dominant Negative Mutant of the FGF Receptor Disrupts Mesoderm Formation in *Xenopus* Embryos. *Cell* 66:257–270.
148. Yu, S. R., M. Burkhardt, M. Nowak, J. Ries, Z. Petrášek, S. Scholpp, P. Schwill, and M. Brand, 2009. Fgf8 morphogen gradient forms by a source-sink mechanism with freely diffusing molecules. *Nature* 461:533–536.
149. Petrov, E. P., T. Ohrt, R. G. Winkler, and P. Schwill, 2006. Diffusion and Segmental Dynamics of Double-Stranded DNA. *Phys. Rev. Lett.* 97:258101.
150. Hou, S., M. Maccarana, T. H. Min, I. Strate, and E. M. Pera, 2007. The Secreted Serine Protease xHtrA1 Stimulates Long-Range FGF Signaling in the Early *Xenopus* Embryo. *Dev. Cell* 13:226–241.
151. Baeg, G.-H., E. M. Selva, R. M. Goodman, R. Dasgupta, and N. Perrimon, 2004. The Wingless morphogen gradient is established by the cooperative action of Frizzled and Heparan Sulfate Proteoglycan receptors. *Dev. Biol.* 276:89–100.
152. Desai, U. R., H.-m. Wang, and R. J. Linhardt, 1993. Substrate Specificity of the Heparin Lyases from *Flavobacterium heparinum*. *Arch. Biochem. Biophys.* 306:461–468.
153. Eldar, A., D. Rosin, B.-Z. Shilo, and N. Barkai, 2003. Self-Enhanced Ligand Degradation Underlies Robustness of Morphogen Gradients. *Dev. Cell* 5:635–646.
154. Fürthauer, M., W. Lin, S.-L. Ang, B. Thisse, and C. Thisse, 2002. Sef is a feedback-induced antagonist of Ras/MAPK-mediated FGF signalling. *Nat. Cell Biol.* 4:170–174.

155. Robinson, M. S., C. Watts, and M. Zerial, 1996. Membrane Dynamics in Endocytosis. *Cell* 84:13–21.
156. Rink, J., E. Ghigo, Y. Kalaidzidis, and M. Zerial, 2005. Rab Conversion as a Mechanism of Progression from Early to Late Endosomes. *Cell* 122:735–749.
157. Petrášek, Z., C. Hoege, A. Mashaghi, T. Ohrt, A. A. Hyman, and P. Schwille, 2008. Characterization of Protein Dynamics in Asymmetric Cell Division by Scanning Fluorescence Correlation Spectroscopy. *Biophys. J.* 95:5476–5486.
158. Shi, X., Y. H. Foo, T. Sudhakaran, S.-W. Chong, V. Korzh, S. Ahmed, and T. Wohland, 2009. Determination of Dissociation Constants in Living Zebrafish Embryos with Single Wavelength Fluorescence Cross-Correlation Spectroscopy. *Biophys. J.* 97:678–686.
159. Shi, X., L. S. Teo, X. Pan, S.-W. Chong, R. Kraut, V. Korzh, and T. Wohland, 2009. Probing Events with Single Molecule Sensitivity in Zebrafish and Drosophila Embryos by Fluorescence Correlation Spectroscopy. *Dev. Dyn.* 238:3156–3167.
160. Heuvelman, G., F. Erdel, M. Wachsmuth, and K. Rippe, 2009. Analysis of protein mobilities and interactions in living cells by multifocal fluorescence fluctuation microscopy. *Eur. Biophys. J.* 38:813–828.
161. Unruh, J. R., and E. Gratton, 2008. Analysis of Molecular Concentration and Brightness from Fluorescence Fluctuation Data with an Electron Multiplied CCD Camera. *Biophys. J.* 95:5385–5398.

Symbols and Abbreviations

Symbols

$\langle \cdot \rangle$	arithmetic mean over time T
a	confocal aperture radius in the object space
α	detection angle of the fluorescence
α	angle between distance and flow vector
$B(t)$	background intensity over time
C	concentration
$\delta I(t)$	deviation from mean intensity value $\langle I(t) \rangle$
δ	focus angle of the laser beam
D	diffusion coefficient
d	distance between two foci
η_0	molecular brightness: $\eta_0 = \kappa \cdot \sigma \cdot q \cdot I_0$
η_{eff}	effective molecular brightness: $\eta_{\text{eff}} = \langle I \rangle / N$
η	viscosity of the fluid
F	fraction of fast component
$G(\tau)$	normalized autocorrelation function
$G_{ij}(\tau)$	normalized cross-correlation function
$g_{ij}(\tau)$	non-normalized cross-correlation function
$I(t)$	fluorescence intensity over time
I_0	maximum center excitation intensity
$I_{\text{ex}}(\vec{r})$	spatial profile of excitation intensity
j	morphogen current across source boundary
κ	detection efficiency of the setup
$\kappa(z)$	amplitude function in generalized Gauss-Lorentz model for the excitation profile
k	degradation rate of the morphogen
k_b	Boltzmann's constant
λ	wavelength
λ	decay length of the morphogen gradient
N	number of particles in V_{eff}
n	index of refraction
$\phi(\vec{r}, \vec{r}', \tau)$	concentration correlation function
q	fluorescence quantum yield
\vec{R}	distance between two foci
\vec{r}	spatial coordinate

$R(z)$	axial point spread function dependence in generalized Gauss-Lorentz model for the excitation profile
r	hydrodynamic radius
r_0	radius of the morphogen source
r_1	radius of the target tissue
σ	absorption cross-section
S	structure parameter: $S = z_0 / \omega_0$
$S(\vec{r})$	optical transfer function of the setup
τ	lag time
ϑ	temperature in degree Celsius
T	absolute temperature in Kelvin
T	measurement time
T	triplet fraction
t	time
$t_{0.5}$	half-life time of morphogen
τ_D	diffusion time
τ_T	triplet blinking time
\vec{v}	flow velocity
V_{eff}	effective detection volume
$W(\vec{r})$	molecule detection function
$w(z)$	width function in generalized Gauss-Lorentz model for the excitation profile
ω_0	lateral $1/e^2$ -radius of a focused Gaussian beam
z_0	axial $1/e^2$ -radius

Abbreviations

AC	Autocorrelation curve
ADC	Analog-to-digital conversion
AOM	Acousto optical modulator
APD	Avalanche photo diode
BF	Bandpass filter
BS	Beam splitter
CC	Cross-correlation curve
CCD	Charge coupled device
CFP	Cyan fluorescent protein
CIC	Clock induced charges
CMOS	complementary metal oxide semiconductor
Cy5	Cyanine 5, a fluorescent dye
DIC	Differential interference contrast

DiD	1,1'-dioctadecyl-3,3,3',3'-tetramethylindodi-carbocyanine perchlorate, a fluorescent dye	HSPG	Heparan sulphate proteoglycan
dnDYN	dominant negative dynamin	ICS	Image correlation spectroscopy
DOE	diffractive optical element	LP	Long pass dichroic filter
DOPC	Dioleoylphosphatidylcholine	MDF	Molecule detection function
DPP	Decapentaplegic	mRFP	Monomeric red fluorescent protein
EC	Extracellular domain of zFR1	mRNA	messenger RNA
ECM	Extracellular matrix	NA	Numerical aperture
ECS	Extracellular space	PDMS	Polydimethylsiloxane
eGFP	enhanced green fluorescent protein	PMT	Photomultiplier tube
EM-gain	Electron-multiplying gain	QE	Quantum efficiency
EMCCD	Electron multiplying CCD	Rh6G	Rhodamine 6G, a fluorescent dye
FCCS	Fluorescence cross-correlation spectroscopy	RICS	Raster image correlation spectroscopy
FCS	Fluorescence correlation spectroscopy	RNA	Ribonucleic acid
Fgf8	Fibroblast growth factor 8	s.d.	standard deviation
Fgf8-eGFP	Fusion protein of eGFP and Fgf8	s.e.m.	standard error of the mean
FK	Fast kinetic mode for FCS	secEGFP	secreted form of eGFP
FRAP	Fluorescence recovery after photobleaching	SS	Zebrafish Fgf8 signal peptide
GPI	Glycosyl phosphatidylinositol	TIRF	Total internal reflection fluorescence
GUI	Graphical user interface	TL	Tube lens
HeNe	Helium neon laser	TM	transmembrane domain of zFR1
HepI	Heparinase I	wt	wild type
HS	Heparan sulphate	zFR1	Zebrafish Fgf receptor 1

Acknowledgements

The work described in this thesis was carried out in the research group of Prof. Dr. Petra Schwille at the institute of biophysics of the Dresden University of Technology (TUD). Many people contributed to the work, and I want to especially thank:

Prof. Dr. Petra Schwille for the great opportunity to work in her group. Petra, thank you for initiating my projects, for guiding me through the tasks, and for all your believe in me and support. Your door was always open to discuss the status quo of the experiments. Thanks a lot for all your ideas and the help.

Shuizi Rachel Yu and Prof. Dr. Michael Brand for our collaboration project on FCS measurements in living zebrafish embryos. Rachel, for me, this work was the most interesting, and as well the most pleasant part of my thesis. Thank you for giving my technological project of EMCCD-based FCS an interesting biological application, and thank you for exactly asking the relevant questions. Your very effective working style and hence mild pressure of time on me made me focus on the right tasks. Michael, thank you for letting me collaborate with your group, for your questions and ideas, and for your effort towards the important publication.

Dr. Jonas Ries for our collaboration project on two-focus EMCCD-based FCS, and for his contributions in the zebrafish embryo project. Jonas, your enormous theoretical knowledge and practical skills in the lab were invaluable. I have never seen somebody like you writing Matlab codes with the speed of talking in his mother language. Above all, your always positive thinking was a constant motivation for me to continue whatever I was doing. You always had a solution at hand.

Dr. Zdeněk Petrášek for his contributions in the zebrafish embryo project. Zdeněk, whenever I had a theoretical or practical question, you listened carefully. Right after the discussion, you always had a thorough solution in mind. And in case the equations filled more than a page, you typically had them written down in perfect Latex-style the next day. Thank you for all your support.

Dr. Ilaria Fortunati for the measurements in microfluidic channels. Ilaria, thank you for bringing an application to my setup which allowed to measure molecular flow as compared to the otherwise always measured diffusion.

All the members of the Schwille and Brand group, especially Wolfgang Staroske, Jakob Schweizer, Jörg Mütze and Dr. Matthias Nowak for many discussions, for finding solutions, for proofreading the thesis, and above all for the familiar atmosphere that made me like to come to the institute every morning. I also acknowledge the help of all other group members, especially from Claudia Schwäger and Karin Crell for kindly providing assistance.

Dr. Axel Wiegand from Andor Technology for his continuous support on questions of further EMCCD development. Axel, you were always accessible and you promptly reacted. Thank you for kindly inviting me to meet the developers at the Andor headquarters in Belfast, where we discussed many important technological details.

Prof. Dr. Thorsten Wohland for kindly agreeing to review this thesis. His groups at the department of chemistry at the National University of Singapore focusses on very similar research projects, in particular also on EMCCD-based FCS. When we met at conferences, we always had stimulating and fruitful discussions. During the last years, the two groups of Prof. Wohland and Prof. Schwille published several technical advances of FCS basically in parallel. Besides EMCCD-based FCS, these included for example spectrally resolved FCS and the application of FCS and FCCS to living organisms.

This work was supported by an EFRE grant (4-0123.55-20-0370-03/3) to Prof. Schwille and an HFSP network grant (050503-50) to Prof. Brand and Prof. Schwille.

Erklärung (Declaration)

Hiermit versichere ich, dass ich die vorliegende Arbeit ohne unzulässige Hilfe Dritter und ohne Benutzung anderer als der angegebenen Hilfsmittel angefertigt habe; die aus fremden Quellen direkt oder indirekt übernommenen Gedanken sind als solche kenntlich gemacht. Die Arbeit wurde bisher weder im Inland noch im Ausland in gleicher oder ähnlicher Form einer anderen Prüfungsbehörde vorgelegt.

Diese Arbeit wurde von Oktober 2004 bis Mai 2010 unter der Betreuung von Prof. Dr. Petra Schwille an der Technischen Universität Dresden angefertigt.

Dresden, den 31.05.2010

Declaration

I herewith declare that I have produced this thesis without the prohibited assistance of third parties and without making use of aids other than those specified; notions taken over directly or indirectly from other sources have been identified as such. This thesis has not been previously presented in identical or similar form to any other German or foreign examination board.

The thesis work was conducted between October 2004 and May 2010 under the supervision of Prof. Dr. Petra Schwille at the Dresden University of Technology.